The Next Generation of Wide Field Adaptive Optics

by

Jeffrey A. Stoesz
B.Sc.H., University of Calgary, 2001

A Thesis Submitted in Partial Fulfillment
of the Requirements for the Degree of

DOCTOR OF PHILOSOPHY

in the

DEPARTMENT OF PHYSICS AND ASTRONOMY

UNIVERSITY OF VICTORIA

THE NEXT GENERATION OF WIDE FIELD ADAPTIVE OPTICS

by

Jeffrey A. Stoesz
B.Sc.H., University of Calgary, 2001

Dr. J. -P. Véran

Supervisor (Department of Physics and Astronomy)

Dr. C. J. Pritchet

Co-Supervisor (Department of Physics and Astronomy)

Dr. F. D. A. Hartwick

Departmental Member (Department of Physics and Astronomy)

Dr. A. Brolo

Outside Member (Department of Chemistry)

Dr. D. Crampton

Additional Member (Department of Physics and Astronomy)

Dr. P. Hickson

External Examiner (Department of Physics and Astronomy,
University of British Columbia)

Supervisory Committee:

Dr. J. -P. Véran, Supervisor
Dr. C. J. Pritchet, Co-Supervisor
Dr. F. D. A. Hartwick, Departmental Member
Dr. A. Brolo, Outside Member
Dr. D. Crampton, Additional Member

Abstract

In the last decade, adaptive optics systems have been implemented on all the major ground based telescopes and have proven reliable tools for correcting the image to near the diffraction limit. However, the correction from these systems is limited to a narrow field of view. This dissertation address the challenges of widening the corrected field of single conjugate adaptive optics by properly using statistical information on the optical turbulence profile of the atmosphere above the telescope, and by optimizing the trade-off between image quality and field of view.

Altair is the facility adaptive optics system for the 8-meter Gemini North telescope and marks the historical beginning of wide field adaptive optics. Its performance evaluation in Part One is the first on-sky comparison of sparse field images from an altitude-conjugated and a ground-conjugated deformable mirror. All of the other basic aspects of Altair's performance are characterized for use by the Gemini community to plan observations. We also study and report on techniques for extrapolating the edge of the deformable mirror, a critical step in altitude-conjugated mode.

In Part Two we develop a point spread function model for Ground Layer Adaptive Optics (GLAO) that is based on analytic forms of the phase power spectral density. This model has been used for feasibility studies of GLAO on Gemini, and the Thirty Meter Telescope (TMT), currently the most advanced extremely large telescope project. The TMT will be an adaptive telescope that has science goals for the huge 81 square arcminute field of the Wide Field Optical Spectrograph (WFOS). We will show that WFOS-GLAO provides useful gains and will operate in the very wide GLAO (VWGLAO) regime, which has no additional overhead for seeing improved operation. To identify the VWGLAO regime we use statistical turbulence profile models and examine anisoplanatism in terms of image quality metrics relevant to the science that GLAO will likely assist. The VWGLAO regime is where there are useful gains over the theoretical seeing limit for wide field science that measure data collection efficiency as proportional to the product of image quality and the field of view (solid angle). We also show that for many cases VWGLAO will not be impacted by lag anisoplanatism nor by wavefront sensor noise.

Table of Contents

List of Figures

This page is intentionally left blank.

List of Tables

Acknowledgements

I wish to express my eternal gratitude to the many people I have developed formative relationships with during my time in Victoria, at the Herzberg Institute of Astrophysics (HIA) and the University of Victoria. I especially thank my supervisor and guru, Jean-Pierre Véran, without whom my involvement in the exciting and important projects with the Gemini Observatory and the Thirty Meter Telescope project would not have been possible – not too shabby. Thank you for opening the doors of opportunity, for your knowledge, and for your perseverance. A huge thanks to my close collaborator Laurent Jolissaint, with whom I shared an office, dandelions, and the occasional pint. You taught me the mathematical secrets of the atmosphere and more. I will think of you every time I cross paths with a hypergeometric function. I am also grateful to Glen Herriot for stimulating assignments and always taking time to discuss the answers to my questions, in the office or in a rental car. Thank you David Crampton for support and encouragement of my work with Gemini and the Thirty Meter Telescope (TMT). Thank you Scott Roberts and the rest of the team studying the feasibility of the wide field optical spectrograph (WFOS) for TMT. A special acknowledgment to Brent Ellerbroek at TMT for his ideas and interest in my work. At Gemini I especially wish to thank Francois Rigaut, Joe Jensen, and Simon Chan for giving a star struck student such a great experience in Hilo and on the mountain during the commissioning of Altair. Thank you to the whole HIA Altair team for building such a sophisticated and reliable instrument. I especially acknowledge Danielle Frenette, Malcolm Smith, Jennifer Dunn, Jean-Pierre, and Glen with whom I worked closely on commissioning Altair. A sincere thanks to David Andersen and Kei Szeto for pioneering the GLAO feasibility study for Gemini. There are also many people who contributed to relevant work not contained of here. A warm thanks to Tim Davidge, John Hutchings, and Tracy Beck for enjoyable coauthor experiences on their astronomy papers. Thank

you to David Hartwick at UVic and Falk Herwig now at Los Alamos National Lab for such interesting class work and projects on stellar astrophysics. Thank you JJ Kavelaars at HIA and Dave Balam at UVic for fun and exciting asteroid and nearly-discovered-comet observing projects. I am grateful to my peers for your enthusiasm. Thank you to Carrie Besko for her many suggestions that improved this manuscript. I wholeheartedly acknowledge my close friends and family for your unwavering love and interest in my goings-on these past years. You are my foundation. A spirited acknowledgment also to the National Research Council of Canada (Conseil national de recherches Canada) for providing the financial support for this work.

July, 2006 *Jeff Stoesz*
Victoria, BC

Chapter 1

Introduction

1.1 Prelude

In one sentence, astronomical adaptive optics is a means for real-time compensation for wavefront aberrations to improve the angular coherence of the light before the science detector. This is a modern description of a cure to the problem of atmospheric turbulence, most famously noted by Sir Isaac Newton in the following passage in *Opticks*, first published in 1704:

> "If the Theory of making Telescopes could at length be fully brought into Practice, yet there would be certain Bounds beyond which Telescopes could not perform. For the Air through which we look upon the Stars, is in a perpetual Tremor..." [New52]

Another astronomer and instrument builder, Horace W. Babcock is credited with being the first to suggest the adaptive optics cure for atmospheric turbulence in a paper titled "The Possibility of Compensating Astronomical Seeing" [Bab53]. The proposed idea used a rotating knife edge test to provide the signal that would drive a corrector that employed technology reminiscent of the burgeoning television industry of the day. The basic function of each component of his idea is the same as modern adaptive optics systems (cf. §1.4) commonly abbreviated AO, but this innovation was not picked up for two reasons. At that time there was an abundance of astronomy that could be accomplished with seeing limited images, and there was still considerable cost for astronomers to implement the components and creating analogue real-time control. With the development of the laser in the late 60s and its propagation through large distances in the air, the need for AO was revisited, this time with a more substantial military budget. A great deal of pioneering work was done in the 70s and 80s to correct the effects of turbulence for laser propagation and for high resolution images of artificial satellites, but only at the labs and telescopes affiliated with the U.S. Department of Defense. Astronomers did not revisit the AO concept until this defense work was gradually declassified in the late 80s [Col92]. Laser propagation and satellite imagery need only one line of sight to be corrected. Astronomers, on the other hand, want to correct an entire field of view and innovation to accomplish this was started early [Bec88]. The rest is history in the making.

We are now in a decade when more than half of all new large ground based telescope projects include an AO system, and half of those will have a wide field AO system. Table 1.1 shows a sample of present and near future large ground based telescopes together with the largest field of view that they will both correct and detect (column 4). Four of the entries on this table have corrected and detected fields > 4 arcminutes thanks to a wide field AO concept still under development called ground layer AO (GLAO). The aim of this dissertation is first and foremost to assess the feasibility and develop the GLAO concept.

In order to understand the origins of the GLAO concept, let us first describe wide field AO (WFAO). In the context of ground based astronomy, wavefront aberrations are caused primarily by the volume of turbulent atmosphere above the telescope. There are many objects being imaged on the science detector's field of view and therefore many paths through the turbulent volume that need correction, each with similar but non-identical wavefront aberrations. The cause and character of these aberrations will be explained later in this chapter. For now we just need to know that there are only a few rare cases where the wavefront correction can be matched to the path of the science object, and for all other cases there will be unavoidable wavefront errors called *anisoplanatism.* The effect of these errors on the image is incoherence of the light and reduced sharpness, which we will qualify later in

Table 1.1. A sample of wide field adaptive optics on telescopes for the visible and infrared wavelengths. For brevity this list excludes telescopes < 8 meters and in most cases the list of AO systems on each telescope shows only the largest corrected and detected (C&D) field.[b]

Telescope	diameter[a] (meters)	AO system	C&D field[b] (sq. arcminutes)
OWL	$\gtrsim 30$	GLAO	36
LAMA	42	LAMA-AO	1
TMT	30	WFOS-GLAO	81
GMT	7x8.4	GLAO	50
GTC	10.4	HOAO	4
Keck	10	KPOW	< 1
Keck II	10	K2AO	< 1
SALT	$\sim$10	-	-
Hobby-Eberly	9.2	-	-
LBT	2x9.2	LINC-NIRVANA	< 1
Subaru	8.3	IRCS-AO	< 1
Antu	8.2	-	-
Kueyen	8.2	-	-
Melipal	8.2	-	-
Yepun	8.2	GRAAL	64
Gemini N.	8.1	*Altair*	< 1
Gemini S.	8.1	GSAO	4
LSST	8.0	-	-

[a] The effective primary mirror diameters are from http://astro.nineplanets.org/bigeyes.html.

[b] This is the solid angle that will be both corrected by AO and detected by a science instrument. The numbers for future instruments are preliminary.

this chapter and quantify throughout this dissertation. When observing faint astronomical sources the performance will increase with the light gathering power of a telescope, proportional to its diameter squared D^2. When that light is imaged coherently one measure of image sharpness will scale with D^2.* The sensitivity performance is the product of these, proportional to D^4, which is a huge motivator for the partnership of AO and extremely large ground based telescopes (ELTs). However, for many science programs performance is also proportional to the solid angle subtended by the field of view. All current and planned AO systems correct the turbulent volume with two-dimensional deformable mirrors (DM). We will explain these basic AO components later, but for now understand that the turbulence is not concentrated in one plane, but is distributed in the volume of atmosphere defined primarily by the corrected and detected field of view (solid angle). We call the category of all the various schemes that budget the correction of this volume Wide Field AO (WFAO).

A system in Table 1.1 that was originally designed to economically correct the volume with one DM and one wavefront reference is *Altair* on the Gemini North telescope†. Altair's place in the history of WFAO is very significant as evaluation of its performance in Chapter 2 is the first direct comparison of images from an altitude conjugated and a ground conjugated DM. The multi-conjugate AO (MCAO) concept can help programs achieve the D^4 advantage over a wider contiguous field, but it was realized that correcting more than a 3 - 4 square arcminutes with MCAO and current technology becomes extremely difficult and costly. At this point the details of the astronomical science goals enter the budget for correction of the turbulent volume. For answering some cosmological questions a new concept was proposed, often called multi-object AO (MOAO), to break up the contiguous field into numerous corrected "button" sized sub-fields totaling 1 - 10 square arcminutes distributed on a wider field of regard. Other astronomical science programs that either target

---

*The measure is the intensity of a point source, which is proportional to D^2 in the ideal diffraction limit.

†also known as Fred Gillett

objects too numerous or with unknown coordinates make an non-contiguous wide field unattractive. In Chapter 5 we briefly identify some programs for which we characterize the performance as proportional to the product of sharpness and the solid angle subtended by the field of view. The cases we will consider call for fields that budget for and control anisoplanatism on contiguous fields $\gtrsim 30$ square arcminutes.

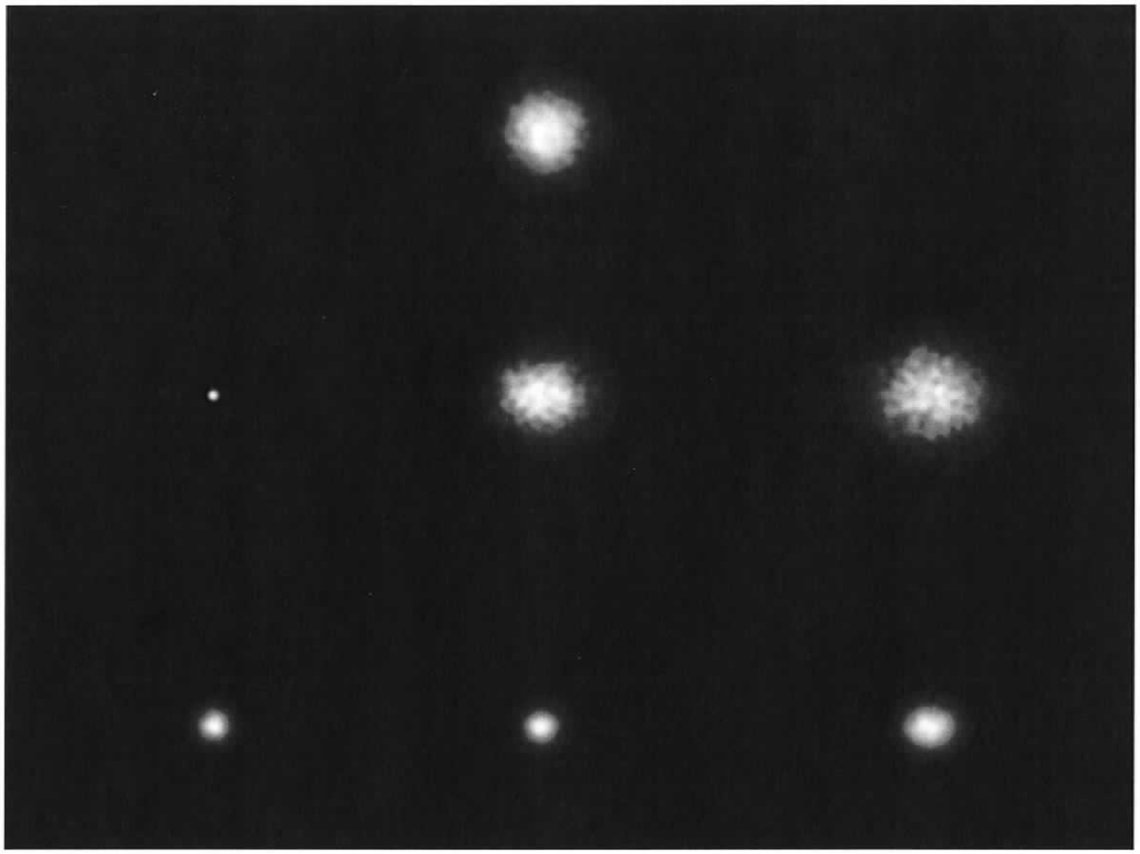

Figure 1.1 An example of how GLAO trades anisoplanatism for field of view. All images are simulated using a spatial domain model of an 8 meter aperture at a wavelength of $1.65\mu m$ with a typical $C_n^2(h)$. The top image is seeing limited. The middle row are simulated images correction from a single on axis wavefront reference, like *Altair*. The bottom row is simulated GLAO with a ring of reference beacons at 3.5 arcminutes radius. The AO images are on-axis (left) 1.5 arcminutes off-axis (mid) and 3.8 arcminutes.

It turns out that when given just one DM to correct this turbulent volume, the best performance gain on any field of view is achieved when that DM is optically conjugated near the ground, leading to the GLAO concept. Fig.1.1 illustrates the images without single conjugate AO (top) with *Altair* (middle) and with GLAO (bottom). GLAO accepts some anisoplanatism degradation to the on-axis image (left) but trades that degradation for improvement at 1.5 arcminutes off-axis (mid) and 3.8 arcminutes off-axis (right). Among the many GLAO developments presented here, the most important is the very wide GLAO (VWGLAO) regime for science cases where performance is proportional to the product of image sharpness and the corrected and detected field. In short our theory states that the field must be pushed as large as the telescope allows, which brings us back to the four telescopes with GLAO systems in Table 1.1. Each of them have unique constraints on the available field for their planned designs and all of them have corrected and detected fields larger than 36 square arcminutes. In Chapter 6 we present a detailed study for the Thirty Meter Telescope (TMT) which has the largest field (81 sq. arcmin) and is considered to be in the VWGLAO regime.

The rest of this introductory chapter will start by explaining the atmosphere's effect on the optical path and the wavefront of light, which is an important basis for the work in all subsequent chapters. We will then define various analysis techniques used on data at the focal plane in §1.3. Then in §1.4 we will briefly illustrate the workings of an AO system with one DM. In §1.5 we outline the challenges for WFAO that we will confront with a solo deformable mirror in the rest of the dissertation.

1.2 Atmospheric turbulence

Turbulence in a fluid is characterized by variations in the velocity of parcels relative to the bulk motion of the flow. If a fluid is viscous enough it will damp out the velocity of parcels. The Reynolds number is a criterion for turbulence that is the ratio of kinetic energy of a parcel over the energy it loses to viscous friction. A laminar flow will develop turbulence when the Reynolds number (Re) exceeds a critical value, which depends on the geometry of the flow. The Reynolds number of a parcel of the flow is given by

$$\mathrm{Re} = LU/\nu \tag{1.1}$$

where L is the characteristic length scale of the parcel, U its characteristic speed, and ν the kinematic viscosity of the fluid. For air, $\nu = 15 \times 10^{-6} m^2/s$, and if the values of L and U are both of the order of $O(1)$ to $O(10)$, then $\mathrm{Re} = 10^4$ to 10^7. This corresponds to fully developed turbulence.

1.2.1 Kolmogorov theory

The foundations of the statistical description for turbulence were laid out by Andrei Kolmogorov [Kol41]. In the Kolmogorov model, atmospheric turbulence is generated by both the large scale shearing flows of atmospheric layers and thermal instabilities caused by ground surface features such as lakes and corn fields. The length scale at which the energy injection occurs is called the outer scale, L_o. As instabilities develop, the turbulent energy cascades down into smaller parcels. The cascade is halted at the inner scale (l_o) where the Reynolds number drops below the critical value and energy can be dissipated by viscous friction. In the range of scales where dissipation and injection are not important the cascade of energy is governed by the rate ϵ.

Observable physical quantities in a turbulence are often only quasi-stationary. Many meteorologic variables such as temperature, pressure, humidity and so on, undergo changes in the mean over time scales ranging from minutes to days to years, which ought to be excluded from the spatial characterization of turbulence. For a statistical description of turbulence, Kolmogorov introduced the structure function D_f for the physical observable $f(\boldsymbol{r})$ as

$$D_f(\boldsymbol{r}, \boldsymbol{\rho}) = \langle [f(\boldsymbol{r}) - f(\boldsymbol{r} + \boldsymbol{\rho})]^2 \rangle \tag{1.2}$$

where the angle brackets indicate an ensemble average and the bold symbols indicate a multi-dimensional vector $\boldsymbol{r} = (x, y, z)$. The structure function of an observable for which the statistics are homogeneous then $D_f = D_f(\boldsymbol{\rho})$. If it is also isotropic then $D_f = D_f(\rho)$, where $\rho = |\boldsymbol{\rho}|$. The structure function is related to the covariance of the observable by

$$D_f(\boldsymbol{\rho}) = 2[B_f(0) - B_f(\boldsymbol{\rho})]. \tag{1.3}$$

Assuming homogeneity the covariance is

$$B_f(\boldsymbol{\rho}) = \langle [f(\boldsymbol{r}) - \langle f \rangle][f(\boldsymbol{r} + \boldsymbol{\rho}) - \langle f \rangle] \rangle. \tag{1.4}$$

Kolmogorov derived a two-thirds power law for the velocity structure function $D_V \propto \rho^{2/3}$ in the domain $l_o \ll \rho \ll L_o$, sometimes called the inertial domain. Obukhov pointed out that any other quantities in the medium that are not changing its basic physical properties can also be described by Kolmogorov's law [Obu49]. The temperature and thereby the refractive index structure function is given by

$$D_n(\rho) = C_n^2 \rho^{2/3}, \quad l_o \ll \rho \ll L_o, \tag{1.5}$$

where C_n^2 is the refractive index structure constant that has units $m^{-2/3}$. The C_n^2 can be measured using thermocouples at various spacings ρ. Fig.1.2 shows three examples of C_n^2 profiles of the atmosphere, derived from data collected by a balloon on a gradual ascent [TBV03, TT06]. We call the layers somewhat below $1km$ the *ground layers* which includes the *boundary layer* of the Earth surface[‡]. At $1km$ and above we believe the turbulence is not strongly affected by the boundary layer and so it is called the *free atmosphere.*

1.2.2 Moments of $C_n^2(z)$

There is a structure to the refractive index structure constant C_n^2 as a function of altitude in the Earth's atmosphere, h. An assortment of modeled $C_n^2(h)$ profiles for the Cerro Pachon observatory site in Chile are shown in Fig.1.2. As we will explore in the upcoming chapters, the basic properties of C_n^2 at a site can be summarized

---

[‡] In the boundary layer, turbulence is injected at many spatial scales, e.g. lakes, cars, a warm telescope dome and so on. The complexity of the boundary layer is not addressed here.

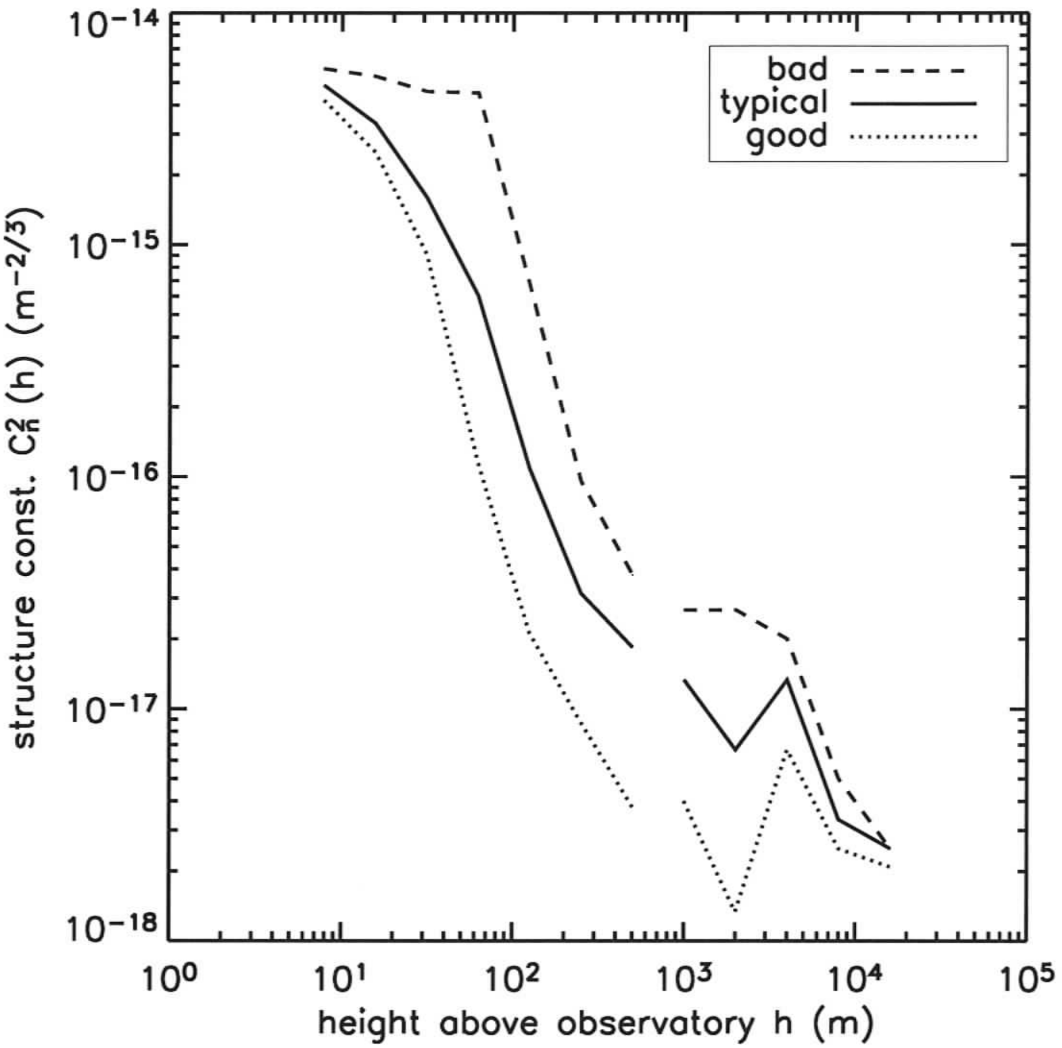

Figure 1.2 An example turbulence strength profile from the ground out to the tropopause. The discontinuity simply marks the transition from the ground layers to the free atmosphere. The nomenclature for each line will be explained in Chapter 5.

using its moments. The m^{th} moment of a profile is defined as

$$\mu_m = \int_0^\infty dz C_n^2(z) z^m. \tag{1.6}$$

We distinguish the direction that the telescope may be pointed $\hat{z}$ from the vertical direction $\hat{h}$, separated by the zenith angle ζ. Any moment can be made a function of zenith angle by noting that $z = h \sec(\zeta)$, where $\sec(\zeta)$ is called the airmass. We will use the vector $\boldsymbol{x} = (x, y)$ to represent the coordinates in the horizontal plane. The following moments are frequently used in adaptive optics:

$$r_o^{-5/3} = 0.4232 \left(\frac{2\pi}{\lambda}\right)^2 \mu_0, \tag{1.7}$$

$$\theta_o^{-5/3} = 2.91 \left(\frac{2\pi}{\lambda}\right)^2 \mu_{5/3}. \tag{1.8}$$

These parameters characterize the spatial and angular coherence properties of the turbulence. The constants for each are defined by D.L. Fried (in [Fri65, Fri82] respectively) to give these moments special meaning for Kolmogorov turbulence, though their usefulness is not limited to purely Kolmogorov turbulence. The spatial coherence length r_o is often referred to as the *Fried parameter* and has the useful interpretation is as the diameter of a beam that has a wavefront phase variance $\sigma_\phi \simeq 1rad^2$. The angular coherence of the profile is characterized by the *isoplanatic angle* θ_o and corresponds to the angle separating two paths (near zenith) where the variance of the phase difference is again $\sigma_\phi \simeq 1rad^2$. One can relate the Fried parameter and the isoplanatic angle with

$$\theta_o = 0.314 \frac{r_o}{\bar{h}}, \tag{1.9}$$

which includes the definition of a weighted mean turbulence height $\bar{h} = (\mu_{5/3}/\mu_0)^{3/5}$.

1.2.3 The Taylor hypothesis

Consideration for the dynamics of the turbulence in Chapter 4 and 5 is greatly simplified by the *Taylor hypothesis* of "frozen flow". The turbulence is modeled as a set of plane parallel layers and the evolution $n(\boldsymbol{x}, z)$ in each layer is dominated by a horizontal displacement caused by wind. For wind velocity $\boldsymbol{v}(z)$ of a layer at height z the displacement is $(\boldsymbol{v}(z) \cdot \Delta t)$. Under the Taylor hypothesis, the required time scale to reconstruct and apply the wavefront correction can be predicted by the horizontal wind speeds.

1.2.4 The near field approximation

Couched in the framework of geometric optics [BW99], the near field approximation allows us to relate the three-dimensional structure function of refractive index $D_n(\rho)$ from §1.2.1 to the two-dimensional phase structure function of the wavefront $D_\phi(\xi)$, where ξ is a baseline in the plane of the wavefront. The phase aberration, $\phi(\boldsymbol{x})$, is $2\pi/\lambda$ times the optical path difference (OPD), where λ is the wavelength of the light. In the plane parallel layer approximation a discrete layer at a height z_n and bounded at $z_n \pm \frac{\Delta z}{2}$ will give an output phase aberration of

$$\phi_n(\boldsymbol{x}) = \frac{2\pi}{\lambda} \int_{z_n-\Delta z/2}^{z_n+\Delta z/2} dz\ n(\boldsymbol{x}, z), \tag{1.10}$$

where $n(\boldsymbol{x}, z)$ is the refractive index minus 1. In the near field approximation the atmospheric phase aberration accumulated over N_L layers is simply

$$\phi(\boldsymbol{x}) = \sum_{n=1}^{N_L} \phi_n(\boldsymbol{x}). \tag{1.11}$$

The near field approximation essentially requires that the aberration from the high altitude layers is small enough that the amplitude of the light wave in the $\boldsymbol{x}$ direction does not appreciably change when propagated to the ground. The highest layer that can produce appreciable amount of aberration is the shearing layer at the tropopause ($12km$ above sea level). Using the definition of r_o and a typical value at the tropopause $r_o(\lambda = 0.5\mu m) = 0.5m$ we find that the OPD is $\sigma_{OPD} = 0.16\mu m$ on scales $x \sim r_o$. This corresponds to a wavefront slope of 0.033 arcseconds. When multiplied by the height of the aberration, the displacement of the amplitude in $x \sim 10^{-3}m$ which is $\ll r_o$ and the approximation is valid over the entire troposphere. Moreover the near field approximation within each layer is valid. Within a layer we can consider the structure function to be homogeneous and isotropic. It can then be shown that substituting Eqn.(1.10) in to Eqn.(1.4) and using Eqn.(1.3) leads to

$$D_\phi(\xi) = \frac{2\pi}{\lambda}\ \Delta z \int_{-\infty}^{\infty} dz'[D_n(\xi, z') - D_n(0, z')]. \tag{1.12}$$

Using Obukov's law (Eqn.(1.5)) and integrating we get

$$D_\phi(\xi) = \frac{2\pi}{\lambda}\ \Delta z\ 2.914381 C_n^2 \xi^{5/3}. \tag{1.13}$$

By using the Fried parameter we can express the more famous form of the phase structure function

$$D_\phi(\xi) = 6.883877 \left(\frac{\xi}{r_o}\right)^{5/3}. \tag{1.14}$$

This derivation was made simple with the help of mathematically well behaved Kolmogorov theory, but Eqn.(1.14) applies only to the inertial domain $l_o \ll \xi \ll L_o$. Nevertheless, assumptions and basic concepts introduced here will be heavily used in the rest of this and other chapters.

1.2.5 Phase power spectral density

The Wiener-Khinchin theorem relates the PSD of a quantity to its covariance. Thus the atmospheric phase covariance in terms of its PSD with units in radians squared of wavefront variance per unit f is

$$B_\phi(\boldsymbol{\xi}) = FT[W_\phi(\boldsymbol{f})], \tag{1.15}$$

where FT is a Fourier transform. The atmospheric phase PSD is two-dimensional with azimuthal symmetric, hence

$$B_\phi(\xi) = 2\pi \int_0^\infty df\ e^{-2\pi f \xi}\ W_\phi(f). \tag{1.16}$$

In Chapter 4 the closed form of the general formulation of the PSD needs to be expressed in terms of the square root of the PSD:

$$[W_\phi]^{1/2} \equiv \widetilde{\phi}(\boldsymbol{f}). \tag{1.17}$$

We use a tilde over the phase symbol ϕ to denote this. As described in §1.2.1 the atmospheric turbulence is a random and statistically stationary processes that can be expressed in terms of the expectation value of the Fourier transform of the phase

$\widetilde{\phi}(\boldsymbol{f})$. In this work we use a modified Kolmogorov power law called a von Karman PSD with outer scale parameter L_o

$$\widetilde{\phi}(\boldsymbol{f}) = \left[0.022896\, r_o^{-5/3} \left(\frac{1}{L_o^2} + \boldsymbol{f}^2\right)^{-11/6}\right]^{1/2}, \tag{1.18}$$

(cf. [Str70]) which tends toward a constant at large baselines ξ (small spatial frequencies f) instead of infinity, as with a pure power law. There are other phase PSD definitions, and certainly the actual phase PSD is more complex than Eqn.(1.18), but current understanding suggests that the von Karman PSD is the most accurate functional form.

1.3 The PSF

Image modeling can take one of two mathematical paths to the image (Fig.1.3). The goal at the bottom right, is the image of a point source, which will be diffracted by the aperture and aberrated by the atmosphere into a point spread function (PSF). The upper branch does the calculation in the *spatial domain* $\boldsymbol{x}$ and requires an iterative model with hundreds or thousands of iterations. Each iteration uses a different realization of the phase to get an instantaneous PSF that is added to the total and simulates a long exposure PSF. The spatial domain model can be made to have a realistic time series of instantaneous wavefronts and PSFs, which is sometimes called a simulation. There are many codes based on the spatial domain model that are widely known to the AO community; a few of them make use of parallel processing to complete the realistic simulations in a useful amount of time. The future of these simulations sees the use of special hardware to allow the simulations to become realistic yet remain tractable. Chapter 3 uses a spatial domain model and will illustrate phase *realization* from an atmospheric phase power spectral density (PSD). It can be shown that the Fraunhofer approximation can be safely used [Goo68] giving the instantaneous PSF

$$I(\boldsymbol{\alpha}) = \left|\mathrm{FT}[\psi(\boldsymbol{u})]\right|^2. \tag{1.19}$$

The $\boldsymbol{u} = \boldsymbol{x}/\lambda$ and ψ is the complex phasor representing the wavefront in the pupil

$$\psi(\boldsymbol{u}) = P(\boldsymbol{u})e^{i\phi(\boldsymbol{u})}. \tag{1.20}$$

The pupil mask $P(\boldsymbol{u})$ is one inside and zero outside the pupil.

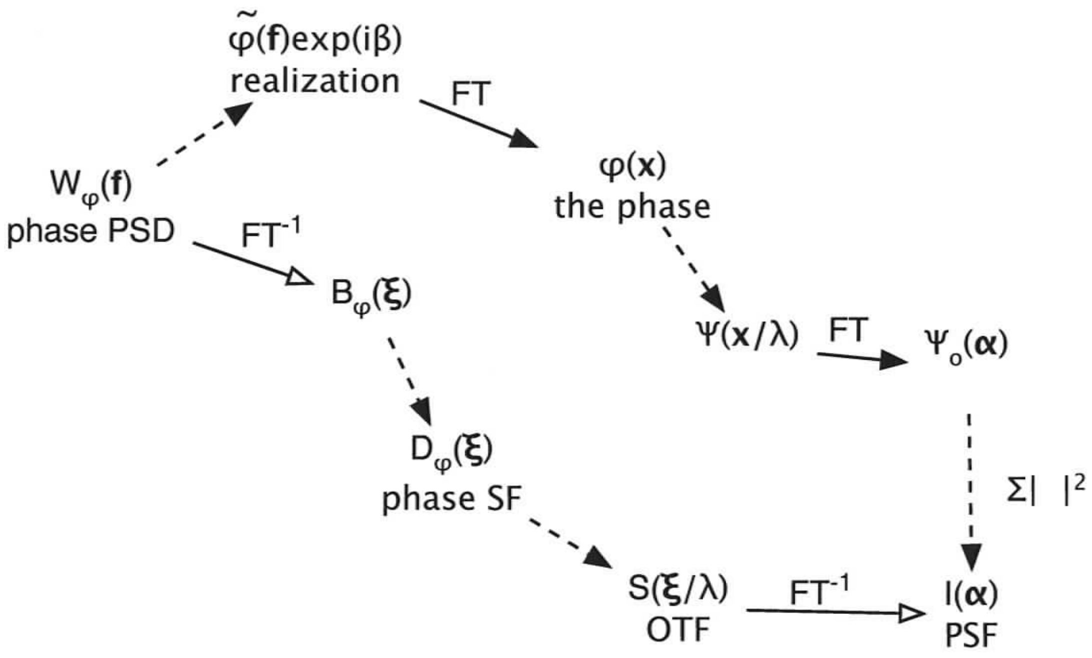

Figure 1.3 A schematic diagram showing the two mathematical paths to the PSF. The solid arrows are integrals solved with Fourier transforms. The dashed arrows are miscellaneous operations.

The lower branch uses more analytic functional forms in the definition of the PSD include all AO effects. This makes it faster because the solution can usually be solved in only one iteration. This branch is called *Fourier domain model* or frequency domain model. Chapter 4 will introduce the PSD we will use to perform trade studies and performance predictions for developing the GLAO concept in Chapter 5 and Chapter 6. The connections from the PSD to the structure function will be given in the form that suits the GLAO PSDs. The connections from the structure function to the optical transfer function (OTF) to the PSF will be needed for the Maréchal approximation to the Strehl ratio, which will be covered in §1.3.2.

1.3.1 Image quality metrics

To quantify the image sharpness we introduce several metrics that are used frequently to reduce the PSF to a figure of merit. The full width at half maximum (FWHM) is a measure of resolution and how it is measured is self explanatory. Strehl ratio is a measure of the contrast in near diffraction limited PSFs. Encircled (or ensquared) energy metrics are commonly used in spectroscopy. We will delve more deeply into the Strehl and encircled energy metrics in the following subsections.

1.3.2 Strehl ratio and the Maréchal approximation

A useful metric for images that are near the diffraction limit of the imaging system is Strehl ratio (SR). We will also introduce the Maréchal approximation, which connects the Strehl ratio to the wavefront variance σ_ϕ^2. Strehl ratio is defined by the integral normalized central intensity of the PSF. This is equivalent to the integral of the optical transfer function (OTF):

$$SR \equiv \frac{1}{\mathsf{S_T}} \iint d\boldsymbol{\eta}\ S(\boldsymbol{\eta}) \tag{1.21}$$

where $\mathsf{S_T} = \iint d\boldsymbol{\eta} S_T$, the integral of the perfect diffraction limited OTF. The auto-correlation theorem gives the long-exposure OTF in terms of the wavefront phasor as

$$\begin{aligned} S(\boldsymbol{\eta}) &= \iint d\boldsymbol{u}\langle\psi(\boldsymbol{u})\psi^*(\boldsymbol{u}+\boldsymbol{\eta})\rangle & (1.22) \\ &= \iint d\boldsymbol{u}\langle e^{i\phi(\boldsymbol{u})-i\phi(\boldsymbol{u}+\boldsymbol{\eta})}\rangle\ P(\boldsymbol{u})P(\boldsymbol{u}+\boldsymbol{\eta}) & (1.23) \end{aligned}$$

where $\eta = \xi/\lambda$. As ϕ is a Gaussian random variable with zero mean, whereby $\langle exp(i\phi)\rangle = exp(-\frac{1}{2}\langle\phi^2\rangle)$, we can use the structure function

$$S(\boldsymbol{\eta}) = e^{-\frac{1}{2}D_\phi(\boldsymbol{\eta}\lambda)} \iint d\boldsymbol{u} P(\boldsymbol{u})P(\boldsymbol{u}+\boldsymbol{\eta}). \tag{1.24}$$

If we assume a circular aperture of diameter D, isotropic turbulence, Eqn.(1.3) and Eqn.(1.4) the Strehl is then

$$SR = e^{-\sigma_\phi^2} \frac{1}{\mathsf{S_T}} \int_0^{D/\lambda} d\boldsymbol{\eta} S_T(\boldsymbol{\eta}) \; e^{\langle \phi(\boldsymbol{\eta}\lambda)\phi(0)\rangle} \tag{1.25}$$

where $\sigma_\phi^2 = \langle \phi^2 \rangle - \langle \phi \rangle^2$. When residual phase aberration $\phi(\boldsymbol{\eta}\lambda)$ is dominated by short correlation distances $\eta \ll D/\lambda$ then $\langle \phi(\boldsymbol{\eta}\lambda)\phi(0)\rangle \simeq 0$ and we get the Márechal approximation to the Strehl

$$SR \simeq e^{-\sigma_\phi^2}. \tag{1.26}$$

We use this approximation for analyzing the performance of the *Altair* AO system in Chapter 2.

The left panel in Fig.1.4 shows example PSFs, each of them azimuthally averaged around the peak of the image, normalized the Strehl value. A semi-log plot is used to show both the bright core and the faint halo. In general, AO smoothes the wavefront allowing more of the light to concentrate in the core of the image measured as an increase in Strehl. The light concentrated in core would have fallen in the region adjacent to the core, from 0.1 to 0.4 arcseconds in this example. Outside of 0.4 arcseconds the AO PSF gradually becomes the seeing PSF. The measured PSF in Fig.1.4 is a star imaged at $2.17\mu m$ with *Altair* correcting the wavefront for the Gemini telescope (8 meters diameter). The modeled curves used the *PAOLA* analytic PSD model by Laurent Jolissaint [JVC06] with parameters that matched the conditions of the measured AO PSF (diamonds). The mismatch of the modeled AO PSF to measurment is due to unaccounted for non-common aberrations ($0.15''$ to $0.3''$) and uncorrectable aberrations (0.6 to 0.7 arcseconds, described in §2.5). The modeled Strehl therefore higher than the measured Strehl.

1.3.3 Enclosed energy function

The right panel of Fig.1.4 show the encircled energy function for the corresponding PSFs on the left. The encircled energy function is the integral of the PSF through

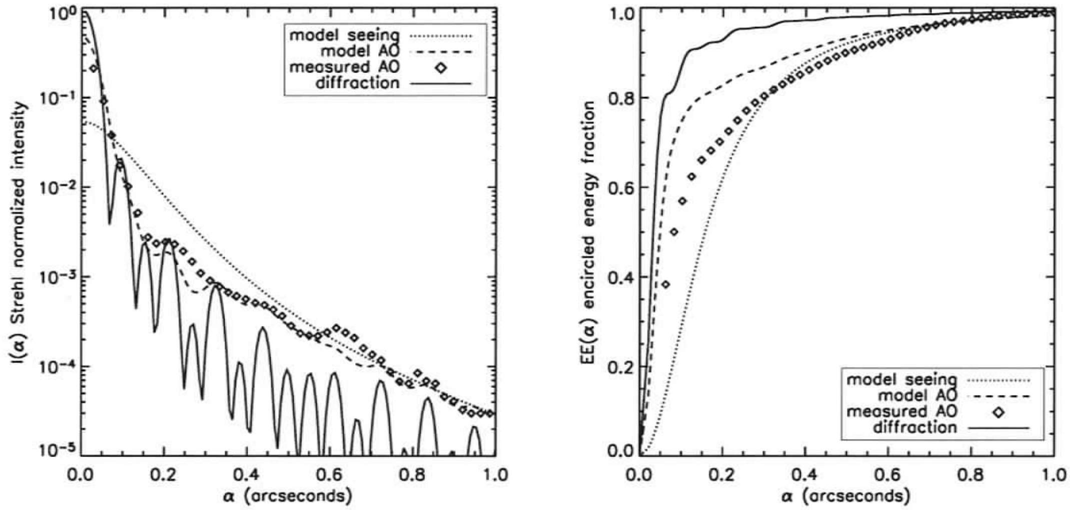

Figure 1.4 Example Gemini PSFs (left) and encircled energy (right) at $2.17\mu m$.

a concentric circular aperture of radius α

$$EE_{circ}(\alpha) = \frac{2\pi}{\mathsf{EE}} \int_0^{\alpha} d\alpha' \; I(\boldsymbol{\alpha}'), \tag{1.27}$$

where $\mathsf{EE} = \iint d\boldsymbol{\alpha} I(\boldsymbol{\alpha})$ is the total energy in the image.[§] In Chapter 5 we use diameter of encircled energy $\omega = 2\alpha$. We also use a square aperture to define the ensquared energy function

$$EE_{sq}(\omega) = \frac{1}{\mathsf{EE}} \int_{-\omega/2}^{\omega/2} \int_{-\omega/2}^{\omega/2} d\boldsymbol{\alpha}' \; I(\boldsymbol{\alpha}'). \tag{1.28}$$

For all apertures the enclosed energy function is monotonic such that the energy fraction is just as commonly specified as the width or radius. For example, the diameter of 50% encircled energy, which is symbolized ω_{50}, or in Chapters 5 and 6 as $EE50$.

1.4 Systems for astronomical adaptive optics

As previously stated, astronomical AO provides real-time correction of the wavefront to improve the angular coherence of the light before it is detected. In this

---

[§] Later in this work we refer to flux of the source rather than the energy of the image when considering a finite exposure time.

section we will briefly describe the principles of the technology used for AO. As we review each component, consider only the left panel of Fig.1.5 which shows a schematic diagram of the *Altair* AO system studied in Chapter 2 and 3. In the right panel of Fig.1.5 is the generally preferred configuration of GLAO. This configuration is studied in detail for the Thirty Meter Telescope in Chapter 6. We restrict the description to the basic components and concepts that are discussed in the remainder of this work; a more extensive exploration of AO systems can be found in [Har98, Rod99].

The **wavefront reference** is a point source separated from the science target by less than the isoplanatic angle $\simeq \theta_o$ if full correction is desired. The brightest stars are generally brightest at visible wavelengths and *Altair*'s WFS uses a CCD to detect that light reflected from the **beamsplitter**.

A **wavefront sensor** (WFS) measures the aberrations in the reference wavefront. This is usually done by dividing the image of the telescope aperture into an array of sub-apertures within which the wavefront gradient is measured, commonly called a Shack-Hartmann sensor. The wavefront is then reconstructed in the control system. The pyramid sensor is another pupil plane interferometric technique that deserves mention [Rag96] but is still under development. It is theorized to have two benefits: 1) it does not sub-divide the telescope aperture; and 2) can average the signal from multiple references on one detector. Both of these benefits lead to a theoretical increase in sensitivity.

The **wavefront corrector** usually a deformable mirror (DM) for applying the required phase compensation to the wavefront, which was reconstructed from the WFS measurements on the previous loop iteration. Continuous face sheet DMs are the preferred corrector for astronomy. The grid of actuators behind the face sheet are registered to the sub-apertures with spacing called pitch, commonly dictated by the coherence length of the turbulence at the wavelength of the desired science data.

Control of an AO system is a vast and complicated subject, beyond the scope of this work. The most important aspect is the control loop with the DM in the optical path of the WFS from which the phase error of the previous iteration is reconstructed. Each iteration the DM effectively accumulates the changes that null the phase of the wavefront in what is called *closed loop* operation.

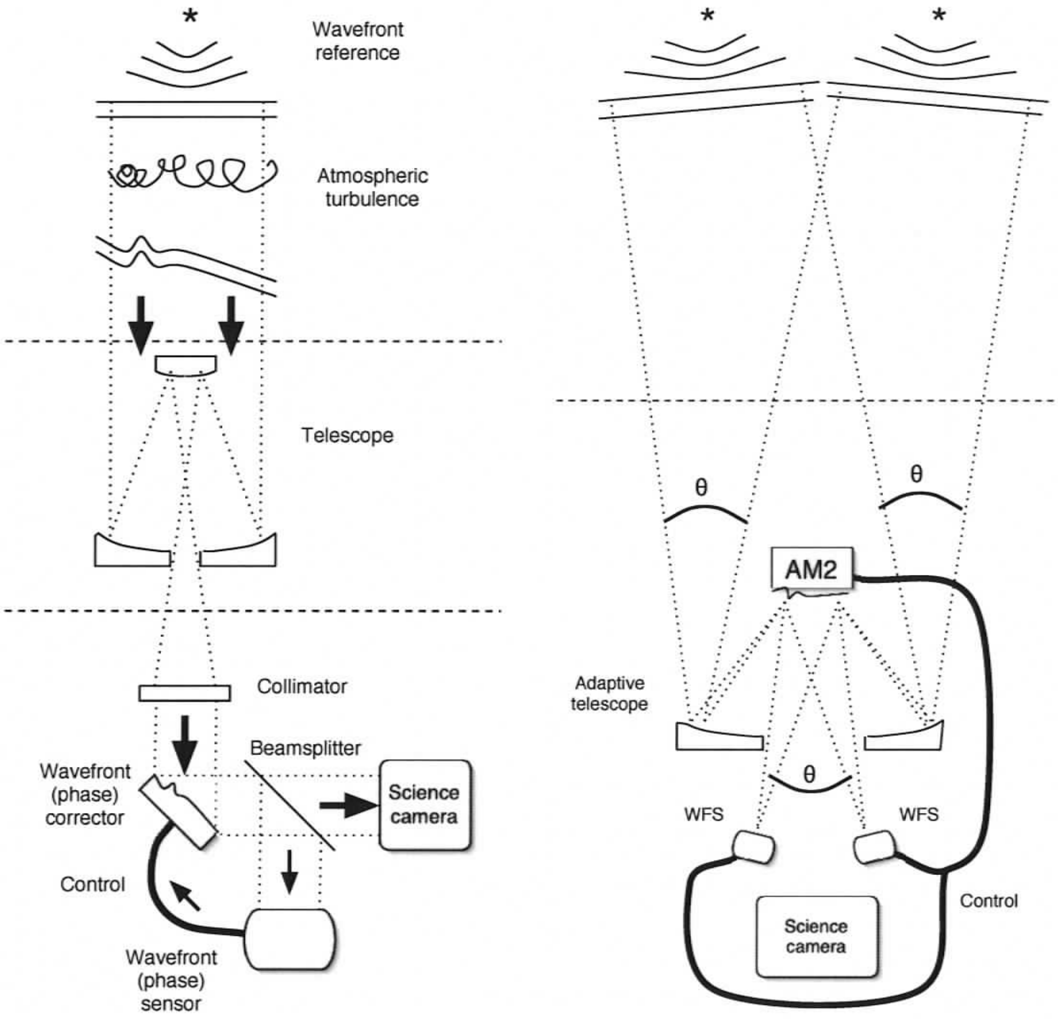

Figure 1.5 Left: the schematic for the *Altair* AO system. Right: the schematic for the preferred GLAO configuration that would use an adaptive secondary mirror (AM2; described in §1.5). The wavefront sensors would be outside of the science field of view.

1.5 Lead-in

This dissertation is presented in two parts. The first part will present work on the first WFAO system, *Altair* for the Gemini North telescope on Mauna Kea in Hawaii. The second part will build a PSF model that we will use to explore the fundamental GLAO parameters and present the main thesis of this work.

Mauna Kea (20°N) is in the mid-latitudes where the jet-stream at the bottom of the tropopause is a major contributor to the total turbulence seen at the telescope. In the design of *Altair* it was correctly recognized that there is a strong layer of turbulence at $8-12km$ above sea level from jet-stream shearing. Measurement of the vertical profile of the turbulence at Mauna Kea was done with a technique called SCintilation Detection and Ranging (SCIDAR) [RE95]. These early measurements were ineffective at detecting the frequency of relatively high amounts of turbulence at low altitudes. Accurate determination of the relative strength of low and high altitude turbulence is difficult and accuracy in this regard is still an area of current research [TVZ05]. Fig.1.2 shows examples of accurate C_n^2 profiles measured at a southern mid-latitude site (Cerro Pachon). This log-log plot of $C_n^2(h)$ at first glance gives diminished importance to the high altitude layers, but remember that the seeing λ/r_o is proportional to $\left(\iint C_n^2(h)dh\right)^{-3/5}$ the thickness of the layers above $2km$ gives the high altitude layers as much impact on the seeing as the ground layers. Thanks to more accurate profile statistics and the small sample of direct measurements of anisoplanatism we will present in Chapter 2, *Altair* has been upgraded with the capability to switch between ground and altitude conjugation. Besides anisoplanatism, Chapter 2 will present all aspects of performance affecting how astronomers plan observations with *Altair*. Efficient acquisition of these data benefited from the preparation of sparse fields of stars queried from catalogues, also presented in Chapter 2.

Work done on the computation and testing of *Altair*'s extrapolation algorithm in Chapter 3 is a system design exercise for altitude conjugation and demonstrates spatial domain modeling on the upper branch of Fig.1.3. The effect of poor extrapolation is similar to anisoplanatism in that the Strehl degrades as a function reference beacon separation.

In Part Two we present two GLAO studies. The first is Chapter 5 where we search for the best corrected field of view and test the strength of angular anisoplanatism compared to lag anisoplanatism. The second in Chapter 6 is a trade study for GLAO assisting the Wide Field Optical Spectrograph (WFOS) on the Thirty Meter Telescope (TMT). Prior to to these studies a simple spatial domain model was used to simulate GLAO and the example PSFs in Fig.1.1, which show the promise of GLAO for only one case. The derivation of an analytic Fourier domain model in Chapter 4 includes angular, displacement, and cone anisoplanatism for an arbitrary arrangement of references. The Fourier domain method is used by many, the most notable exploration of the subject is [JVC06].

Why develop a Fourier domain GLAO model? The spatial domain model that we used to make Fig.1.1 is unacceptably slow and a Fourier domain GLAO model was sought to rapidly explore the GLAO parameter space. Given the natural variability of the ground layer turbulence [TVZ05] means that testing the feasibility of a given GLAO configuration requires evaluating the PSF in many different atmospheric conditions and many places in the field. There are also numerous GLAO configurations that need to be explored in trade studies: DM conjugation, actuator density, beacon range, WFS integration time, and most importantly the arrangement of the science detector fields with respect to the reference beacons. The strategy for using it is to solve one small GLAO optimization or evaluation problem at a time.

Modeling results for GLAO are one of the motivators for extensive site testing campaigns designed to provide $C_n^2(h)$ with the desired accuracy for trade studies. The Chapter 4 model implemented in an early version of the *GLiFFT* code and its results were used for the feasibility study of GLAO at the Gemini observatory [ACS06], motivating a campaign specifically for future GLAO studies. As will be explained in Part Two, the sampling intervals Δh needed for $C_n^2(h)$ shrink proportional to the inverse of the size of the GLAO asterism and as we will see in Chapter 5 the optimal size of the asterism demands layers at $h = [7.5, 15, 30, ...]$. The excitement about GLAO's potential at very wide asterisms have also motivated entirely new techniques for sensing the ground layers of $C_n^2(h)$ (e.g. SHABAR and SODAR).

It is interesting to note that the jet-stream generates turbulence at high altitude for sites at mid-latitudes, away from the poles and equator. The arctic and antarctic may offer large GLAO gains from their lack of high altitude turbulence, at any corrected field of view. These large gains would therefore exclude antarctic GLAO performance from the VWGLAO regime established in Chapter 5. See [TLJ04] for more on GLAO at the antarctic.

The best asterism shape is *a priori* a ring, which for now we will explain with an analogy that provides the correct intuition. Imagine a water cushion that has fixed volume enclosed in a flexible membrane that is allowed to lay flat on the ground. The top surface is flat in a region that is many times larger than the field of view we will map onto it with the sky coordinates $\boldsymbol{\alpha}$. Pressing down on the flat surface with finger tips like reference beacons, the membrane surface dimples in the downward direction that we map to the value of an image quality metric (e.g. FWHM). In this analogy downward in the z direction is an improvement in image quality. As the cushion has a fixed volume the areas a fair distance away from the beacons will rise up above the $z = 0$ plane (cf. middle row Fig.1.1). Adding more beacons (with the same weight) creates a flat region of improved image quality inside their perimeter. The beacons at the edge need the greatest weight to maintain a flat region inside the perimeter; a beacon in the middle can help flatten the surface, but only with a slight amount of weight relative to the edge beacons. Playing with this thought experiment one can see a circular asterism, regardless of the number of stars so long as they are evenly spaced, provides the most uniform correction inside its perimeter and has the greatest area to perimeter ratio.

Leaving the analogy, let us consider the subject of tomography. Using a set of

WFSs, each observing a wavefront from a different line of sight in the field, forming an *asterism*. The three-dimensional turbulent volume through which the field of view propagates can be reconstructed by the geometrical principles of tomography. If you were able to do perfect tomography for the solitary DM of a GLAO system using some asterism, you would then want to drive a ground conjugated DM with the average wavefront integrated from the tomographic volume by an infinite ring of synthetic stars. The problems of noise propagation with imperfect tomography can of course be mitigated by making the actual asterism as close to an infinite ring as possible. In Chapter 5 we show the difference between 8 and 4 beacons on a ring to be minor and hence the effort of tomography dedicated to GLAO to improve upon the performance of 8 and even 4 is of little benefit.

The overdue question is what are the reference beacons? The natural assumption would be stars, which are very good point sources effectively an infinite distance away and when used as a reference beacon are called a natural guide star (NGS).

$$\text{Sky coverage} = \pi\theta_n^2 \;\times\; \text{star density.} \tag{1.29}$$

Where θ_n is the instrument specific isoplanatic radius, which is approximately equal to θ_o with a solo WFS and solo DM with pitch equal to r_o. This is the case for *Altair* and inside the isoplanatic patch under these conditions can provide what is called full correction depicted in Fig.1.4. Towards the galactic poles[¶] the density of bright stars is such that the sky coverage can be as low as a few percent [RG92, ET98]. Spurred by the demands for sky coverage the concept of the laser guide star (LGS) was called for early [Bec88] and is now a rapidly developing technology for AO. The preferred type of LGS system propagates $\sim 15W$ of power per beacon, tuned to $589.6nm$ and focused on a relatively thin layer of sodium atoms at 85 to $100km$ above sea level. We will leave more detail on LGSs for Chapter 6 where we solve several system design problems for GLAO with multiple sodium LGSs. In GLAO, LGSs are convenient but not essential thanks to the potentially wider NGS patrol

---

[¶] In the directions perpendicular to the plane of the Milky Way.

field. The inset on Fig.1.6 shows over 20 useable NGS (black dots of varied size) in the GLAO patrol field. The scatter plot shows mean and standard deviation of FWHM performance modeled with *GLiFFT* for the Gemini GLAO feasibility study. The result for the LGS asterism (large dot; pentagon on the inset) is among the best NGS results (pluses). The standard deviation is for the NGS cases can be up to three times as much, due to uneven weight WFS flux around the annulus. An exhaustive study of LGS vs. a system with all NGS WFS should use optimized re-weighting and requires further development of the Shack-Hartmann WFS noise model presented in Chapter 4 as well as a pyramid WFS noise model. This study has low priority as the feasibility studies undertaken thus far, Gemini GLAO for the Gemini North telescope and WFOS-GLAO for the Thirty Meter Telescope, both benefit from existing sodium LGS infrastructure.

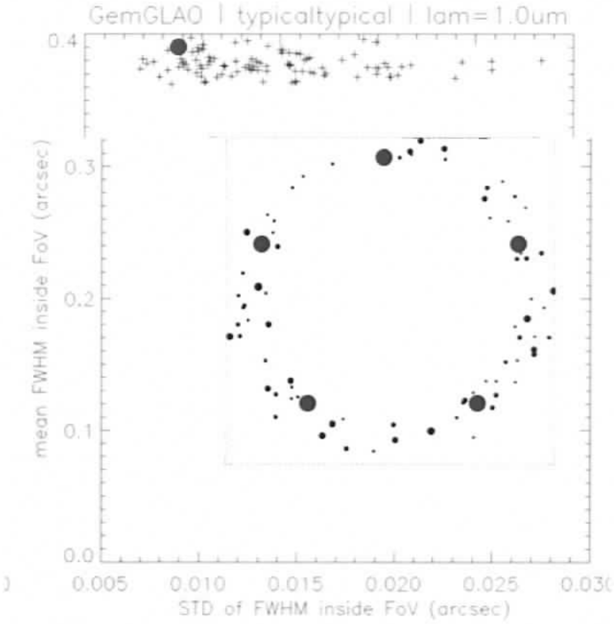

Figure 1.6 The mean and standard deviation of FWHM measured on a GLAO field with radius 5 arcminutes. The large dot is for correction by a pentagon LGS asterism at 6 arcminutes radius (inset, large dots). Each plus is correction by 20 NGS stars at a random pointing near the galactic pole. The 20 brightest NGS where found in an annulus with inner and outer edge at 5 and 7 arcminutes (inset, dots with size proportional to magnitude).

Another key technology that GLAO benefits from is adaptive secondary mirror (AM2) technology [BMK04]. It is part of the natural evolution of AO from a self contained instrument add-on, to an integral part of large ground based telescopes. The right panel in Fig.1.5 shows the schematic of the AO system integrated into the telescope with AM2 then feeding a science instrument or an extended AO system. The secondary mirror of most telescopes is fortuitously conjugated near the ground (-97m for Gemini and +300m for the current TMT design) and therefore the right panel of Fig.1.5 is representative of a GLAO system on an adaptive telescope. The developments in strategies for extended AO systems for ELTs is summarized in [HEA06] and specifically for TMT in [EBD05].

Part One

Altair

"Precision instruments are designed to achieve an *idea*, dimensional precision, whose perfection is impossible. There is no perfectly shaped part of the motorcycle and never will be, but when you come as close as these instruments take you, remarkable things happen ..."

Robert M. Pirsig, *Zen and the art of motorcycle maintenance*

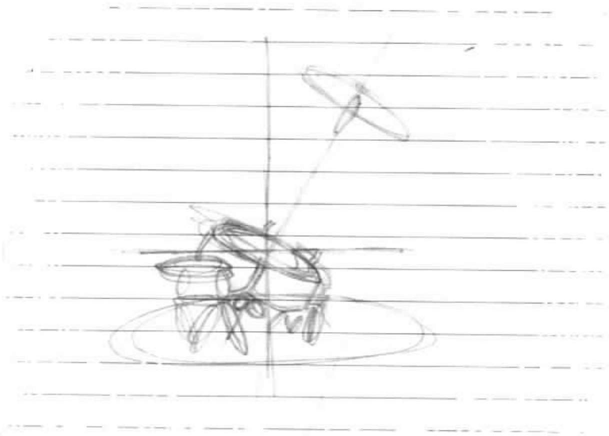

Chapter 2

Evaluation of the on-sky performance of Altair

This chapter is a rewrite of work published in conference proceedings [SVR04] and is reproduced here with the permission of the International Society for Optical Engineering.

Abstract:

In this paper we evaluate the on-sky performance of Altair, the facility adaptive optics (AO) instrument at the Gemini North telescope. The method for doing this on-sky evaluation includes: 1) the choice of suitable sparse stellar fields for point spread function (PSF) observations that must cover a range of guide star magnitudes and angular separations from the guide star 2) an observation strategy and data reduction pipeline and 3) a PSF database from which the performance results are queried. The database stores observatory system parameters and performance observations such as FWHM, Strehl, encircled energy, wavefront sensor flux, as well as coherence length (r_o) and outer scale (L_o) of the turbulence measured in closed loop and therefore synchronous with the focal plane observations of the telescope. Using the database we estimate 20 to 24% Noll efficiency of the system when accounting for instrument vibration and M2 print through aberrations. From anisoplanatism in the focal plane we estimate a distribution of effective turbulence height above the summit to be $3.3 \pm 0.6km$. The performance evaluation method used on Altair is general and the sparse fields used here are well suited to evaluation of any AO system using a single natural guide star with a near infrared imager.

2.1 Introduction

Altair was designed and built at the Herzberg Institute of Astrophysics, Canada, and delivered for commissioning in the Fall of 2002. Deploying Altair is "transparent" for the science instrument, as it reproduces the telescope's f/16 focal ratio, pupil size and position. The present work studies Altair in natural guide star mode with NIRI, the Gemini Near-IR Imager (see [HJI03]) in f/32 imaging mode. Altair uses a 177 actuator deformable mirror (DM) and a separate tip-tilt mirror (TTM) to correct the atmospheric turbulence. The correction is done at a rate of up to 1 kHz (one DM/TTM update every milli-second) and is optimized automatically. It uses a Shack-Hartmann wavefront sensor (WFS) looking at visible wavelength guide star light reflected from a dichroic beam splitter.

One of the unique features of Altair's design is that the DM is optically conjugated at a range of 6.5 km above the telescope. In July of 2005 Altair was fitted with a deployable field lens to effectively re-conjugate the DM close to the ground if desired. The conjugation range of the DM has important consequences on the size of the corrected field of view. Motivated by the conjugation issue we carefully search the USNO and 2MASS catalogues to find sparse fields of stars suited to measuring Strehl and other point spread function (PSF) metrics of the Altair-NIRI-f/32 imaging mode.

AO loop statistics are used in conjunction with PSFs to assess the performance of AO systems, as was done with *PUE'O* on the Canada France Hawaii telescope [RSA98]. Altair has the capability to record statistics of the atmosphere and guide star brightness synchronous to the focal plane data. We have reduced the loop statistics and focal plane data in a homogeneous way and together with other system parameters they are entered into the *PSF database.*

In this work the database is used to characterize Altair performance for Gemini astronomers and to diagnose engineering problems. In §2.2 we describe the selection of sparse fields for PSF observations suitable with a visible wavelength WFS and an infrared imager. §2.3 describes the focal plane and pupil plane data reduction pipelines. In §6.3 and §2.5 we interpret *Altair*'s performances queried from the *PSF database* and summarize the main results in §2.6.

2.2 Sparse Field Selection

A key objective of measuring image quality on the sky is to sample a range of values on several input parameters of the system. Two parameters are controllable: 1) the angular separation of the PSF from the guide star, and 2) the flux received by the WFS from the guide star. The choice of stellar field dictates these two parameters. Crowded fields of stars seriously complicate data reduction and can easily produce systematic errors in Strehl ratio and encircled energy measured from the PSFs. A background object hidden in the halo of the foreground PSF with 1% of the foreground flux will negatively bias the measured Strehl by the same amount. The ideal star fields are therefore sparse, with separations of $2.5''$ to $3''$ and all stars with roughly the same infrared magnitude. One also wants to find a range of guide star magnitudes near the transition from full correction to partial correction and down to the operational limit. It will be shown in §6.3 that the transition starts at $R \sim 11.7$, down to the limit at $R \sim 15.6$ during commissioning.

The 2 Micron All Sky Survey (2MASS) catalogue [CSv03] (all-sky release) was queried first, with the constraints shown in the first row of Table 2.1. The declinations are constrained to those that come within 45° of zenith at Mauna Kea (20°N). H band is the cardinal band pass for acceptance testing and was used to constrain brightness. The saturation limit of the NIRI f/32 camera with a well corrected stellar image in the narrow [FeII] filter* is ~ 7.5 H magnitudes and therefore ~ 10 H magnitudes through the H filter itself. The choice of constraint at the bright end ($H > 9$) will therefore cause saturation or near saturation for a small number of the sparse fields when imaged in the H filter. The faint constraint ($H < 12.5$) keeps the

---

*$\Delta\lambda/\lambda = 0.025\mu m/1.644\mu m = 0.015$

Table 2.1. Constraints on the 2MASS and USNO catalogue, which define the sparse fields. The USNO search has an exception to the star count column, explained in Fig.2.1.

catalogue	position	brightness	field radius	star count
2MASS	$-26^{\circ} < Dec < 64^{\circ}$	$9 < H < 12.5$	$< 13''$	# of H stars ≥ 3
USNO	2MASS field positions	$R < 13$	$< 13''$	# of R stars ≥ 1

relative brightnesses of the PSFs in each group of stars within a factor of 25. The price of this uniformity is that these groups occur very rarely toward the Galactic poles. Lastly, the group must have a radius roughly $< 13''$ in order to fall on the NIRI f/32 camera.

Next, the co-ordinates of the 2MASS selected sparse fields are searched for R band magnitudes in the US Naval Observatory (USNO) catalogue version 1.0B [MLC03]. In order to manage the size of the search in the neighbourhood of the Galactic bulge ($Dec < 5^{\circ}$ and $RA > 17h$ see Fig.2.1) only those 2MASS groups with a number of stars ≥ 4 where queried.

The left panel of Fig.2.1 shows the location of 2MASS groups that have at least one star with $R < 13$. A star with $H \sim 9.5$ will most commonly be $T_{eff} \sim 4500K$ and have an intrinsic colour $(R - H) \simeq 0.2$, not too red. With reddening by the interstellar medium with $A_V \geq 2$ extinction a huge fraction of the Galactic plane groups drop out. Many groups found away from the Galactic plane are in open clusters. The right panel of Fig.2.1 shows histograms of RA for the fields with various guide star brightnesses. The selected fields span RA with most fields from 8 to 17 hours RA being found in open clusters, where the Galactic plane extremely low on in the southern sky.

Table 2.2 shows the sorting priority used for shortlisting the best sparse fields distributed over RA. The best overall fields will have uniform infrared magnitudes and at least one bright visible star for guiding with full correction (< 11.7 V mag of

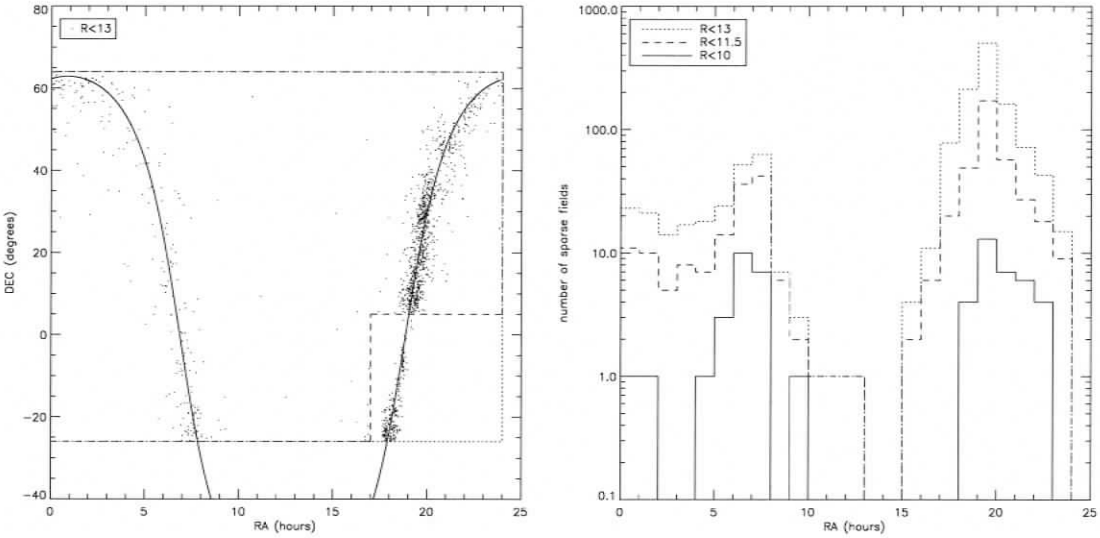

Figure 2.1 The sparse fields plotted on the sky (left panel). The area bounded by the dotted line and not the dashed line was searched for guide stars with 2MASS groups where # of H stars ≥ 4. The area bounded by the dashed line was searched around all 2MASS groups (# of H stars ≥ 3) as described in table 2.1. In the right panel are histograms of RA (right panel) for the fields with a guide star brighter than the R magnitude indicated in the legend.

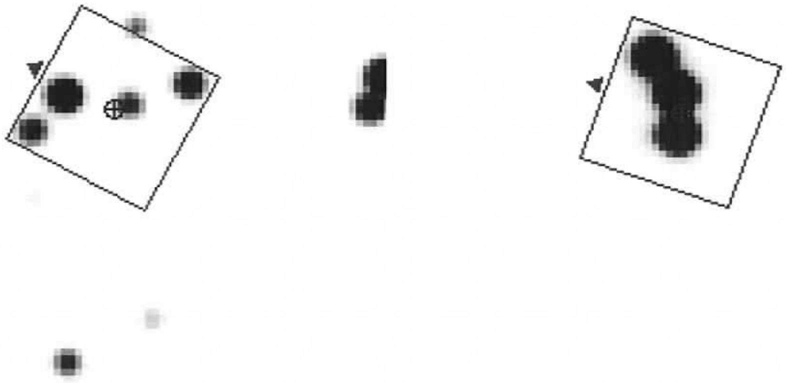

Figure 2.2 The left panel is the field named abr-643 at 07:58:48.7 -20:17:53.7 and the right panel is field baq-179 at 15:09:22.8 +29:30:49.0. The images are 2MASS J band and the box overlay is the 22″x22″ NIRI-f/32 FOV.

Table 2.2. The sorting scheme used to inspect and select the sparse fields in Appendix A.1.

	first sort priority	second sort priority	third sort priority
The best fields (observable December - February)	brightest V mag	number of H band stars	faintest H band star
Fields observable March - November	brightest V mag	number of H band stars	RA

an equivalent K7 star for Altair). Appendix A.1 lists positions and magnitudes of 19 fields selected from these results. Fig.2.2 shows two of the selected sparse fields.

2.3 Construction of the Performance Database

The *PSF Database* includes information derived from the AO corrected images (sometimes called focal plane data) and synchronous AO loop statistics (sometimes called pupil plane or loop data). There are many other measured quantities and telescope parameters such as dome temperature and telescope elevation included as well. In this section we will describe the data and reduction process.

2.3.1 Focal plane data

AO corrected images were recorded with the NIRI camera in f/32 mode. The full image is 1024x1024 pixels and the plate scale was measured at 21.8±0.2 milliarcsec/pixel.[†]

The data preprocessing involved standard near infrared imaging techniques to do flatfield, sky subtraction, and image stacking to give typical integration times of 15-40 seconds. The 15 second integration time is considered long enough to get a good measure of the azimuthally averaged PSF, but if the image of the star was faint with respect to the detector read noise then longer stacks were made for that PSF. The flatfield images where collected using the Gemini Calibration instrument (GCAL) and are sufficient for flatfielding. Accurate sky images were readily available by using the dithered sparse field images.

Subsequent FWHM, Strehl ratio, 50% and 80% Encircled Energy (EE) analysis was done on extracted 256x256 pixel subarrays containing the PSF of interest. The DC sky level on the subarrays was measured from sky count histograms and a circular mask was used to exclude outer regions of the subarray where the radius of encircled energy plot may have negative slope, due to imperfect flatfielding.

2.3.2 AO loop data

Altair loop data such as WFS pixel values, WFS slope measurements, reconstructed wave-front errors and deformable mirror (DM) commands are stored in Altair on circular buffers (CB) containing 60 seconds worth of data at 1 kHz. Alternatively, Altair can calculate and store just the essential statistics on the fly, synchronous with focal plane data. This was the preferred method since statistics can be computed with no overhead and for periods much longer than the length of the CBs.

[†] With the field lens used during the July 2005 run the plate scale was 21.4±.2 milliarcsec/pixel.

The statistics of interest here are the average WFS count rate and the covariance of the DM actuator commands. Altair is calibrated so that these data are always in physical units, e.g. DM actuator commands are in microns of wavefront and the conversion from micron to volts is performed from a look-up table in Altair.

The average WFS count rate, F_{WFS}, was empirically found to be related to the V magnitude and (V-R) color of the guide star by the equation:

$$F_{WFS} = (4.2 \cdot 10^6) \cdot (10^{-0.4(\mathrm{V}-0.73(\mathrm{V}-\mathrm{R}))})(ADU/ms). \tag{2.1}$$

Well calibrated AO systems on the current generation of 8-10 meter telescopes can be sensitive to the size of the turbulence outer scale L_o (see [SLC03] and references therein). A fit based on the von Karman model of the phase power spectral density (PSD) parametrized by the coherence length r_o and outer scale L_o is a judicious choice. The von Karman PSD is modeled in terms of variance of the modal commands sent to the DM (as in [Win91, JVM04]).[‡] An example fit of the von Karman modal PSD to the variance of the DM commands is shown in Fig.2.3. An infinite outer scale PSD is over plotted to show the importance of outer scale to an 8 meter telescope.

2.3.3 Current completion status of the Performance Database

The current Altair Performance Database includes data from the commissioning nights December 2002, 21, 22; April 2003, 16, 17, 19, 21, 22; May 2003, 13, 14, 15, 16; and a science verification night on November 2003, 18. There were sparse field data collected on July 20, 2005, both with and without the field lens re-conjugation of Altair. The December, April, May, November, and July nights are represented in the database by 12, 30, 154, 72, 26 reduced NIRI-f/32 data sets respectively. From these data sets are 380 PSFs that are sensitive to the PSF structure, 3 σ above the sky, out to a full arcsecond in radius or more. This sensitivity was desired for

---

[‡] The Zernike or DM basis functions are often called modes, of a modal basis. See [VRM97] for description of the atmospheric PSD projected onto a Zernike basis, similar to the DM basis functions.

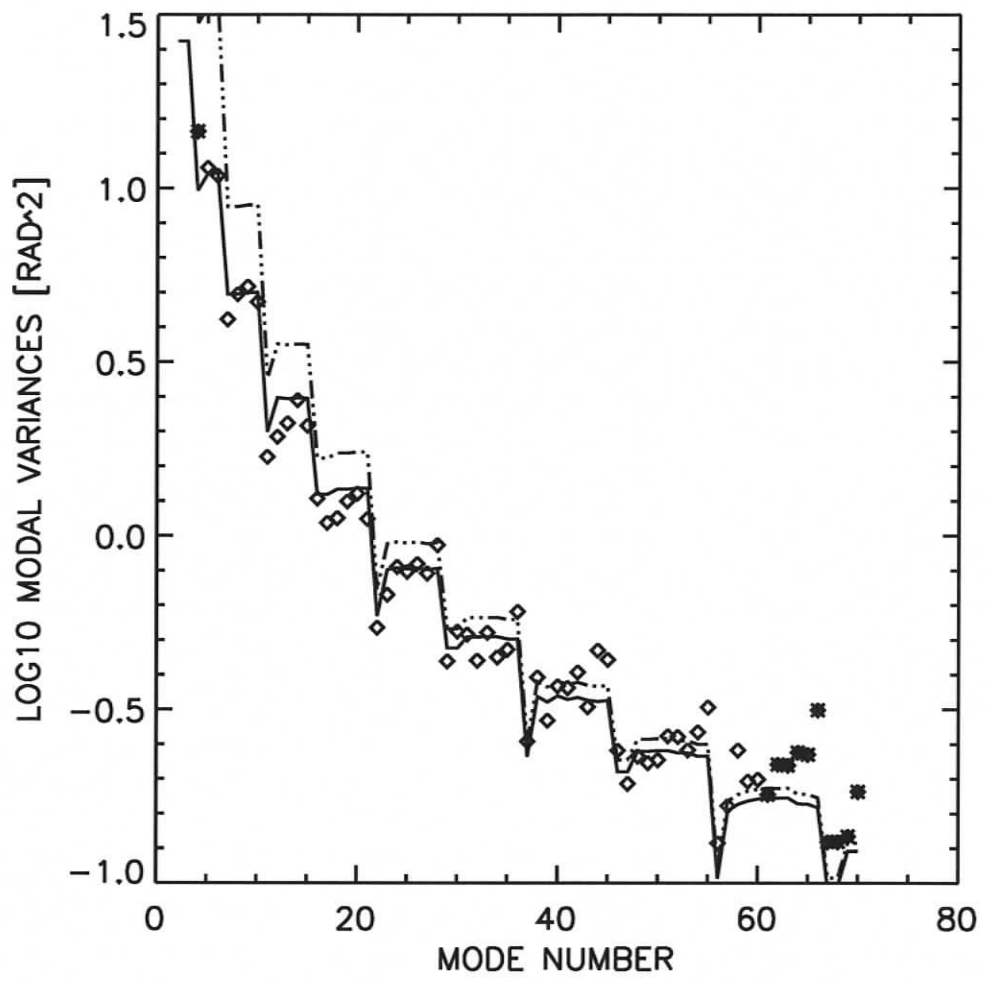

Figure 2.3 An example von Karman modal power spectrum fit (solid line) to the data (open diamonds). The crossed off diamonds are excluded from the fit. The first excluded point is the focus mode, excluded because of active compensation of focus by the telescope secondary mirror. The dash-dot line is the power spectrum with the same r_o but with infinite outer scale. It is over plotted to show the importance of including outer scale on an 8 meter telescope.

accurate encircled energy and Strehl measurements. Images were made in various broad and narrow filters in each of the JHK bands, including [FeII] ($1.64\mu m$) H_2 1-0 S(1) ($2.12\mu m$) and Brγ ($2.17\mu m$). The JHK and K′ bands referred to here are centered at 1.25, 1.65, 2.20, and $2.12\mu m$.

The loop statistics are sporadic, but were collected automatically, hence there are over 2,000 10 second measurements in [December 2002, April 2003, May 2003] and 2,000 in [July, November] 2003. There were over 12,000 measurements in 2004 and 2005, but none were synchronous with our July 20, 2005 focal plane data. Those that were collected synchronously, were in November, much of the May data, and some of the April data, matching a total of 165 focal plane data sets.

2.4 Altair performance queried from the *PSF Database*

2.4.1 Distribution of r_o and lower limits on outer scale, L_o

The left panel of Fig.2.4 is a histogram of r_o values from the von Karman fit (solid) described in the previous section. The results of fitting with and fixed infinite outer scale are also plotted (dotted). We only present those loop data that are matched to focal plane data. Each r_o value has been corrected to zenith using $\cos^{3/5}\xi$ for this plot. Both r_o histograms have lognormal distributions with a mean equal to $0.156 \pm 0.005m$ with width $0.05m$ for von Karman and $0.182 \pm 0.005m$ with width $0.06m$ for the infinite outer scale values.

The distribution of r_o from the von Karman results is also consistent with the findings of [RSA98] at CFHT (mean $r_o = 0.155m$ on a $3.6m$ aperture) where an infinite outer scale fit is acceptable. In a test to verify these AO loop results, several $[r_o, L_o]$ measurements were used to model seeing limited images. The FWHM of over 12 modeled images were compared to open loop images that bracketed each closed loop result and were found to agree very well.

Uncertainty in an L_o measurement on a finite aperture grows rapidly with L_o when it is more than a few times larger than the aperture. We can interpret from

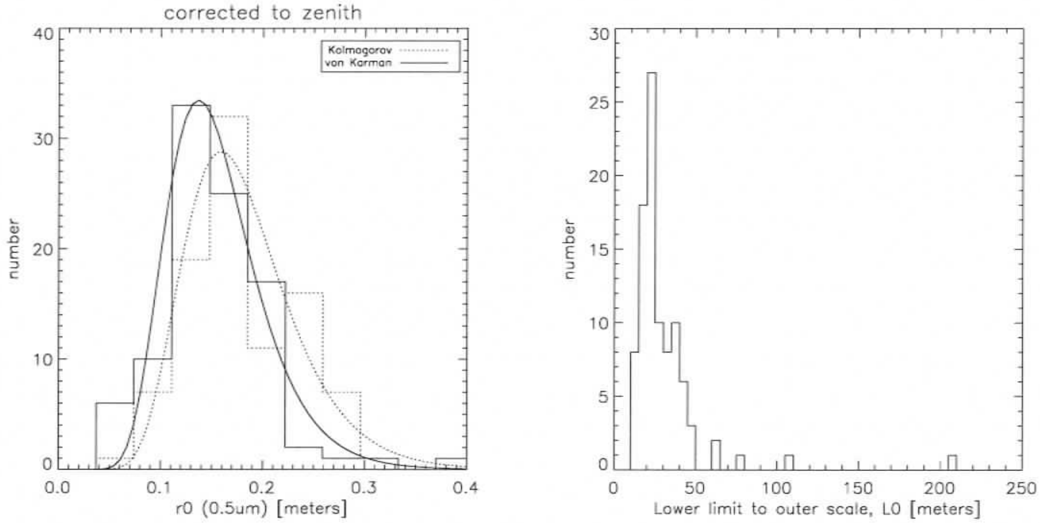

Figure 2.4 In the left panel the distribution of the finite and infinite outer scale r_o values synchronous to the focal plane data presented in this paper. Each r_o value used in this plot was corrected to zenith. A lognormal distribution with a mean equal to $0.156 \pm 0.005m$ and $\sigma = 0.05m$ is over plotted with the histogram from von Karman fits (solid). A distribution from PSD fits with a fixed infinite outer scale is also plotted for comparison (dotted). It has a mean of $0.182 \pm 0.005m$ and $\sigma = 0.06m$. The right panel shows the distribution of L_o values associated with the von Karman fit.

the right panel in Fig.2.4 that 95% of the L_o measurements range between 10 and 40 meters, 4% between 40 and 80 meters and the occasional measurement is fit by an $L_o > 80$ meters.

2.4.2 Altair image quality

The FWHM, radii of 50% and 80% encircled energy, and Strehl performance of the on-axis PSF are plotted against the coherence length of the turbulence r_o. Performance versus guide star separation and magnitude are also given.

FWHM and Strehl vs. coherence length, r_o

Evidence of vibration is seen in the Fig.6.7 where the normalized FWHM measurements asymptote to about 1.2 in K band (asterisks). If we postulate that the asymptote is not at unity because of Gaussian jitter of the image centers then the FWHM of the jitter and the diffraction limited PSF add in quadrature and we can solve for the RMS of the jitter in radians, γ, using

$$\gamma = \frac{1}{2\sqrt{2\ln 2}} \frac{1.02\lambda}{D} \sqrt{\left(\mathrm{FWHM}\frac{D}{1.02\lambda}\right)^2 - 1}. \tag{2.2}$$

The 1.02 correction factor multiplying $\frac{\lambda}{D}$ gives a more precise FWHM for the Gemini diffraction pattern. The K and H band asymptotes ($\mathrm{FWHM}\frac{D}{\lambda} \rightarrow 1.2$ and 1.3) both indicate $\gamma \simeq 15mas$. There is also evidence in Fig.6.7 for excessive scatter and hence variable amounts of vibration between about 10 and $20mas$ in both x and y axes. The FWHM evidence for tip-tilt jitter is corroborated by spectral analysis of tip-tilt errors stored the circular buffers.

Fig.2.6 shows Strehl ratio measurements on images of bright guide stars as a function of r_o. The r_o measurements have one sigma error bars and Strehl error bars are the quadrature sum of one sigma error in sky subtraction and photon noise in the aperture photometry used to calculate Strehl, which are in most cases smaller than the symbols. The solid curve is a Maréchal approximation,

$$\mathrm{Strehl} = \exp\left(-\sigma_\phi^2\right) \quad \text{where } \sigma_\phi^2 = \sigma_{atm}^2 + \sigma_{vib}^2 + \sigma_{tsc}^2 + \sigma_{inst}^2. \tag{2.3}$$

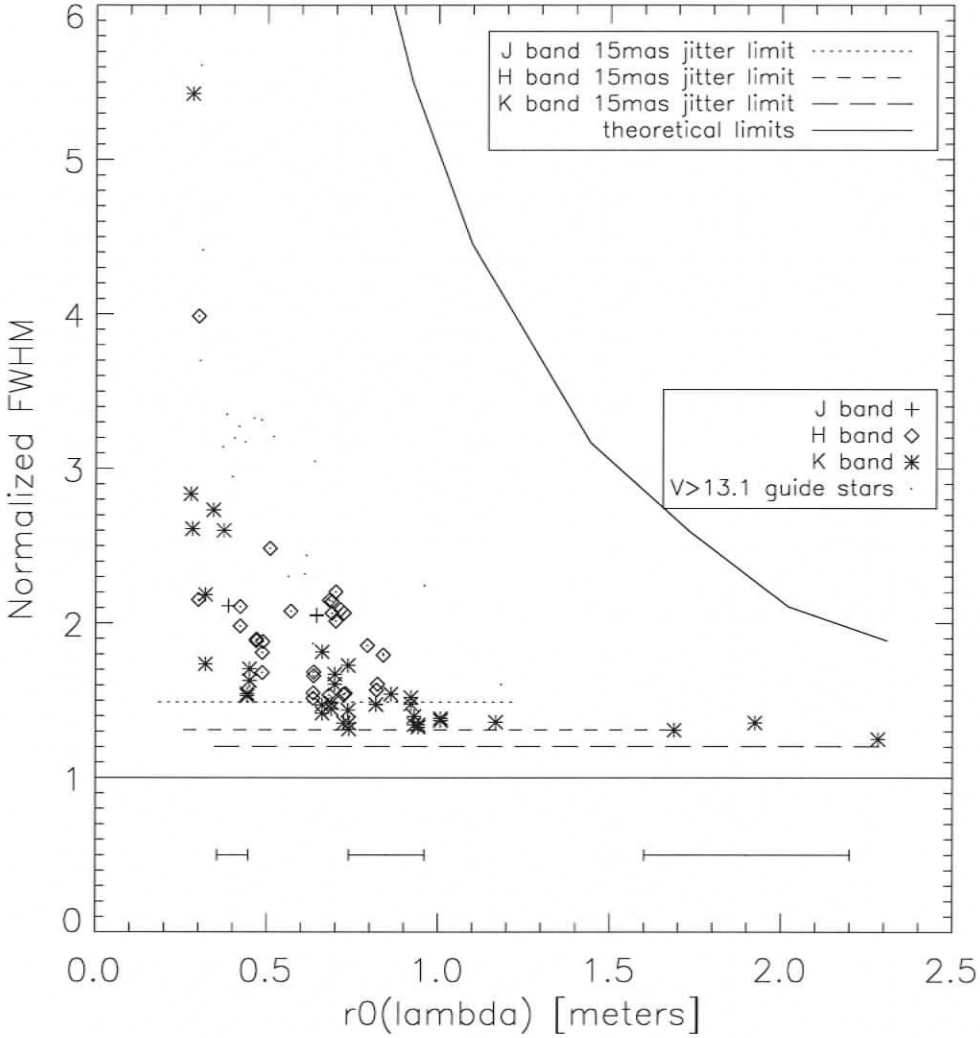

Figure 2.5 . The normalized FWHM, defined as FWHM$\frac{7.906m}{\lambda}$, plotted against r_o. The solid curves are the theoretical limits. Example one sigma error bars on r_o are shown at the bottom and error bars on normalized FWHM are typically smaller than the symbols. Faint guide stars (V> 13.1 equivalent K7 star) are plotted as points.

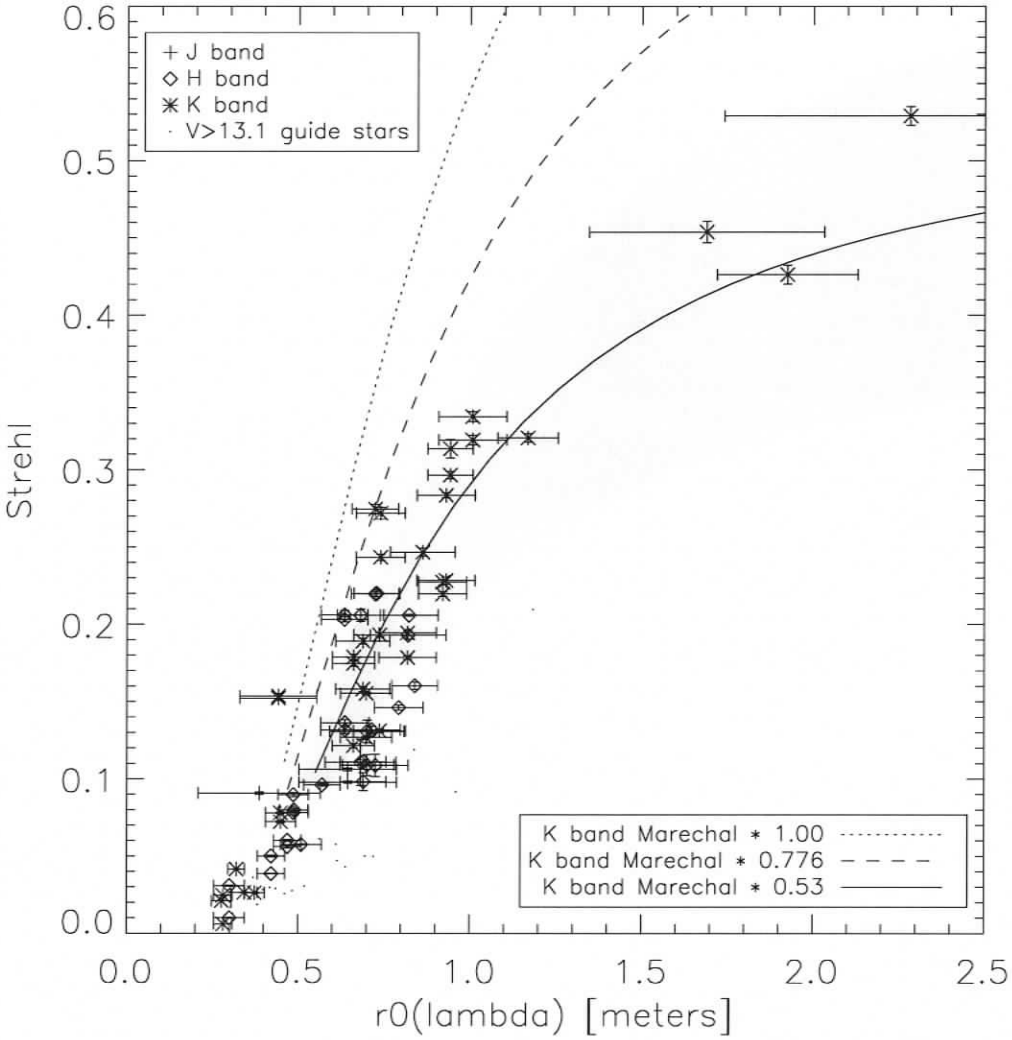

Figure 2.6 . The Strehl of bright guide stars as a function of $r_o(\lambda)$ where λ is the image wavelength. The upper legend indicates λ of each measurement. Some of the faint guide stars (> 13.1 equivalent V) are plotted as points. The solid line is a Maréchal approximation fit to the K band measurements only (asterisks), which indicates atmospheric residual phase variances of $0.019(D/r_o)^{(5/3)}$ (see text). The fit uses $15mas$ as the typical vibration (σ^2_{vib}). The gray zone shows the effect of vibration between 10 and $20mas$. The dashed line is the expected performance if vibrations are eliminated. The dotted line is the theoretical perfect performance if both vibrations and known telescope and instrument aberrations are eliminated.

It was fit to those K band data with Strehl > 0.10, where the approximation is acceptable. The variances $\sigma^2_{vib} + \sigma^2_{tsc} + \sigma^2_{inst}$ take into account three known non-atmospheric sources of Strehl attenuation in the system and $\sigma^2_{atm} \propto (D/r_o)^{5/3}$. The σ^2_{vib} chosen for the fit used $15mas$ RMS as the typical tip-tilt jitter leading to $208nm$ RMS wavefront error (c.f. [Ha99]). This $15mas$ was used with equation 2.2 to plot the typical FWHM asymptotes for JHK bands in Fig.6.7. The σ^2_{tsc} and σ^2_{inst} represent the high order static aberrations (spatial frequencies $\gtrsim 1/2\Delta$) in the telescope and NIRI that Altair cannot correct. We take these values from the error budget of the Altair critical design review [Ha99] with RMS values $\sigma_{tsc} = 116nm$ and $\sigma_{inst} = 124nm$, which combine to $170nm$.

With these three estimated non-atmospheric error sources accounted for, the uncompensated atmospheric phase variance indicated by the fit (solid curve) using a weighting of $1/\sigma$ of the Gaussian r_o error bars is $\sigma^2_{atm} = 0.019(D/r_o)^{(5/3)}rad^2$ which corresponds to a Noll efficiency of 24%.[§] The gray area in Fig.2.6 marks the zone of expected performance with between 10 and $20mas$ of vibration. The dashed line in Fig.2.6 represents expected K band performance if the vibration alone is eliminated. The dotted line is the theoretical perfect performance if all three non-atmospheric effects are eliminated.

The combined telescope and NIRI error budget ($170nm$) is probably pessimistic as one can see in the fit combined with the vibration effect (solid line Fig.2.6) which asymptotes to a Strehl of 0.53. There is one data point, the highest Strehl image, which is significantly above the fitted solid line in Fig.2.6 and suggesting better than typical vibration for that image, but this is contradicted by the corresponding point in Fig.6.7 which suggests slightly worse than typical vibration (long dashed line). If the combined telescope and NIRI error were $126nm$ then the asymptote would be at more comfortable 0.60, leading to a fit with $\sigma^2_{atm} = 0.023(D/r_o)^{(5/3)}rad^2$ and still respectable Noll efficiency of 20%. By inspection of static speckles in the

---

[§] Altair has 12 subapertures spanning the diameter of the pupil's footprint on the conjugated range and hence a theoretical Noll effciency limit of 77% for fitting error and aliasing.

PSF we determined that at least $84nm$ RMS of the budgeted high order telescope aberrations are due to print-through aberrations on M2. See §2.5 for the details of this estimation.

These M2 aberrations are on spatial scales very similar to the subaperture size in the pupil plane that are aliased by the system and introduce aliasing errors at spatial scales equal to and longer than the subaperture size. A calibration technique for antialiasing with a chosen fixed Cassegrain rotator angle was successfully implemented during April 2003. The calibration wavefront was derived from a comparison of long exposure high resolution WFS (18 subapertures across the pupil at the output of Altair) measurements with and without closed loop. This calibration reduces the effect to $\sim 40nm$ RMS at the chosen Cassegrain rotator angle, but the effect can produce errors as large as $\sim 100nm$ RMS at uncalibrated angles.

Radius of Encircled Energy

Fig. 2.7 shows radii of 50% and 80% encircled energy. The curves represent the theoretical seeing limited values (modeled with $L_o = 30m$) in each of the JHK bands. The horizontal lines indicate the theoretical limits of a perfect diffraction pattern. The system provides a gain of about a factor 2 on radius of 50% EE in H and K band.

Guide star brightness and anisoplanatism

The left panel of Fig.2.8 shows Strehl measurements vs guide star V magnitude calculated using Eqn.(2.1) with (V-R)=0.8 (dwarf K7 spectral type). In each band, curves enclose the distribution of Strehl vs. guide star magnitude for some of the 2002 and 2003 entries in the database. From these sketched curves we estimate the start of the transition from full to partial correction to be ~ 11.7 at V band and the operational limit to be ~ 15.6 at V. Table 2.3 shows the transition and limiting magnitudes in terms of dwarf stars of other spectral types.

The right panel of Fig.2.8 shows Strehl loss vs. separation from the guide star

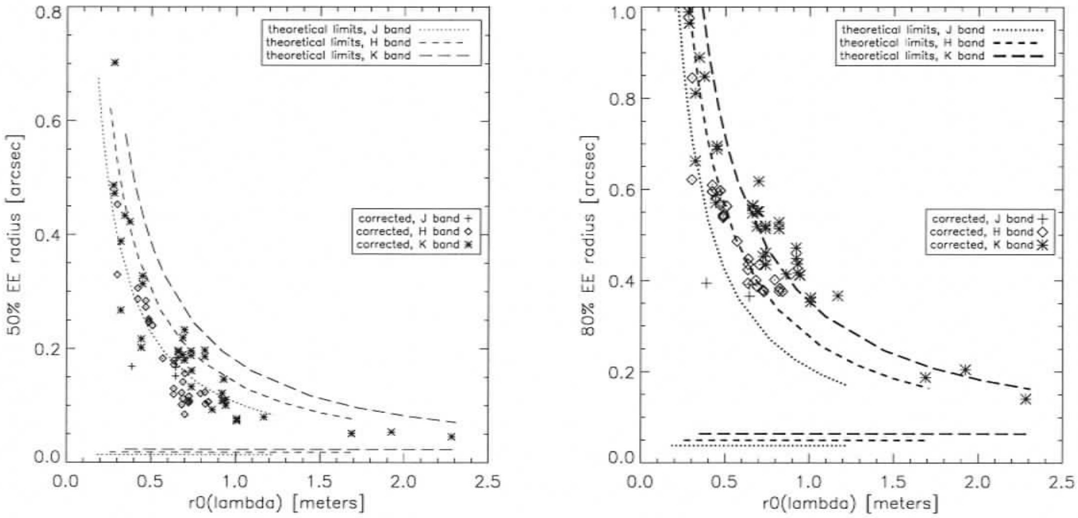

Figure 2.7 In the left and right panels are radii of 50% (left panel) and 80% (right panel) encircled energy. The error bars on EE radius are smaller than the symbols in most cases. Error bars on r_o values are the same as in Fig.6.7 and Fig.2.6. The dotted, dashed, and long-dash curves in both plots represent the seeing limited values (with $L_o = 30m$) in each of the JHK bands.

Table 2.3. V band limiting magnitude and colour for full and partial correction regimes.

Spectral Type		A0	G6	K7	M4		
V-R color	-0.2	0.0	0.4	0.8	1.2	1.6	2.0
Limiting mag for							
full correction	11.0	11.1	11.4	11.7	12.0	12.3	12.6
Partial correction	14.9	15.1	15.3	15.6	15.9	16.2	16.5

queried from the database at zenith distances $0^{\circ} < \xi < 30^{\circ}$ only. The high variability of the turbulence not at the conjugation altitude is apparent in the scatter of the data. The envelope of possible Strehl loss drawn with the solid lines encloses the measurements in JHK when Altair is conjugated to 6.5km. The measurements over plotted with boxes are from July 20, 2005 UT during commissioning of the field lens, which effectively re-conjugates Altair's DM to the ground. All five of the

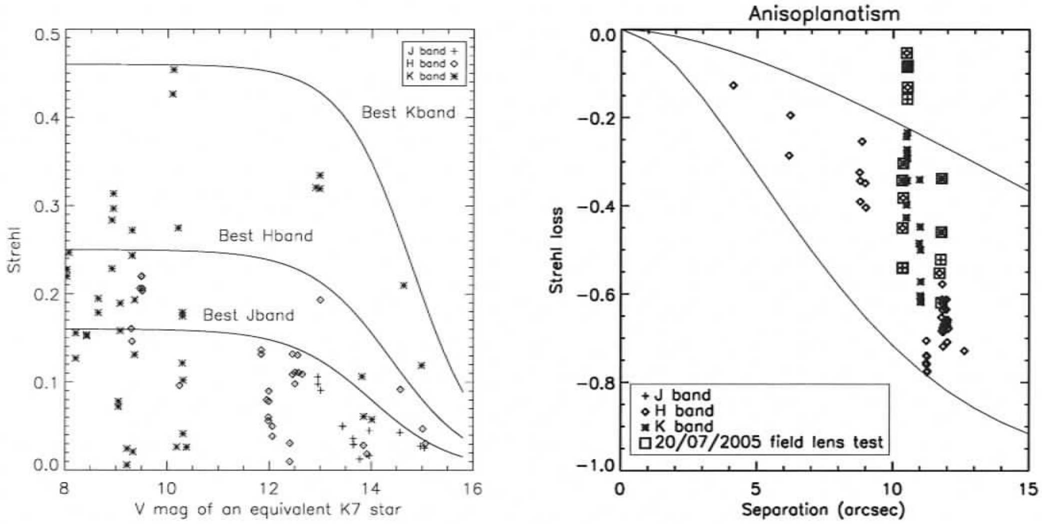

Figure 2.8 The panel on the left shows Strehl vs. the magnitude of a guide star equivalent to a K7 spectral type. The curves are sketched and bound the upper limit of Strehl and faint limit of guide star magnitudes. The panel on the right shows Strehl loss (within 30° of zenith) vs. separation from the guide star.

points that clearly lie above the envelope, improving isoplanicity are with ground conjugation using the field lens.

When altitude conjugated a crescent shaped footprint on the DM is being extrapolated [Ver00] for any PSF that is not the guide star. At $6.5km$ conjugation, a separation of $21''$ corresponds to one actuator pitch. Monte Carlo simulations of Altair's extrapolation algorithm predict -2.5% Strehl loss at $21''$ and just -0.75% at $11''$ in $0.2''$ seeing at $1.65\mu m$, all of which is perfectly conjugated to the DM. Extrapolation error therefore does not account for the off-axis Strehl loss when conjugated at altitude. Peculiar PSF shapes have been seen in images at separation $> 21''$ where the unactuated boundary of the DM is to blame. However the bulk of the Strehl loss at separations $< 21''$ must be atmospheric.

2.5 Wavefront error due to M2 print-through

The left panel of Fig.2.9 shows perfect alignment of the fundamental frequencies of the static speckles in long exposure images at $2.17\mu m$ (asterisks) and $2.12\mu m$

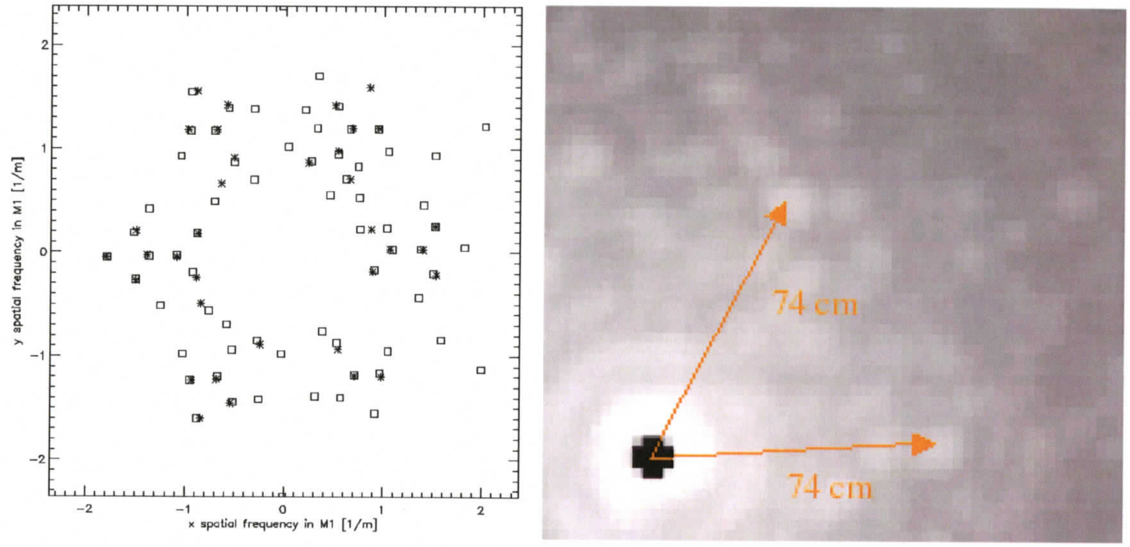

Figure 2.9 The left panel shows the fundamental frequencies in the pupil plane associated with the positions of the static speckles in the focal plane. The asterisks are derived from at 2.17μm image and the boxes from a 2.12μm. The log stretched image on the right shows a high Strehl image at 2.17μm from which the positions and peak counts of the static speckles were measured.

(boxes), which indicate the diffraction is indeed originating from the pupil plane (M2). The right panel of Fig.2.9 is an example of a high Strehl image at 2.17μm. The entire core of the image is very saturated (black) surround by the first Airy ring and a visibly broken third Airy ring.

Beyond the third ring are static speckles from the optics accounting for the telescope and NIRI error budget, but those speckles with six-fold symmetry are attributed to the M2 print-through aberrations. A synthetic PSF made with 24 of the identified print-through speckles gives 0.94 Strehl at 2.17μm and hence 84nm RMS wavefront error.

2.6 Summary

Using sparse fields of stars queried from the USNO and 2MASS catalogues we have collected metrics of the atmosphere and the Altair-NIRI-f/32 PSF. These measurements together with other system parameters are ingested into a *PSF database*. We used the database to characterize performance for Gemini astronomers, illustrating Strehl, FWHM, and 50% EE as a function of guide star brightness and separation, as well as seeing conditions (r_o). We also diagnosed and quantified vibration effects, conjugation effects, and M2 aberrations. The usefulness of the PSF database will continue to increase as more data are accumulated throughout Altair's lifetime.

In addition to the types of engineering work done here the database can also provide serendipity for resolved astrophysical objects, since the sparse star fields used for this work are chosen only for their asterisms. These fields contain stars that have likely not been imaged with such high angular resolution (35 to 100 milliarcseconds).

Chapter 3

Control of the unilluminated actuators in Altair

3.1 Introduction

In this chapter we show results and notes made while testing calculations of wavefront extrapolation matrices for control of "un-illuminated" actuators in Altair, an altitude conjugated AO system. This work uses iterative spatial domain modeling (upper branch, Fig.1.3) to do the calculations, which are described in §3.3. We start this chapter with the theory and practice of generating atmospheric phase realizations given the phase power spectral density (PSD) of the turbulent atmosphere. Making realizations using Fast Fourier Transforms (FFT) of the phase is an old technique (see [Sed98] and references therein) that we develop in §3.2. The methods are defined in §3.4. In §3.5 we test the extapolation matrix method by J.-P. Véran [Ver00] and three variations on the method using simulated observations of Strehl ratio (SR). We find a new method that uses weighted edge actuators is better. The extrapolation matrices are pre-computed only at discrete pupil configurations. We discuss the choice of pupil configurations and look for ways to reduce their number by finding degenerate configurations in §3.4.2.

3.2 Wavefront realization

A realization of the atmospheric wavefront phase is

$$\phi(\boldsymbol{x}) = FT\left[\widetilde{\phi}(\boldsymbol{f})\; e^{i\beta(\boldsymbol{f})}\right] \tag{3.1}$$

where $\widetilde{\phi}$ is the amplitude of the atmospheric phase power spectral density (PSD). Getting a result from a Fourier Transform which is $\Re$eal and has no symmetry requires a hermitian complex normal $e^{i\beta(\boldsymbol{f})}$. A neat way to generate $\beta(\boldsymbol{f})$ is with $\beta'(\boldsymbol{f}) \subset [0, 2\pi)$ that is uniform and random. This is used to define

$$\beta_{even}(\boldsymbol{f}) = \beta'(\boldsymbol{f}) + \beta'(-\boldsymbol{f}) \text{ and} \tag{3.2}$$

$$\beta_{odd}(\boldsymbol{f}) = \beta'(\boldsymbol{f}) - \beta'(-\boldsymbol{f}) \tag{3.3}$$

so that

$$e^{i\beta(\boldsymbol{f})} = cos(\beta_{even}) + i\ sin(\beta_{odd}). \tag{3.4}$$

This has a uniform distribution in a unit circle in the complex plane and is hermitian in $\boldsymbol{f}$.

3.2.1 Wavefront-on-demand vs. screens

One can generate random wavefront array with the needed size on demand. We prefer to generate one or more oversized wavefronts, called *phase screens* from which the needed wavefront can be plucked from a random location $\boldsymbol{x}$, which has less computation time per iteration and sufficient randomness for each test. We will limit ourselves to using a Fast Fourier Transform (FFT) to compute Eqn.(3.1). The cyclic nature of the FFT means that the tip-tilt, and to a lesser extent defocus and astigmatism are under represented in a wavefront array that is less than about twice the diameter of pupil. Oversized phase screens mitigate this.

3.2.2 Renormalizing phase screens

Phase screens with $L_o \rightarrow \infty$ are self-similar and can be rescaled to redefine its r_o or pixel length d. Note that with von Karman screens rescaling should not be done as seeing is coupled with outer scale L_o, r_o, and pixel length d.

The piston removed phase variance on a realization of the phase on a circular aperture of diameter D is defined as

$$\sigma_1^2 = \left\langle \frac{4}{\pi D^2} \int_0^{2\pi} \int_0^{D/2} |\phi(\boldsymbol{x}) - \phi_o|^2 \rho d\theta d\rho \right\rangle, \tag{3.5}$$

where the piston $\phi_o = \frac{4}{\pi D^2} \int_0^{2\pi} \int_0^{D/2} \phi(\boldsymbol{x}) \rho d\theta d\rho$. From [Nol76] the piston removed Kolmogorov phase variance is given in terms of r_o by

$$\sigma_1^2 = 1.030 \left(\frac{D}{r_o} \right)^{5/3}. \tag{3.6}$$

Measuring the variance of the wavefronts provided by the screen can be done with repeated circular samples as in Eqn.(3.5). The corresponding r_o is given by Eqn.(3.6) and the screen can therefore be rescaled with the factor $(r_o/r_o')^{5/6}$. Defining a new pixel length means multiplying the screen by $(d'/d)^{5/6}$. Where d' and d are the new and old values respectively.

The FFT as it is defined in IDL might lead to confusion about the correct normalisation. In IDL

$$f_{ij} = FFT^{-1}\{F_{ij}\} \text{ and } F_{ij} = FFT\{f_{ij}\} \tag{3.7}$$

then

$$\sum_i^N \sum_j^N \frac{|f_{ij}|^2}{N^2} = \sum_i^N \sum_j^N |F_{ij}|^2. \tag{3.8}$$

3.2.3 Phase screens for Monte Carlo simulations

For the our calculations a pair of 2048x2048 pixel phase screen are realized. The Monte Carlo simulation we will describe in the next section call for 128x128 pixels to hold the wavefront. We use one layer that is conjugate to the virtual deformable mirror (VDM), which, when projected on the pupil plane is $11.9m$ across. The screens are therefore $190m$ across. In order to get an extrapolation matrix that is independent of r_o we are forced to choose $L_o \rightarrow \infty$(discussed later). To make the Altair corrected Strehl similar to the plots in [Ver00] we choose $r_o = 0.2m$ at $0.55\mu m$.

The small covariance measured on the 128x128 random wavefront samples indicate, though not conclusively, that the large screens provide a very large number of decorrellated screens. This is important as we are trying to simulate long exposure times. We used one 2048x2048 screen for computing the extrapolation matrix (§3.4) and the other, generated on a different seed, for testing it (§3.5).

3.3 The simulation

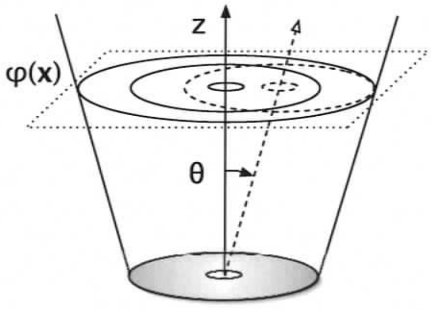

Figure 3.1 The reference star pupil called the analysis pupil is the area bounded by the solid circle and is shown here on-axis. The image pupil (dashed) is off-axis by the separation angle θ.

Altair's deformable mirror (DM) and wavefront sensor (WFS) are altitude conjugated to the plane with phase $\phi(\boldsymbol{x})$ in Fig.3.1. We model an ideal wavefront sensor and reconstructor providing an exact measure of the wavefront inside the analysis pupil. Piston is always removed from the phase unless specified otherwise.

$$\phi = \phi' - \phi_o \tag{3.9}$$

where the piston is given in general by

$$\phi_o = \frac{1}{\mathsf{P}_{\mathsf{gs}}} \iint P_{gs} \phi(\boldsymbol{x}) d\boldsymbol{x}. \tag{3.10}$$

The pupil mask P_{gs} is equal to one inside the pupil and zero outside and

$$\mathsf{P}_{\mathsf{gs}} = \iint P_{gs} d\boldsymbol{x}. \tag{3.11}$$

In Altair the system design calls for the extrapolation to occur on the deformable mirror (DM) actuator commands, hence we model the DM zonally rather than modally. The actuator influence function have a functional form

$$I(\boldsymbol{x}) = (1 + p_4 R) \exp(-p_3 R), \tag{3.12}$$

where

$$R = |x|^{(p_o + p_1|\boldsymbol{x}| + p_2|\boldsymbol{x}|^2)} + |y|^{(p_o + p_1|\boldsymbol{x}| + p_2|\boldsymbol{x}|^2)}. \tag{3.13}$$

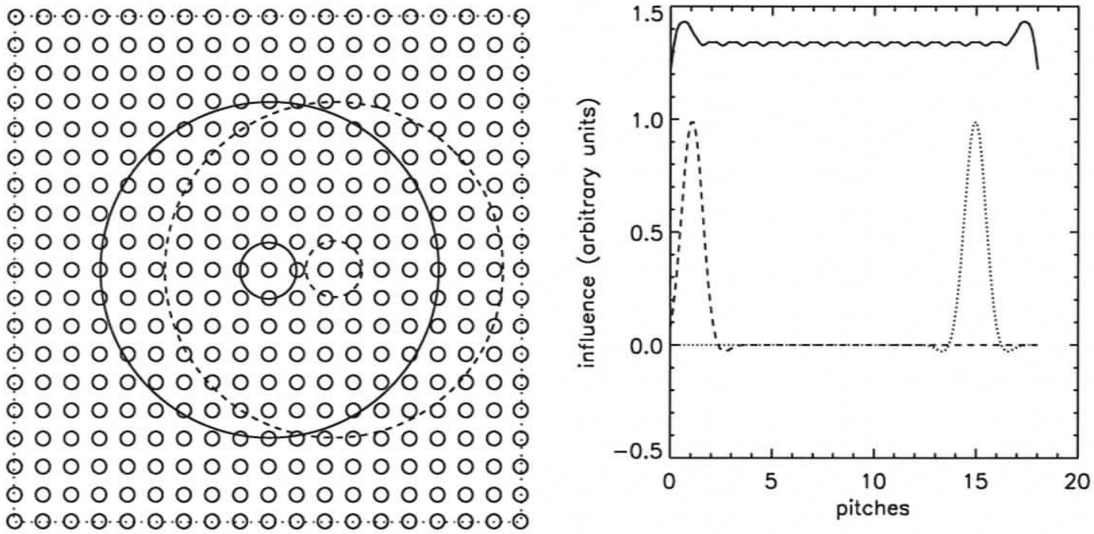

Figure 3.2 Left: the area of virtual DM is bounded by the dotted box, has 19x19 actuators (small circles) 18x18 pitches = 11.9x11.9 meters sampled in the simulations by 128x128 pixels. The area of the virtual DM bounded by the dotted line is symbolized P_{dm}. The circular Gemini pupil area with inner and outer diameters 1 and 7.906 meters is symbolized by P_{gs}. Right: cuts in the x direction through the center of the virtual DM. The dashed line and dotted line are the second and fifteenth actuators in that row set to one. The solid line is a cut along the same row, but is the sum of all 19x19 actuators, each set to one.

The parameters $p_{o...4}$ were fit to the mean of all of the influence functions measured on the DM. The virtual DM shape is modeled as a sum of influence functions. The i^{th} actuator uses the function above, shifted to its location, and symbolized with $I_i(\boldsymbol{x})$. A cross-section of the DM with all actuators pushed to an influence of one is plotted with the solid line in Fig.3.2. The additive model is acceptable here, though more sophisticated techniques for DM modeling in the spatial domain have been recently developed (e.g. [VY06]). Altair is conjugated at a range $z = 6.5km$ and has an actuator pitch of $0.6588m$ implying an angular pitch $\theta = 21.16$ arcseconds.

We will put all of the turbulence into the one infinitely thin layer with output wavefront with phase ϕ. This is done so that computation of the extrapolation matrix and testing is not complicated by anisoplanatism. We define the projection of the phase ϕ on the influence of the i^{th} actuator in the pupil P_{gs} as

$$(\phi|I_i)_{gs} = \frac{1}{\mathsf{P_{gs}}} \iint P_{gs}\phi I_i d\boldsymbol{x}. \tag{3.14}$$

From [Ver00] the setting for an actuator in the analysis pupil (an illuminated actuator) is given by the projection of the wavefront phase, ϕ, on each influence function

$$\boldsymbol{m}_{gs} = \Delta_{gs}^{-1}\big((\phi|I_1), ..., (\phi|I_{N_{gs}})\big)^T. \tag{3.15}$$

Where the matrix of overlap integrals for the actuators is

$$(\Delta_{gs})_{ij} = (I_i|I_j)_{gs}. \tag{3.16}$$

All 361 of the actuators in the virtual DM are in the set $\boldsymbol{m}_{dm}$ and is comprised of the sets $\boldsymbol{m}_{gs}$ and $\boldsymbol{m}_{out}$. A predefined Altair procedure determines which actuators are considered far enough inside the analysis pupil to be considered illuminated ($\boldsymbol{m}_{gs}$) and which are not ($\boldsymbol{m}_{out}$) based on Shack-Hartmann WFS (SH-WFS) subaperture illumination.* Actuators which fall on or just outside of the illuminated patch can be selected to be in $\boldsymbol{m}_{gs}$ when one of their neighbouring subapertures is illuminated. The projection represents measurement by the WFS, reconstruction, and modeled DM shape. We discuss the consequences of differences between projection and SH-WFS measurement in §3.6.

Outside the analysis pupil the actuator settings are extrapolated with

$$\boldsymbol{m}_{out} = E\boldsymbol{m}_{gs} \tag{3.17}$$

Where E is the extrapolation matrix with dimensions $N_{out} \times N_{gs}$. We will discuss the computation of E in the next section.

The phase of the wavefront after it is reflected off of the DM set to $\boldsymbol{m}_{out}$ and $\boldsymbol{m}_{gs}$ is called the corrected or residual phase, given by

$$\phi_r = \phi - \sum_{i}^{N_{gs}} m_{gs_i} I_i(\boldsymbol{x}) - \sum_{n}^{N_{out}} m_{out_n} I_n(\boldsymbol{x}). \tag{3.18}$$

---

*Altair has SH-WFS subapertures with the same pitch as the actuator pitch on the DM. The vertices of the square subapertures are aligned with actuators. The Altair procedure for making this determination is called *altairInitGS*.

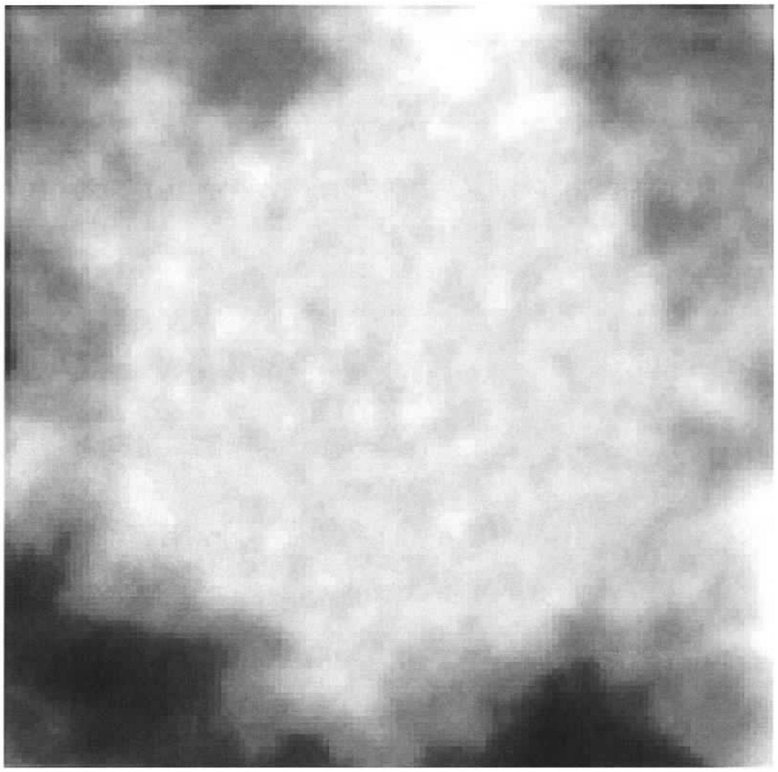

Figure 3.3 Example of a 128x128 residual wavefront phase $\phi_r(\boldsymbol{x})$ realization. The peak to valley of the gray scale is on the order of 1 radian of phase error. The location of the analysis pupil in the picture is clearly visible. The extrapolation is best near the analysis pupil.

The residual phase is characteristically flat inside the analysis pupil with more substantial deviations from flatness outside of the analysis pupil where extrapolation errors occur (Fig. 3.3). The wavefront is centered on the virtual DM in a 128x128 array inside the dotted box in Fig.3.2. There are 7 pixels per pitch and therefore perfect symmetry about the center of the array.

We assess the quality of this residual using the Strehl ratio (SR) of the PSF. An accurate estimate of SR for the parameters we use here requires hundreds of realizations of the wavefront. Recalling §1.3, each realization is corrected by the simulated DM, multiplied by the image pupil (dashed pupil Fig.3.2) Fourier transformed, absolute valued, squared, and then added to the PSF.

3.4 Calculating the extrapolation matrix

For calculation of the extrapolation matrix E we use a Monte Carlo simulation calculation similar to that described above and record the covariance of $\boldsymbol{m}_{out}$ and $\boldsymbol{m}_{gs}$. Both the $\boldsymbol{m}_{out}$ and $\boldsymbol{m}_{gs}$ vectors are calculated from projections of the wavefront as in Eqn.(3.15) for $\boldsymbol{m}_{gs}$ and in a similar way for $\boldsymbol{m}_{out}$. Each set of the measured $\boldsymbol{m}_{out}$ and $\boldsymbol{m}_{gs}$ pairs are added to the covariance matrices

$$\Gamma_1 = \langle \boldsymbol{m}_{out} \boldsymbol{m}_{gs}^T \rangle \quad \text{and} \tag{3.19}$$

$$\Gamma_2 = \langle \boldsymbol{m}_{gs} \boldsymbol{m}_{gs}^T \rangle. \tag{3.20}$$

The extrapolation matrix is then given by the matrix multiplication

$$E = \Gamma_1 \Gamma_2^{-1}, \tag{3.21}$$

which has dimensions $N_{out} \times N_{gs}$. The derivation of this optimal extrapolation matrix is in [Gen95]. The matrix Γ_2 is not well conditioned and hence inversion needs to be done with care.† It is important to note that the r_o dependence in Γ_1 and Γ_2 combine to cancel out in the definition of E. The covariance matrices are the essence of the optimal extrapolation matrix method and we will not be modifying Eqn.(3.21). We will however set up four methods for projecting $\boldsymbol{m}_{gs}$ and $\boldsymbol{m}_{out}$, including the method of [Ver00].

We test two distinctly different methods for doing the covariance matrix computation, each of which has two variations, for a total of four methods. The full calculation described in [Ver00] we call *method 2*. *Method 1* will involve removing information about the analysis pupil during computation of the covariance. The wish is to have a single covariance matrix that can be used to construct the extrapolation matrix for any analysis pupil configuration called *method 1*a. For *method 1*b we add some information about the analysis pupil location to in order to correctly

---

†We zero any singular values in the decomposition that are smaller than 10^{-4} in a ratio with the dominate singular value.

remove piston. For *method 2*b we take actuators in the $\boldsymbol{m}_{gs}$ set that are near the edge of the analysis pupil and include them in the $\boldsymbol{m}_{out}$ set as well. For all methods we check for negative effects due to precomputing covariance matrices only for a finite number of analysis pupil placements.

3.4.1 Edge actuators and *method 2*

The vector $\boldsymbol{m}_{gs}$ is calculated from a projection of the phase on to the actuator influence functions. Recall that the projection of the phase ϕ on the i^{th} actuator in the analysis pupil P_{gs} is given by

$$m_{gs_i} = (\phi|I_i)_{gs} = \frac{1}{\mathsf{P_{gs}}} \iint P_{gs} \phi I_i d\boldsymbol{x}. \tag{3.22}$$

Similarly we are have projection on each m_{out_n} with the complement to the analysis pupil mask, $P_{out} = 1 - P_{gs}$. The location of the analysis pupil of course changes the number of actuators inside. Furthermore, those actuators near the cusp will have projections (Eqn.(3.22)) that will be strongly affected if the pupil is displaced by just a fraction of a pitch.

Methods 2a & 2b

For *method 2*a, membership of actuators to $\boldsymbol{m}_{gs}$ and $\boldsymbol{m}_{out}$ is set with the predefined procedure *altairInitGS*, which places edge actuators in the analysis pupil P_{gs}. The only difference with *method 2*b is that those edge actuators in $\boldsymbol{m}_{gs}$ are also represented in $\boldsymbol{m}_{out}$. This means there are additional rows and columns in the linear system Eqn.(3.17) for *methed 2*b. The chosen criterion for an *edge actuator* is

$$\frac{(\phi|I_i)_{gs}}{(\phi|I_i)_{dm}} < 0.3, \tag{3.23}$$

where P_{dm} mask is the large box drawn with a dotted line in Fig.3.2 (1 inside and 0 outside). With this criterion there are between 12 and 16 of these edge actuators, depending on the location of the analysis pupil.

3.4.2 Analysis pupil configurations and *method 1*

The location, size and shape of the analysis pupil P_{gs} are collectively called pupil configurations. Here we choose how many discrete configurations for which we need to pre-compute E, and afterwards we define *method 1*. The numbering scheme for the virtual DM actuators (bounded by the large dotted box in Fig.3.2) starts in the bottom left, counting along rows as follows:

```
...
38  39  ...
19  20  21  ...
0   1   2   3   ...
```

The *Altair* system design [V01] calls for 16 analysis pupil locations in a 4x4 grid located above and to the right of the base central actuator. The base central actuator is numbered 180. The numbering scheme for the 4x4 locations starts at actuator 180 with points separated by $\frac{1}{4}$ of a pitch. The locations are shown in parentheses with respect to actuators [180,181,199,200] in the following diagram.

```
199                     200
(12)   (13) (14) (15)
(8)    (9)  (10) (11)
(4)    (5)  (6)  (7)
(0)180(1)   (2)  (3)    181
```

For this definition on the 16 base analysis pupil locations, 3 sets of covariance matrices calculations (Γ_1, Γ_2) can be avoided because rotation of the virtual DM makes the configurations centered on locations [(1),(2),(3)] degenerate with [(4),(8),(12)]. See appendix B.1 for further discussion.

In addition to the natural guide star (NGS) case with the analysis pupil pictured in Fig.3.1 and Fig.3.2, there is a laser guide star (LGS) case as well. The LGS pupil footprint on the DM is given by the distance from the beacon to the DM conjugation times the angle that it subtends to fill the pupil of the telescope. The Gemini pupil diameter is 7.906 meters and the range to the sodium layer when pointed at zenith is $\sim 90km$ which gives a footprint diameter of 7.34 meters, a little more than 11 pitches. For the NGS and LGS (zenith) cases we have 32 configurations and 26 unique covariance calculations per method.

Methods 1a & 1b

In an attempt to reduce the dependance of covariance computation on the analysis pupil configuration we define *method 1* to use P_{dm} (dotted box Fig.3.2) rather than P_{gs} in Eqn.(3.15). As a result there is only one matrix of overlap integrals Δ_{dm} (Eqn.(3.16)) needed and therefore Γ_1 and Γ_2 can be assembled from the rows and columns of $\Gamma = \langle \boldsymbol{m}_{dm} \boldsymbol{m}_{dm}^T \rangle$ at the time when the analysis pupil configuration is known. For *method 1*a, piston is removed from $P_{dm}\phi'$, making *method 1*a completely independent of analysis pupil configuration. Hence, *method 1*a will need only one covariance matrix Γ. For *method 1*b, piston is removed from $P_{gs}\phi'$ as in *method 2* and needs covariance calculated on the same number of analysis pupil locations as in *method 2*. *Method 1*b has no practical benefits and is included to show the low importance of piston removal in the covariance computation.

3.5 Testing and results

A summary of the methods for covariance computation is shown in Table 3.1 We saved the covariances for each method at 1,000 and 10,000 iterations. To test these methods using Strehl ratio (SR) we found that SR reached an asymptote in 161 iterations of the simulated PSF at each image star offset, also labeled "science star offset" on the x-axis in Fig.3.4. These plots show the extrapolation out to 47 arcseconds or 2.2 pitches, in the positive x direction only (cf. left panel Fig.3.2) The y-axis in Fig.3.4 shows SR for the LGS case (left pair of plots) and NGS case (right pair). The results from the covariance matrices with 10,000 iterations are the top pair of plots and 1,000 iterations are the in the bottom pair.

Comparing with results of the covariance computation with 1,000 iterations (bottom pair of plots) we see that 1,000 is gives just 3% lower Strehl at 47 arcseconds. This suggests that 10,000 iterations in the covariance matrix computation

Table 3.1. Summary definition of six methods for extrapolation. The success of each method to improve off-axis Strehl ratio is also ranked.

Name	piston removed from ϕ'?	product matrix	edge actuators in both $\boldsymbol{m}_{gs}$ and $\boldsymbol{m}_{out}$?	LGS rank	NGS rank
*method 1*a[1]	no	Δ_{dm}	no	4	3
*method 1*b	yes	Δ_{dm}	no	5	4
*method 2*a[2]	yes	Δ_{gs}	no	2	2
*method 2*b	yes	Δ_{gs}	yes	1	1
Methods that do not use pre-computed extrapolation matrices					
nearest neighbour slaving	-	-	-	3	5
no extrapolation	-	-	-	6	6

[1] This method needs only one covariance matrix Γ for any configuration!

[2] This is the original method of Véran [Ver00].

are sufficient.

*Method 1*a (long dash) and *method 1*b (dotted) is worse than nearest neighbour slaving (dash dot-dot-dot) for the LGS case. *Method 1* is unacceptable and shows the importance of proper simulation of edge effects. *Method 2*b (dash dot) is the clear winner because it fully takes into account the vignetting by the analysis pupil. The benefit is apparent both off-axis and especially on-axis for the LGS case where a full ring of actuators are being extrapolated. With the chosen edge actuator criterion (Eqn.(3.23)) *method 2*b requires an additional 12 to 16 rows and columns in Γ_1 as compared to *method 2*a.

In Fig. 3.5 the on axis performance is in the top panels, followed by the 47 *arcsec* separation in the middle, and the number of illuminated actuators (length of the $\boldsymbol{m}_{gs}$ vector) in the bottom panels. In these plots the analysis pupil location is centered on actuator 180 when the abscissa is zero. When the abscissa is 1 the analysis pupil is on actuator 181. The image at 47 *arcsec* (2.2 *pitches*) separation from the analysis pupil was located to the far left of the analysis pupil. The analysis pupil moved though areas corrected by four different sets of covariance matrices

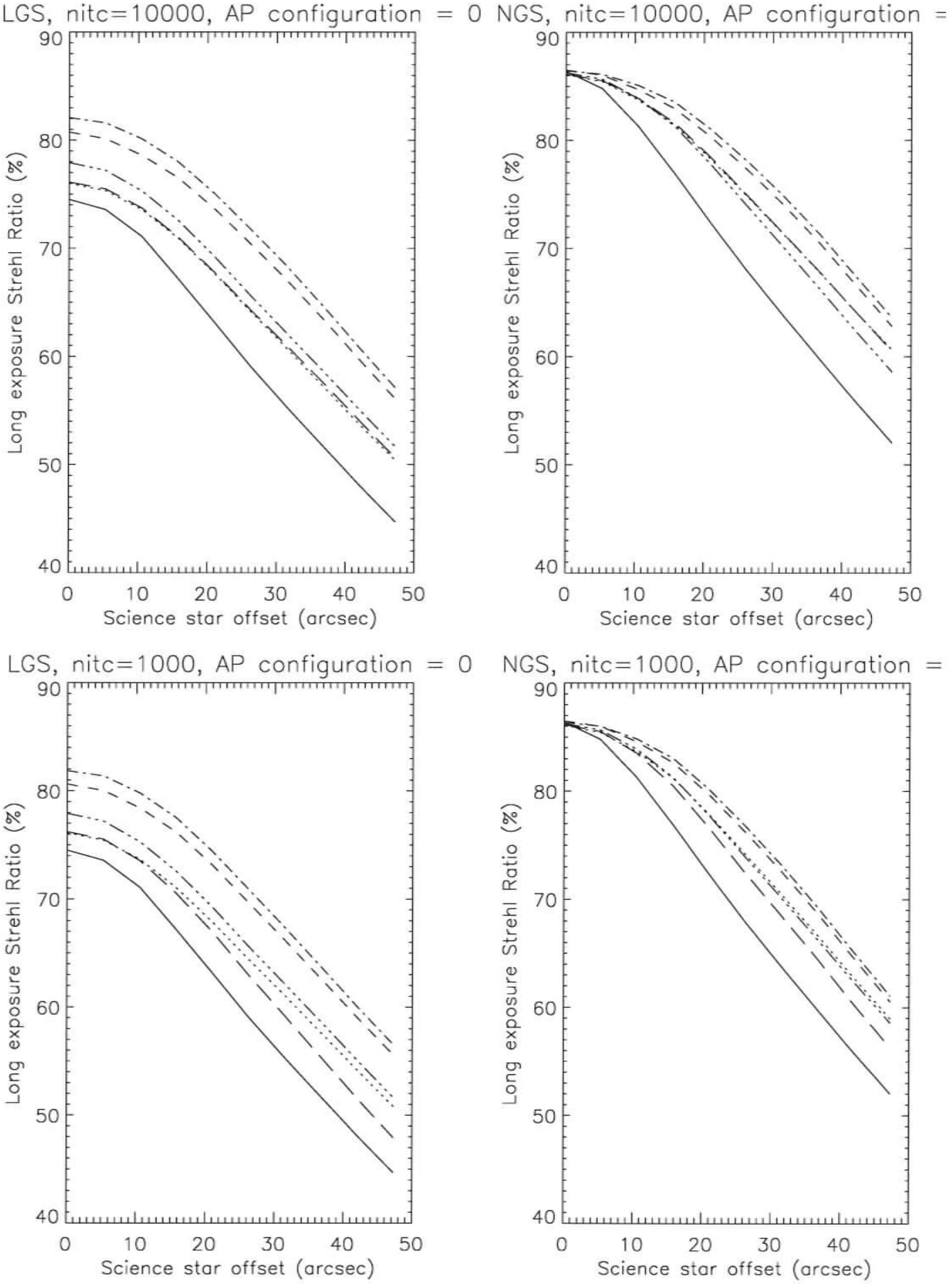

Figure 3.4 The Strehl ratio as a function of image star separation. The wavelength is $1.65\mu m$, the Gemini pupil $D = 7.906$ and $r_o = 0.838m$. The analysis pupil is centered on actuator 180 (central). No extrapolation (solid), *method 1*a (long dash), *method 1*b (dotted), nearest neighbour slaving (dash dot dot dot), *method 2*a (short dash), *method 2*b (dash dot).

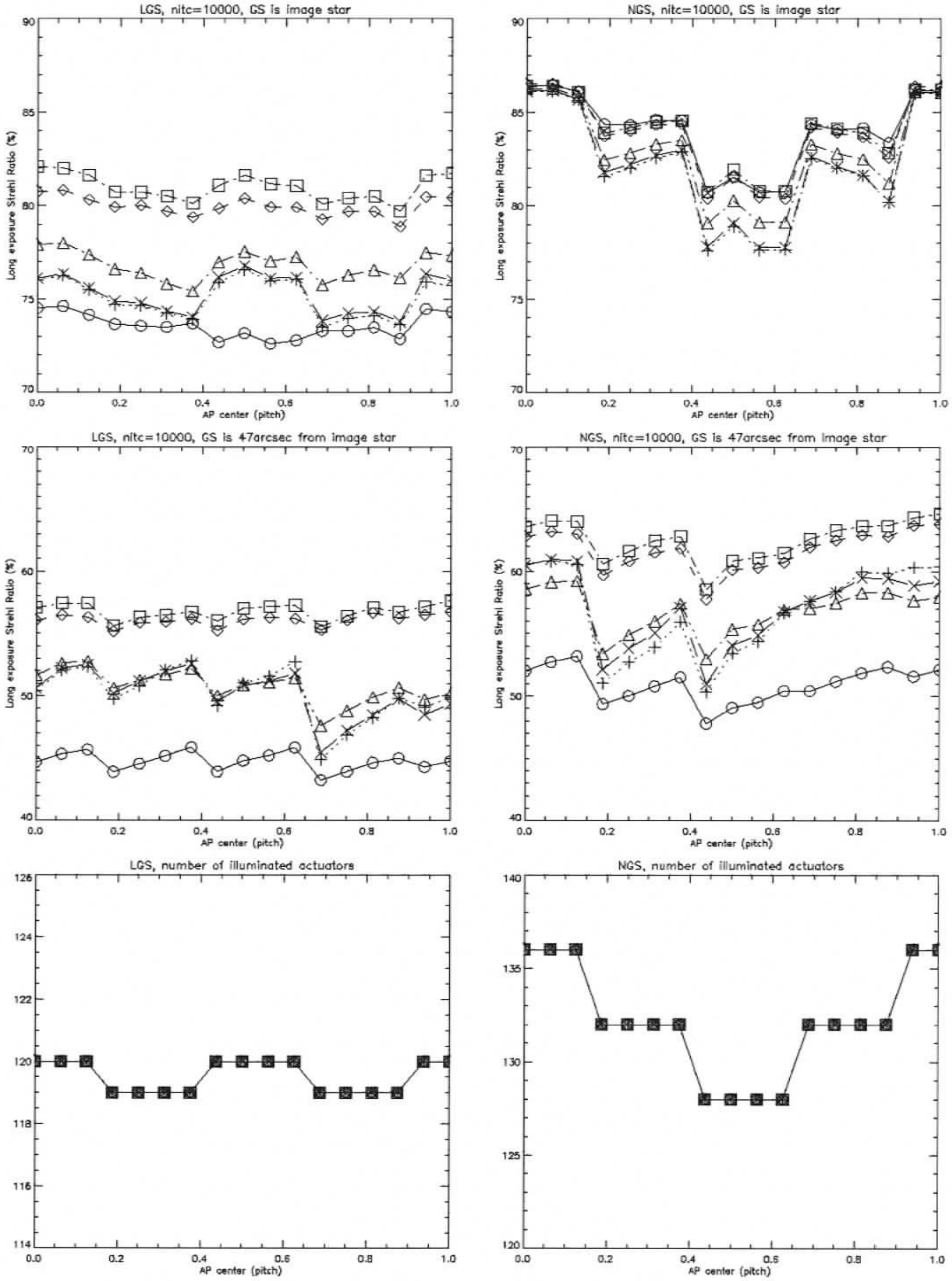

Figure 3.5 Similar to Fig.3.4. The Strehl ratio as a function of analysis pupil location (to the right of act 180) when the analysis and image pupils are separated by 0 arcseconds (top panels) and 47 arcseconds (middle panels). No extrapolation (circles), *method 1*a (x), *method 1*b (plus), nearest neighbour slaving (triangle), *method 2*a (diamond), *method 2*b (square). The number of actuators in the analysis pupil (i.e. length of $\boldsymbol{m}_{gs}$) for all covariance methods plotted in the bottom panels.

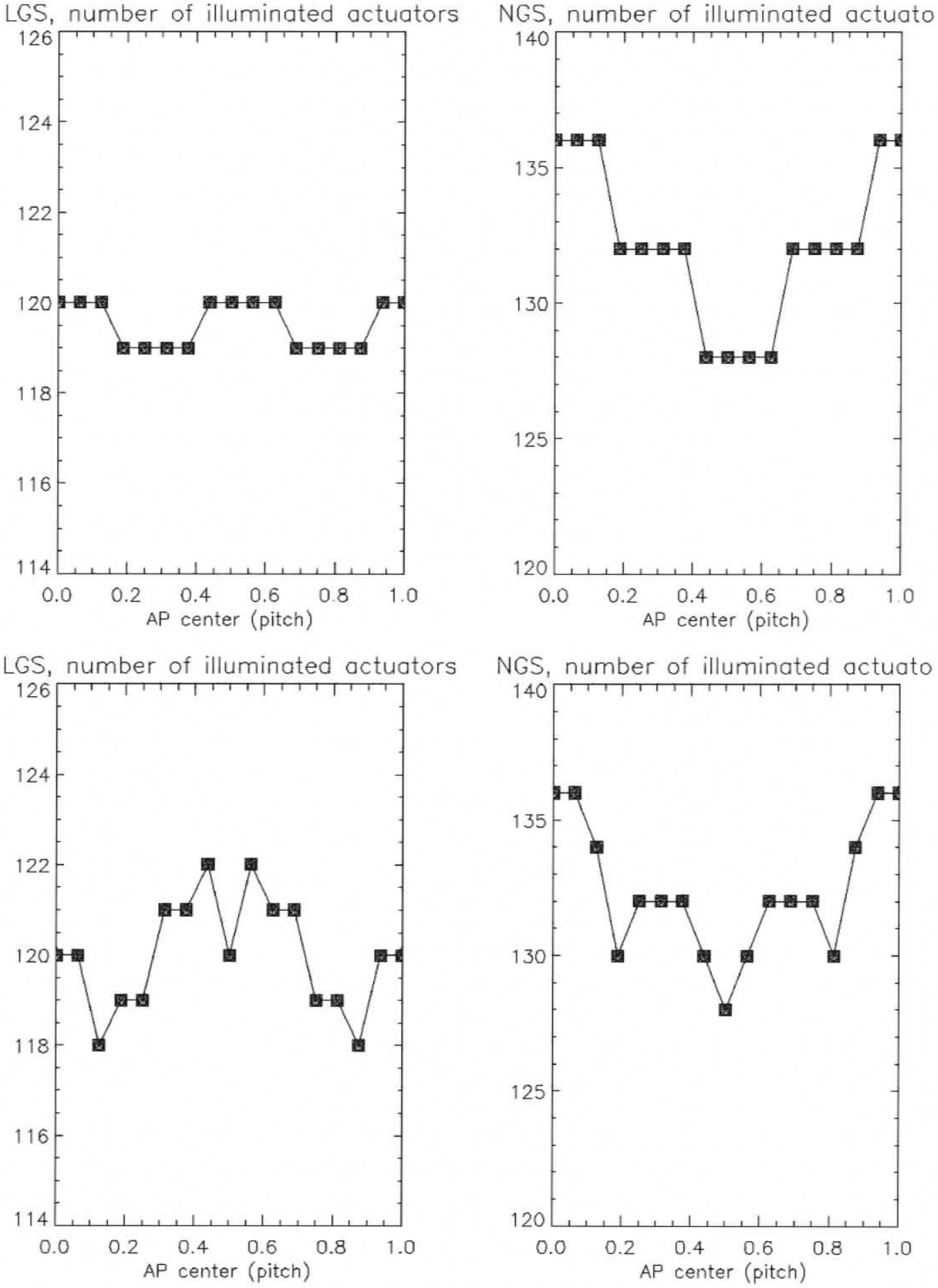

Figure 3.6 Top panels: the assumed length of $\boldsymbol{m}_{gs}$ actuators repeated from the bottom of Fig.3.5. Bottom panels: the length if membership was reassessed for each analysis pupil location.

(for *method 1*b, *method 2*a, and *method 2*b). The analysis pupil centers of five MC simulations are located at abscissa=[0,0.25,0.5,0.75,1]. The set of $\boldsymbol{m}_{gs}$ changed depending on which of these locations was closest (preference when to the right when equidistant). The negative effects of a finite number of precomputed covariance matrices are negligible compared to the effect of a changing number of $\boldsymbol{m}_{gs}$ actuators. In other words, it is not the extrapolation, but the correction inside the analysis pupil that is to blame for the small variation in SR in Fig.3.5. For the NGS case there is $\sim 5\%$ drop in SR from analysis pupil center at zero to 0.5 *pitch* at both on and off axis. nearest neighbour slaving and *method 1* show even more degradation than no extrapolation for NGS on axis, because of the poorly set $\boldsymbol{m}_{out}$ actuators having influence inside the on axis image pupil. In these tests the predefined analysis pupil locations for the MC simulations each require a particular set of $\boldsymbol{m}_{gs}$ and so we are forced to use these same sets for correction inside the analysis pupil. It is the poor correction inside the analysis pupil which dominates and is clearly visible in NGS results. It would help this virtual system if we could adjust the predefined locations so that the number of $\boldsymbol{m}_{gs}$ actuators was maximised for each location. Fig. 3.6 shows the number of $\boldsymbol{m}_{gs}$ allowed by the 4 of the 16 predefined locations (top pair of plots) and the numbers when reassessed by *altairInitGS* at each offset (bottom pair of plots). One can see that the configuation which is equidistant from actuator 180 and 181 has a minimum number of $\boldsymbol{m}_{gs}$ for the NGS case.

The ramping up that is visible in the middle two plots is due to the image patch moving closer to the $\boldsymbol{m}_{gs}$ actuators, which "move" in steps as the analysis pupil moves. The NGS off axis plot shows the combined effect of ramping and changing $\boldsymbol{m}_{gs}$ numbers.

3.6 Summary and Suggestions

Clearly *method 2*b offers the best performance for both the LGS and NGS cases because if fully accounts for vignetting at the edge of the analysis pupil. Some investigation needs to be done to determine the optimal number of edge actuators (defined by Eq. 3.23). The *method 1*a is better than *method 1*b because for the same performance only one covariance matrix Γ for any analysis pupil configuration is needed.

There are 16 analysis pupil locations for extrapolation defined in Altair's system design [V01]. The membership of actuators in $\boldsymbol{m}_{gs}$ plays a more significant role than finite number of pre-computed covariance matrix computation locations, hence 16 base locations is sufficient. However, out of those 16 analysis pupil locations 13 need unique covariance matrix computations. The number of unique computations can be reduced to 6 if the 4x4 grid of analysis pupil centers was shifted so that actuator 180 is in the center of the grid. Situations that would demand this type of economy are ones with a very large variety of analysis pupil configurations, e.g. multiple GS systems or an LGS pupil that changes with zenith angle. More suggested improvements are in Appendix B.1.

As an aside we make three caveats about the DM, WFS, and atmospheric models:

- The simulation of the DM was done with influence functions which define the DM shape by adding together. This is is a problem for our calculation at the edge of the virtual DM. The covariance matrix computation should to be done on a 21x21 virtual DM model to mitigate its inability to recreate a flat shape at the edge. If Altair wishes to place the analysis pupil more than one pitch away from the base central actuator, to extrapolate by as much as 4 pitches (84.6 arcseconds) then a 23x23 virtual DM is needed for computation of the covariance matrices.

- The projection method used in the simulation could benefit from a projection that is more a representative of a Shack-Hartmann WFS measurement. In the case of a finite virtual DM, the wavefront area seen by the quilt-work of subapertures is different from the area seen by the projection method we use with Eqn.(3.22). This is a problem for actuators which are not completely surrounded by illuminated subapertures (near the edges of the analysis pupil). This has been ignored and assumed negligible.

- We have calculated and tested the extrapolation for an infinite outer scale L_o. Doing so greatly simplifies the system design, as it makes the extrapolation matrix independent of r_o. However, an outer scale of 30 meters or less may have a noticeable effect on extrapolation.

Part Two

GLAO

Chapter 4

The GLiFFT model

4.1 Introduction

In this chapter we derive the spatial frequency domain formulae used in the analytic PSF model for ground layer AO (GLAO) called *GLiFFT* . The algorithm uses a fast Fourier transform (FFT) in computing the optical transfer function (OTF) from the phase power spectral density (PSD). The primary improvement here over the PSDs published in [SJV04, Tok04, JVC06] is anisoplanatism is re-derived for multiple wavefront references (also called beacons) at arbitrary range and with lag. We cautiously include back propagation to an altitude conjugation z'.

The derivation of the anisoplanatism PSD used in the rest of this work is in §4.2. The paper by [JVS04] is the first exact expression for a continuous distribution of beacons inside a disk on the sky. The papers by [SVR04, Tok04] each give the first exact expression for angular anisoplanatism of an arbitrary asterism of beacons, the latter also gives the exact expression for an arbitrary asterism of beacons at finite range (cone anisoplanatism). In §4.2 the formulae of these special cases are connected to the equations prented here. In addition to angular and cone anisoplanatism, we include lag anisoplanatism in the formulation under the assumption of the Taylor hypothesis.

The computation algorithm is described in §4.3. Using an FFT implies periodic boundaries. The array size that the PSD is defined on must be sufficiently large so that the results are representative of results a Fourier transform with proper infinite boundaries. The *GLiFFT* code gets its name by iterating a few times to eliminate these FFT numerical effects. Iterating is method of speeding up the computation, which is especially important to GLAO where, because of the temporal and spatial variability of the GLAO PSF, needs to be done hundreds of times for a given system and site. We illustrate the PSD sampling effects on the GLAO PSF in §4.3.1.

4.2 The model PSD

The standard spatial frequency domain model (e.g. [RVL98, TLS00]) for the AO corrected phase (also called residual phase) can be separated into at least three terms of phase PSD from the uncorrelated effects: fitting error, WFS noise, and anisoplanatism.

$$W_{\phi_r}(\boldsymbol{f}) = W_{fit}(\boldsymbol{f}) + W_{noise}(\boldsymbol{f}) + W_{aniso}(\boldsymbol{f}). \tag{4.1}$$

where f is the spatial frequency of the wavefront projected onto the primary mirror (called the pupil plane hereafter). For simplicity we choose an actuator spacing Δ on a square grid in the pupil plane. Moreover we assume actuator influence functions (cf. Chapter 3) that are $sinc(\Delta x)sinc(\Delta y)$ so that the fitting error term (W_{fit}) for f_x and $f_y > (2\Delta)^{-1}$ is the atmospheric PSD Eqn.(4.12) and zero elsewhere, which matches reality fairly well. Similarly, the other terms are non-zero only where f_x and $f_y \leq (2\Delta)^{-1}$. This is sometimes called a square actuator geometry and the box it defines in the PSD is called the control box. We also assume the subaperture geometry and spacing are matched to that of the actuators on the deformable mirror (DM). We will call the matched spacing pitch (or Δ) hereafter and only allow it to have values that divide the pupil (of diameter D) into an integer number of pitches (N_p).

$$\Delta \equiv \frac{D}{N_p}, \quad \text{where } N_p \text{ is an integer.} \tag{4.2}$$

4.2.1 Anisoplanatism PSD

The anisoplanatism phase PSD starts with the residual phase at $\boldsymbol{x}$ in the pupil plane.

$$\phi_r(\boldsymbol{x}) = \phi(\boldsymbol{x}) - \overline{\phi}(\boldsymbol{x}) \tag{4.3}$$

The phase on the deformable mirror $\overline{\phi}(\boldsymbol{x})$ will be integrated from lines of sight different from $\phi(\boldsymbol{x})$. Using the small angle approximation the phase integrated through N_L discrete layers at an angle $\boldsymbol{\theta}_m$ from the $\hat{z}$ direction (see Fig.4.1) is

$$\phi_m(\boldsymbol{x}) = \sum_{n=1}^{N_L} \phi_n\left(\boldsymbol{x} + \boldsymbol{\theta}_m z_n\right). \tag{4.4}$$

In the case where the beacon is not at infinity, illuminating a cylindrical volume of turbulence above the telescope, but rather a cone with its vertex at range H and forming the small angle of D/H the integrated phase is

$$\begin{aligned} \phi_m(\boldsymbol{x}) &= \textstyle\sum_{n=1}^{N_L} \phi_n\left(\boldsymbol{x}\gamma_n + \boldsymbol{\theta}_m z_n\right), \\ &\text{where } \gamma_n = 1 - \tfrac{z_n}{H}. \end{aligned} \tag{4.5}$$

To simulate WFS and DM conjugation at range z' we can back project the phase by subtracting z' from the range of each layer. After some algebra we get

$$\begin{aligned} \phi'_m(\boldsymbol{x}) &= \textstyle\sum_{n=1}^{N_L} \phi_n\left(\frac{\boldsymbol{x}-\boldsymbol{\theta}_m z'}{\gamma'}\gamma_n + \boldsymbol{\theta}_m z_n\right), \\ &\text{where } \gamma_n = 1 - \tfrac{z'}{H}. \end{aligned} \tag{4.6}$$

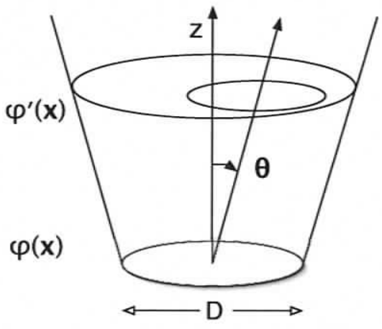

Figure 4.1 The phase at the pupil ($\phi(\boldsymbol{x})$) and at the metapupil ($\phi'(\boldsymbol{x})$). The direction of a line of sight is identified by the angle $\boldsymbol{\theta}$ with respect to the optical axis.

This formulation is well suited to transformation to the Fourier domain, however a nonzero z' implies integration of phase along impossible to view lines of sight for a finite aperture. Rigorous treatment of these edge effects is sometimes referred to as the assumption of an infinite aperture. We will avoid this assumption and model only ground conjugation here ($z' = 0$).

Using the Taylor assumption of frozen flow (recall §1.2.3) the integration of the phase in the time interval Δt is written

$$\phi_m(\boldsymbol{x}) = \left\langle \sum_{n=1}^{N_L} \phi_n\left(\boldsymbol{x}\gamma_n + \boldsymbol{\theta}_m z_n - \boldsymbol{v}_n \tau\right) \right\rangle_{\Delta t}. \tag{4.7}$$

The angle brackets denote the time average over the WFS integration time Δt. Using the similar notation as [JVC06] the separation of pure lag t_{lag} from WFS integration time Δt gives a total lag $\tau = \Delta t/2 + t_{lag}$.

The Fourier transform of Eqn.(4.7) involves the shift and scaling theorems as well as a boxcar average in the $\boldsymbol{v}_n$ direction.

$$\widetilde{\phi_m}(\boldsymbol{f}) = \sum_{n=1}^{N_L} \frac{1}{\gamma_n}\widetilde{\phi_n}\left(\frac{\boldsymbol{f}}{\gamma_n}\right) \; L_n(\boldsymbol{f}) \; G_{m,n}(\boldsymbol{f}) \tag{4.8}$$

and we define

$$\begin{aligned} L_n(\boldsymbol{f}) &= \exp\left(2\pi i \frac{\boldsymbol{f}\cdot\boldsymbol{v}_n\tau}{\gamma_n}\right) \operatorname{sinc}\left(\frac{\boldsymbol{f}\cdot\boldsymbol{v}_n\Delta t}{\gamma_n}\right), \\ G_{m,n}(\boldsymbol{f}) &= \exp\left(2\pi i \frac{\boldsymbol{f}\cdot\boldsymbol{\theta}_m z_n}{\gamma_n}\right). \end{aligned}$$

The tilde over the phase denotes the expectation value of the Fourier transform.

The superposition of measurements from a finite number of beacons is then

$$\overline{\phi}(\boldsymbol{x}) = \sum_{m=1}^{N} w_m \phi_m(\boldsymbol{x}) \;\; \text{and} \;\; \sum_{m=1}^{N} w_m = 1, \tag{4.9}$$

where ϕ_m is the contribution from the m^{th} beacon, weighted by w_m.*

Finally, putting Eqn.(4.9) with Eqn.(4.8) into Eqn.(4.3) the residual phase is

$$\widetilde{\phi_r}(\boldsymbol{f}) = \sum_{n=1}^{N_L}\left[\widetilde{\phi_n}(\boldsymbol{f}) - \sum_{m=1}^{N} w_m \frac{1}{\gamma_n}\widetilde{\phi_n}\left(\frac{\boldsymbol{f}}{\gamma_n}\right) \; L_n(\boldsymbol{f}) \; G_{m,n}(\boldsymbol{f})\right]. \tag{4.10}$$

Assuming that the phase in the N_L layers is uncorrelated then

$$\begin{aligned} W_{aniso}(\boldsymbol{f}) &= \left[\widetilde{\phi_r}(\boldsymbol{f})\right]^2 \\ &= \sum_{n=1}^{N_L}\left[\widetilde{\phi_n}(\boldsymbol{f}) - \sum_{m=1}^{N} w_m \frac{1}{\gamma_n}\widetilde{\phi_n}\left(\frac{\boldsymbol{f}}{\gamma_n}\right) \; L_n(\boldsymbol{f}) \; G_{m,n}(\boldsymbol{f})\right]^2. \end{aligned} \tag{4.11}$$

Recall that we have chosen

$$\widetilde{\phi_n}(\boldsymbol{f}) = \left[0.0229 \; r_{o_n}^{-5/3}\left(\frac{1}{L_o^2} + \boldsymbol{f}^2\right)^{-11/6}\right]^{1/2}. \tag{4.12}$$

---

*In the case where each beacon in the asterism provides sufficient WFS flux for noiseless operation, then an optimal w_m could be found to redistribute correction across the whole field of view to compensate for an irregular asterism.

Eqn.(4.11) is the general form of the anisoplanatism PSD that includes lag and cone anisoplanatism when H is finite and $\gamma_n \neq 1$. When $\tau = 0$ then $L_n(\boldsymbol{f}) = 1$ and Eqn.(4.11) becomes purely angular and cone anisoplanatism.

Special cases of the anisoplanatism PSD

If $L_o \to \infty$ then Eqn.(4.12) becomes the Kolmogorov power law and using the scaling theorem of Fourier transforms we could write

$$\widetilde{\phi_n}\left(\frac{\boldsymbol{f}}{\gamma_n}\right) = \left(\frac{1}{\gamma_n}\right)^{-11/6} \widetilde{\phi_n}(\boldsymbol{f}). \tag{4.13}$$

Regardless of L_o, for the Natural Guide Star (NGS) case $H \to \infty$ and $\gamma_n \to 1$ meaning we could then write the anisoplanatism PSD as the product of the atmospheric PSD and a filter. Eqn.(4.11) would become

$$W_{aniso}(\boldsymbol{f}) = \sum_{n=1}^{N_L} \left[\widetilde{\phi}_n(\boldsymbol{f})\right]^2 \left[1 - \sum_{m=1}^{N} w_m \; L_n(\boldsymbol{f}) \; G_{m,n}(\boldsymbol{f})\right]^2. \tag{4.14}$$

Let us consider hypothetical cases with an infinite number of NGSs which means infinite wavefront signal in an arbitrarily short WFS is not much use for the lag factor $L_n(\boldsymbol{f})$ and we set it to unity. If the NGS are continuously distributed over a circle of radius θ_r we can rewrite the sum in the second term in Eqn.(4.14) as the continuous integral of beacons, each occupying an infinitesimal fraction of the circle's area $d\boldsymbol{\theta}/\pi\theta_r$,

$$\int_{circ(\theta_r)} \frac{d\boldsymbol{\theta}}{\pi\theta_r^2} \exp\left(2\pi i \boldsymbol{f} \cdot \boldsymbol{\theta} z_n\right). \tag{4.15}$$

Using the substitutions

$$R_n = \theta_r z_n \quad \text{and} \quad \boldsymbol{r}_n = \boldsymbol{\theta} z_n, \tag{4.16}$$

$$\boldsymbol{f} \cdot \boldsymbol{r}_n = f r_n \cos\beta \quad \text{and} \quad d\boldsymbol{r}_n = r_n d\beta dr_n \tag{4.17}$$

we get the form of the integral that clearly generates the Airy function.

$$\int_0^{2\pi} \int_0^{R_n} \frac{r_n d\beta dr_n}{\pi R_n^2} \exp\left(2\pi i f r_n \cos\beta\right) = \frac{2J_1(2\pi f R_n)}{2\pi f R_n} \tag{4.18}$$

where J_1 is the first order Bessel function of the first kind. Hence,

$$W_{aniso}(\boldsymbol{f}) = \sum_{n=1}^{N_L} \left[\widetilde{\phi}_n(\boldsymbol{f})\right]^2 \left[1 - \frac{2J_1(2\pi f R_n)}{2\pi f R_n}\right]^2 \tag{4.19}$$

as first published in [JVS04]. If the second term is instead integrated over a ring of radius θ_r the second term becomes a zeroth order Bessel function leading to

$$W_{aniso}(\boldsymbol{f}) = \sum_{n=1}^{N_L} \left[\widetilde{\phi}_n(\boldsymbol{f})\right]^2 [1 - J_0(2\pi f R_n)]^2 . \tag{4.20}$$

as first published in [Tok04].

4.2.2 WFS noise PSD

The noise PSD is shown to be negligible for the modeling work presented in Chapter 5 and 6 but is included here for completeness. For a sum of wavefront measurements from N Shack-Hartmann WFS

$$W_{noise}(\boldsymbol{f}) = \sum_{m=1}^{N} w_m |\tilde{\mathcal{R}}(\boldsymbol{f})|^2 \sigma_{noise}^2 \text{ and } \sum_{m=1}^{N} w_m = 1 \tag{4.21}$$

where $\tilde{\mathcal{R}}$ is the reconstructor operator for the WFS(s) and σ_{noise}^2 is the variance in the WFS measurements due to photon and read noise (see [RVL98, V04]). The reconstructor propagates the noise in the WFS measurements to the corrected phase. Modeling the SH WFS as an ideal slope sensor

$$|\tilde{\mathcal{R}}_{SH}(\mathbf{f})|^2 = \frac{1}{4\pi^2 f^2 \text{sinc}^2(\Delta\ f_x)\text{sinc}^2(\Delta\ f_y)} \tag{4.22}$$

where Δ is the sub-aperture size.

$$\sigma_{noise}^2 = \left(\frac{2\pi}{\lambda_{obs}}\right)^2 \Delta^2 \left(\frac{\theta_b}{SNR}\right)^2 \tag{4.23}$$

where λ_{obs} is the central wavelength used in the observation, θ_b is the half-width at half-maximum of the spot size, and SNR is the signal-to-noise ratio of the flux on a typical lenslet image from which the slope is derived. Although SNR is part of the minimal parameter set, we will expand on its meaning for the sake of clarity. For the m^{th} WFS

$$SNR_m = \frac{S}{\sqrt{S + B + RON}}, \tag{4.24}$$

where the terms in the denominator are the beacon flux, background flux, and read out noise all in photoelectrons accumulated in the portion of the WFS CCD that was used to compute the slope. For N WFS with identical registration and beacon flux, bacground, and RON

$$SNR = \sqrt{N}\; SNR_m. \tag{4.25}$$

4.3 The algorithm to compute the PSF from the phase PSD

The Wiener-Khinchin theorem relates the PSD of a quantity to its covariance. Thus the two-dimensional phase covariance in terms of the PSD with units in radians squared of wavefront variance per unit f is

$$\begin{aligned} B_\phi(\boldsymbol{\xi}) &= FT[W_\phi(\boldsymbol{f})] \\ &= \int_{-\infty}^{\infty}\int_{-\infty}^{\infty} df_x\, df_y\; e^{-2\pi \boldsymbol{f}\cdot\boldsymbol{\xi}}\; W_\phi(\boldsymbol{f}). \end{aligned} \tag{4.26}$$

Since the covariance and PSD have even symmetry the inverse Fourier transform (FT) will be the same $W_\phi(\boldsymbol{f}) = FT[B_\phi(\boldsymbol{\xi})] = FT^{-1}[B_\phi(\boldsymbol{\xi})]$. Using the relationship between the covariance and the OTF (recall §1.3.2) the two-dimensional OTF is

$$S_\phi(\boldsymbol{\xi}) = exp[-B_\phi(0) + B_\phi(\boldsymbol{\xi})] \tag{4.27}$$

This OTF is for an infinite aperture, as the integral Eqn.(4.26) is over all spatial frequencies. It can be shown that the integral Eqn.(4.26) weighted by $1 - I_T(\boldsymbol{f} = \boldsymbol{\alpha}/\lambda)$, where I_T is the diffraction limited PSF results in the total OTF. It is however more efficient to compute the total OTF as the product of $S_\phi S_T$, where S_T is the telescope OTF.

$$S(\boldsymbol{\xi}) = S_T(\boldsymbol{\xi})\; exp[-B_\phi(0) + B_\phi(\boldsymbol{\xi})]. \tag{4.28}$$

The PSF is then

$$I(\boldsymbol{\alpha}) = FT^{-1}[S(\boldsymbol{\xi}/\lambda)]. \tag{4.29}$$

The PSD we start with uses an expectation value (Eqn.(4.12)) meaning that $S(\boldsymbol{\xi})$ and $I(\boldsymbol{\alpha})$ are also the expectation. In other words $I(\boldsymbol{\alpha})$ will be an infinite time average and there will be no speckles.

4.3.1 PSD sampling and numerical effects in the PSF

An FFT is a discrete FT and therefore only a linear transformation of coordinates for $\boldsymbol{f}$ and $\boldsymbol{\xi}$ can preserve Parceval's theorem. In other words the integral Eqn.(4.26) must be sampled on a regular grid with sampling Δf. Since S_T is zero for $\xi > D$, the telescope diameter, it suggests that

$$\Delta f \lessapprox \frac{1}{4D} \tag{4.30}$$

to adequately sample near the origin. Modulation of the PSD sets another constraint on Δf. Looking back to Eqn.(4.8), we see modulation of the residual PSD by $L_n(\boldsymbol{f})$ at a period $(\boldsymbol{v}_n\tau)$ meters and $G_{m,n}(\boldsymbol{f})$ at $\boldsymbol{\theta}_m z_n$ meters. We therefore require

$$\Delta f \leq \frac{1}{max(\boldsymbol{v}_n\tau)} \quad \text{and} \tag{4.31}$$

$$\Delta f \leq \frac{1}{max(\boldsymbol{\theta}_m z_n)}. \tag{4.32}$$

Aliasing of the PSD could cause a serious bias for Δf that is larger than this. For reasonable input parameters the largest modulation by $(\boldsymbol{v}_n\tau)$ would typically be 10 times less than from $(\boldsymbol{\theta}_m z_n)$. For example, maximum $v_n = 70m/s$ winds and $\tau = 0.01s$ lag time, leads to a modulation requiring $\Delta f \leq 0.714m^{-1}$. An example of an extreme case of $(\boldsymbol{\theta}_m z_n)$ would be a PSF computed at the edge of an asterism 2 arcminutes in diameter and an atmosphere with no turbulence above $12km$ requires $\Delta f \leq 0.0716m^{-1}$.

An example GLAO PSD (W_{ϕ_r}) evaluated with no wind and a four beacon asterism with 1, 4, and 17 arcminute diameter is shown in panels a), b), and c) of Fig.4.2. They have the same outer scale, cut and stretch levels as the atmospheric PSD (W_ϕ) in panel d). The variance inside the square area controlled by the deformable mirror (f_x and $f_y \leq (2\Delta)^{-1}$) is from anisoplanatism of layers in the *gray zone.* Tokovinin [Tok04] coined the term *gray zone* that refers to the volume of the turbulence that is being smoothed by averaging the wavefront from multiple beacons. The bottom of the *gray zone* is at a range of $z - z' = \Delta/(2\theta_r)$.[†] This corresponds to a PSF centered in an ring of beacons at a radius $\theta_r = \theta/2$ with the first maximum of the filter in Eqn.(4.20) at $f = 0.6(\theta_r z)^{-1} = 2.4(2\Delta)^{-1}$, far outside the controlled area. Layers contribute variance proportional to $r_{o_n}^{-5/3}$ (cf. Eqn.(4.12)) with significant modulation contribution from the highest layer due to its thickness. No aliasing is present in Fig.4.2 as *GLiFFT* computations satisfy the Δf requirments Eqn.(4.30), Eqn.(4.31), and most importantly Eqn.(4.32).

As previously stated, an FFT implies periodic boundaries and the array size that the PSD is defined on must be sufficiently large so that the results are representative of a Fourier transform with proper infinite boundaries. Increasing the width of the regular square grid $N = 2f_{max}/\Delta f$ on which the OTF and subsequent PSF are computed will give an asymptotic approach to the true PSF. Using the same Cerro Pachon atmospheric conditions as in Fig.4.2 and fixing Δf for the requirements above we reduce $1.25\mu m$ PSFs to radius of 50% encircled energy[‡] (EE50) and fit the asymptote of the function $EE50(N) = a_o + a_1/N$ in Fig.4.3. To fit each curve there are four iterations of $f_{max} = [4/r_o,\ 8/r_o,\ 12/r_o,\ 16/r_o]$ ($r_o(\lambda = 1.25\mu m) = 0.107m$). The different curves are for different telescope diameters D. The left panel is the GLAO PSD model with four beacons at a diameter $\theta = 17$ arcminutes and on the right is the seeing limited PSD model. We can confirm from the plot that the numerical error in EE50 reduces to about 1% for $f_{max} = 12/r_o$.

The computation time of a PSF is limited by the FFTs, roughly proportional to $N^2 \log N^2$. Repeated in three iterations with $f_{max} = [4/r_o,\ 8/r_o,\ 12/r_o]$ would be just ~56% longer than one at $f_{max} = 12/r_o$ but would reduce error in EE50 to many times less than 1%. The interative calculation can work on any PSF metric or even rebined parts of the PSF for reconstructing an entire asymptotic PSF. In Fig.4.4 are the PSFs corresponding to the PSDs in Fig.4.2. The subtle differences between the two wide field GLAO cases, panels b) and c), tempt the creation of a

---

[†] Note that if the DM is conjugated too high, there is a gray zone below the DM as well.

[‡] Refer to §1.3.3 for an illustration of encircled energy.

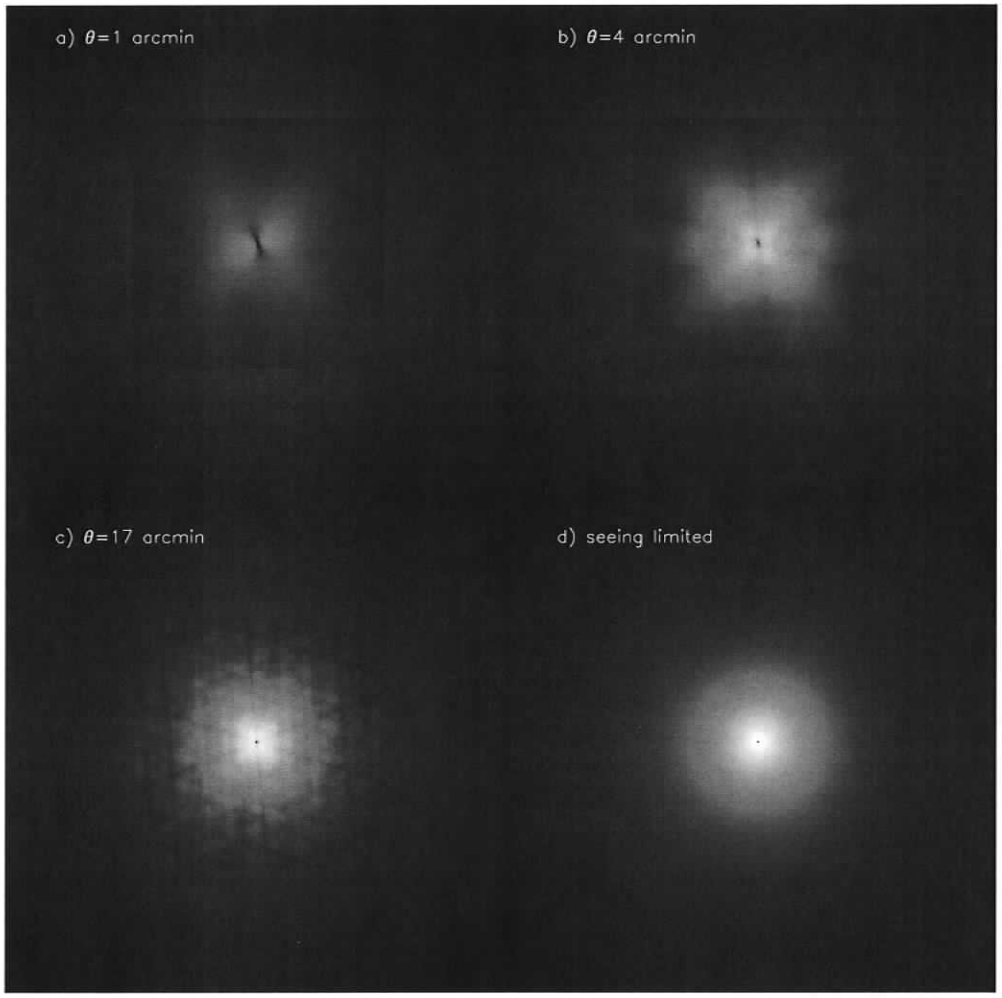

Figure 4.2 Example GLAO PSDs for $\theta = 1, 4$, and 17 arcminutes and $\Delta = 1$ meter in panels a), b), and c). The asterism is four beacons at the vertices of a box that is off center. Panel d) shows the seeing limited PSD. All PSDs have an outer scale of 30 meters and the typical Cerro Pachon C_n^2 model (solid lines in Fig.1.2). All panels have the same log stretch and cut levels.

new image quality metric for comparison to the seeing limited PSF d). In Chapter 5 we will define and use such a metric.

4.4 Summary

The theory and implementation of a PSF model using analytic formulae in the PSD for accurate computation of anisoplanatism has been derived and illustrated. We

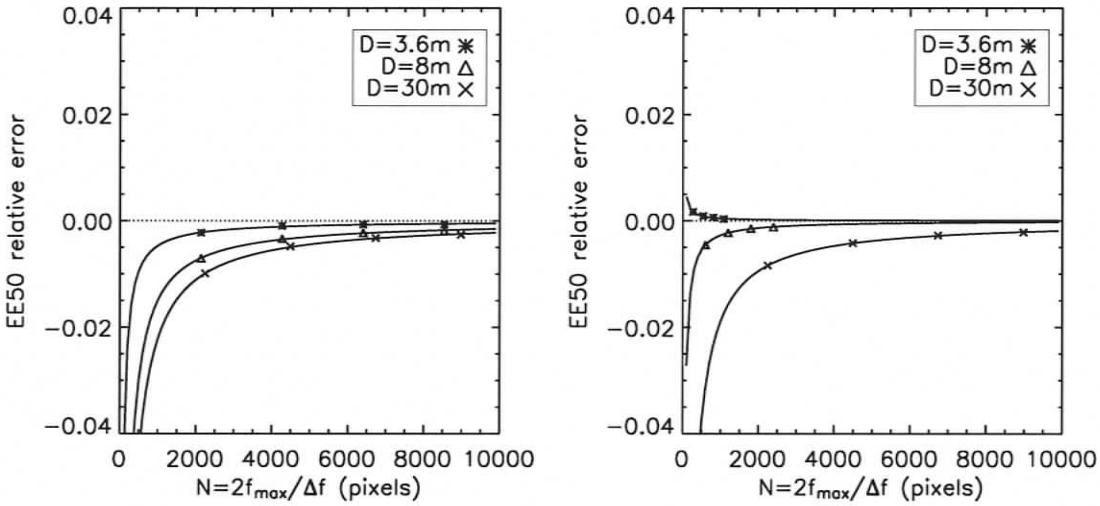

Figure 4.3 The radius of 50% encircled energy (EE50) relative to the asymptote of the fitting function $EE50(N) = a_o + a_1/N$ (solid curves) where N is the width of the square grid used to compute the OTF and PSF. The left panel is the GLAO PSD model and the right panel is the seeing limited PSD model. One can see that for the GLAO $D = 3.6m$ and $8m$ cases (asterisks and triangles) the PSD anti-aliasing requirement Eqn.(4.32) dictates Δf, otherwise the telescope diameter Eqn.(4.30) dictates Δf.

proceed with this anisoplanatism model and algorithm, accurate in the wide field cases shown in panels b), c), and d) in the above figures.

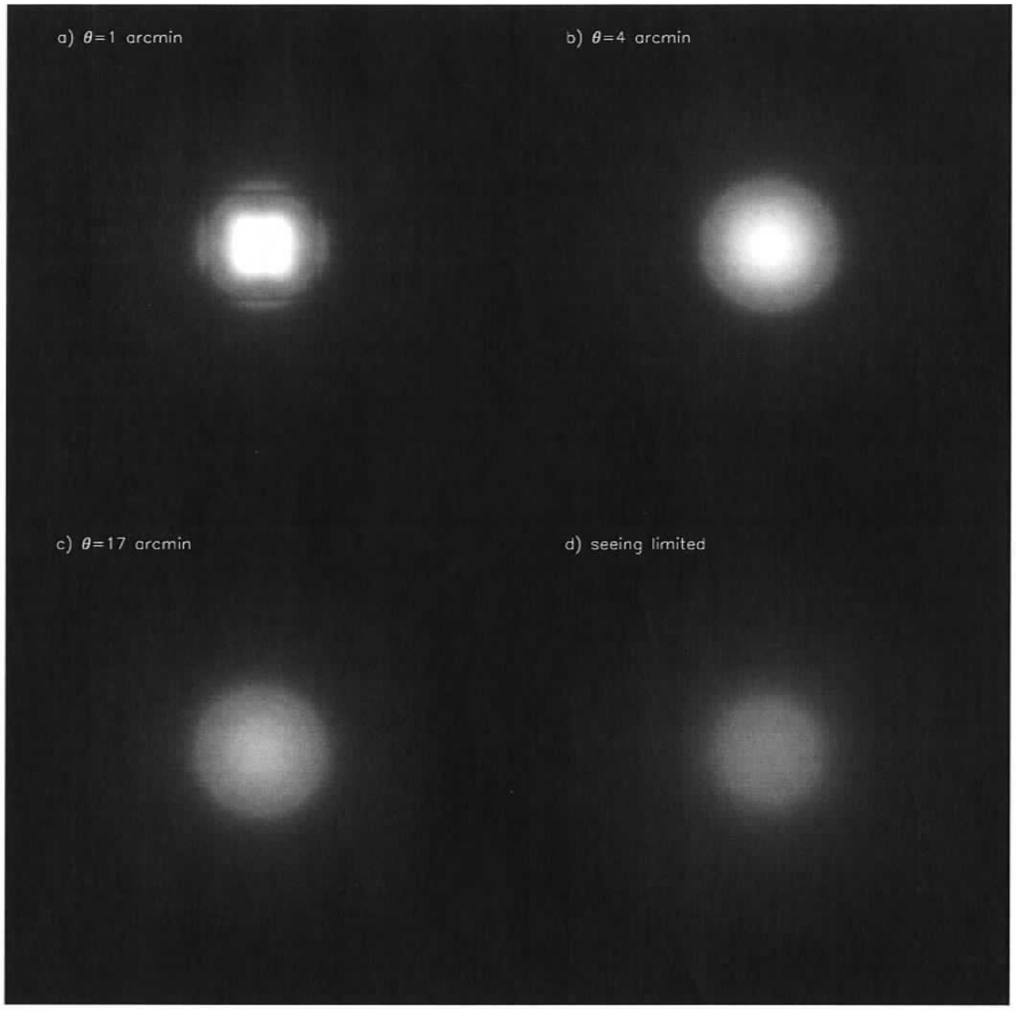

Figure 4.4 The PSFs corresponding to the PSDs in Fig.4.2 with a 30 meter circular aperture and $\lambda = 1.25$. All panels have the same cut levels and this time a linear stretch to show the subtle differences between the $\theta = 4, 17$ arcminutes and seeing limited case. The $\theta = 1$ arcminute PSF has a noticeable Strehl, much higher than the upper cut level.

Chapter 5

Constraining the GLAO parameter space

This chapter and parts of Chapter 4 is work to be submitted to *Publications of the Astronomical Society of the Pacific.*

Abstract:

Nature provides reduced turbulence at intermediate altitudes and as a result the mean image quality of a ground layer adaptive optics (GLAO) corrected field degrades slowly with increasing field diameter. If this function has a shallow slope all the way out to the maximum seeing limited field of view of the telescope then surveys at that telescope may significantly benefit from GLAO. Using published optical turbulence profile models for Cerro Pachon we identify the useful gains of GLAO as the very wide GLAO (VWGLAO) regime. This is shown with two example telescope and science scenarios. We also show that using only four sodium laser guide stars the very wide GLAO system with optimal actuator and subaperture pitch will not be affected by servo lag and wavefront sensor noise.

5.1 Introduction

Ground Layer Adaptive Optics (GLAO) is a concept where the atmospheric layers of optical turbulence closer to the ground are corrected, the mid-altitude layers are partly corrected and high layers not at all. As described in the seminal paper by [Rig02] the ground layers are targeted because their correction is easily measured over wide fields of view. Image correction by GLAO when providing large uniform corrected fields is best described as improved seeing (e.g. [Tok04, LH06, SVR06, ACS06]). GLAO modeling confirms that this description applies to a wide range of corrected fields of view, from a few to 30 arcminutes, sometimes more, depending on the low altitude turbulence.

There are numerous considerations that influence the actual usable field of view for the current and next generation of large telescopes for the visible and infrared wavelengths. Such considerations include over-sizing the primary mirror to reduce infrared background light, or baffles to block scattered light, the availability of large format CCDs or detectors, elimination of static aberrations with tertiary lenses or mirrors, and of course the scientific goals for the telescope. These considerations for the field of view are just a small part of the vast topic and are beyond the scope of this chapter. In this chapter we use just two assumed telescopes scenarios at one site to illustrate the VWGLAO regime and to characterize the fundamental adaptive optics (AO) error terms.

Most large telescopes will use several types of AO to achieve their full potential and one of those will inevitably be GLAO ([EBD05, HEA06]). With proven advances in AO, and the advent of the adaptive secondary mirror the idea of building adaptive telescopes is being realized. Because the adaptive secondary is naturally conjugated near the ground, the type of AO that an adaptive telescope will always be capable of is GLAO. This means that the low altitude turbulence will certainly but eventually become one of considerations for designing the field of view of a telescope.

In §5.2 we describe the PSF model. In §5.3 we define the input to the model and set up the VWGLAO system. §5.4 gives predictions for two simple science cases optimized for VWGLAO. The predictions are for monochromatic point sources only, but more importantly we define the VWGLAO regime and show that these systems will not be limited by wavefront error caused by noise or lag.

5.2 The PSF model

The *GLiFFT* PSF model used here is coded in IDL and defined in terms of the phase power spectral density (PSD) described in Chapter 4. In the VWGLAO regime the angular anisoplanatism and fitting error, dominate over wavefront aliasing, lag, noise, and scintilation. The anisoplanatism model is used with simple wavefront averaging with all beacons given the same weight. We use lag anisoplanatism only to estimate the upper bound on WFS integration time Δt^{+} in §5.4.3.

The *GLiFFT* algorithm is similar to *PAOLA* [JVC06] using a fast Fourier transform (FFT) to compute the optical transfer function (OTF) which is multiplied by the telescope OTF. The PSF is then the result of another FFT on the OTF. Using an FFT implies periodic boundaries and the array size that the PSD is defined on needs to be sufficiently large so that the results are representative of results an Fourier transform with proper infinite boundaries.

Numerical errors caused by the periodic boundary conditions affect the plots in §5.4 by less than 5%. For the ITRS cases ($\lambda = 1.25\mu m$) described in the following sections, the PSD was evaluated out to $f_{max} = 16/r_o$, which corresponds to a PSF radius of λf_{max} =6 to 19 arcseconds, depending on the C_n^2 profile. The ITR cases ($\lambda = 0.6\mu m$) required only $f_{max} = 8/r_o$ corresponding to a 3.5 to 12 arcsecond PSF radius. To prevent aliasing in the anisoplanatism PSD one must select the correct sampling, Δf discussed in §4.3.1. The range in array size used here is $f_{max}/\Delta f =$ 1500 to 4700 for the ITRS cases and 700 to 8000 for the ITR cases. When the plots are regenerated with $f_{max}/4$ there is as much as a 20% error in ITRS (Fig.5.5).

When regenerated with $f_{max}/2$ there is no perceptible difference in any of the plots in §5.4 and we therefore estimate numerical errors are less than 5% on the ordinate for plots with two decades and less than 2.5% for plots with one.

5.3 Initial constraints on the VWGLAO parameter space

Here we will define the focal plane, including beacon type and asterism. We define two telescope scenarios, each with its own observing scenario. The atmospheric models include profiles of the refractive index structure constant $C_n^2(h)$ and the wind velocity $\boldsymbol{v}_n(h)$. We also discuss deformable mirror conjugation.

5.3.1 The telescope and its field of view

Survey science cases that we consider use a true seeing improvement system with a uniform PSF across a contiguous field. For this reason we will not locate beacons in the science field because they either cause vignetting from pick-off mirrors, or in the case using a dichroic, a non-uniform and unstable PSF in the neighborhood of the beacon. A square science detector fits nicely inside an asterism of four or eight beacons, as shown in Fig.6.2. We define the field of view using only the diameter of the circle θ, which meets the vertices of the the square science field. The diameter, θ, should not be confused with $\boldsymbol{\theta}_m$, the vector coordinate of the m^{th} guide star. We keep these two configurations constant and scale them with θ. They are considered optimal, though further study of PSF uniformity and stability in the neighborhood of a beacon may change this.

The definition of the seeing limited field of view for the telescope, with diameter θ_{max}, is germane to the search for the GLAO field of view θ. We consider D =3.6 and 8 meter telescopes and choose them to have a θ_{max} =26 and 13 arcminutes respectively.

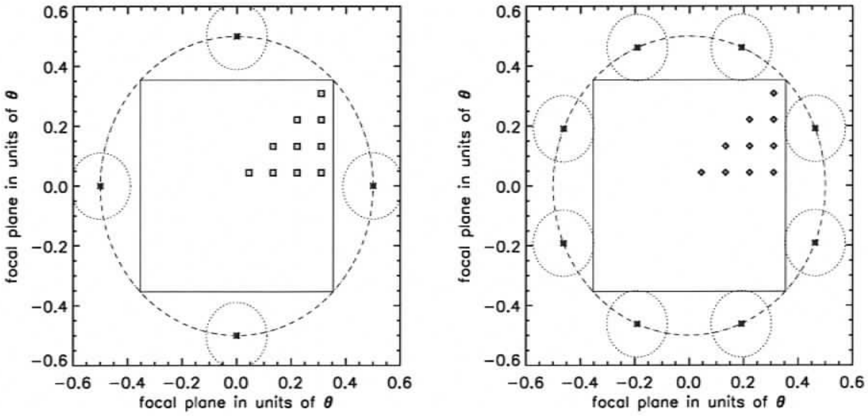

Figure 5.1 The arrangement of the beacons for the two LGS cases (asterisks). Using the symmetry of this arrangement the set of 10 unique PSF locations (square or diamond symbols) are shown inside the science detector area (large box).

5.3.2 Image quality metrics for GLAO

The performance of very wide GLAO (VWGLAO) is best described as seeing improved. As such, VWGLAO will not open new science cases, but can improve the efficiency of seeing limited science programs. For this reason we define two PSF metrics that make simple integration time calculations for image photometry, called Integration Time Ratio (ITR) and Integration Time Ratio for Spectroscopy (ITRS).

We start with the equation for background-limited signal to noise ratio (SNR) on a circular photometry aperture of diameter ω and solve for the integration time (IT). By background-limited we mean that noise from the detector and photon noise from the source are negligible compared to the photon noise of the sky or uniform background.

$$IT(\omega) = \frac{b\pi\omega^2}{4}\frac{SNR^2}{(pEE_{circ}(\omega))^2}, \tag{5.1}$$

where b is the background intensity. $EE_{circ}(\omega)$ is the fraction of PSF energy inside a concentric circle of diameter ω. The integrated PSF flux in units of photoelectrons per telescope aperture area is p. SNR is the desired photometry signal to noise ratio.

For the definition of ITR we will set $\omega = \bar{\omega}$, the optimal aperture size for background-limited point-source photometry. This is at the maximum signal to noise ratio as a function of ω and a fixed integration time. We define ITR to eliminate the constant of proportionality.

$$ITR = \frac{IT'(\bar{\omega}')}{IT(\bar{\omega})} = \left(\frac{\bar{\omega}'}{\bar{\omega}}\right)^2 \left(\frac{EE_{circ}(\bar{\omega})}{EE'_{circ}(\bar{\omega}')}\right)^2. \tag{5.2}$$

The prime denotes the no-GLAO PSF (seeing in this case) being compared. The two PSFs are of course in the same atmospheric conditions.

ITR has potential for becoming a standardized figure of merit for GLAO as its computation is no more complicated than Strehl ratio.

We also consider a wide field spectroscopy scenario in which the aperture is not optimized to suit the seeing conditions. We define ITRS here with a square aperture that is representative of the bin size used in reducing the dispersed images to 1D spectra. Generally the bin width in the spectral direction matches the width of the slit or spaxel in the focal plane. To maximize its usefulness as a diagnostic tool, ITRS will evaluate a source that is point-like in the spatial and spectral dimensions that is on a flat background in the dispersed image. This means that any continuum light from the source is fainter than the sky background. This is so that the total background in the dispersed image is proportional to ω^2.

$$IT(\omega) = b\omega^2 \frac{SNR^2}{(pEE_{sq}(\omega))^2}. \tag{5.3}$$

$EE_{sq}(\omega)$ is the fraction of the PSF energy ensquared in a width ω.

$$ITRS(\omega) = \frac{IT'(\omega)}{IT(\omega)} = \frac{((EE_{sq}(\omega))^2}{((EE'_{sq}(\omega))^2}. \tag{5.4}$$

The only difference from ITR is that the spaxel is square and the width ω is a parameter chosen for instrument design.

5.3.3 The atmospheric scenarios

The scenarios consist of a global outer scale, a global maximum wind profile, and optical turbulence profile (C_n^2) models. The optical turbulence profiles are separated

Table 5.1. The layer heights and models used from [TT06]. "B" indicates the model derived from balloon data. The "S" indicates the SODAR data. "FA" indicates the free atmosphere model.

	z_n (meters)											
scenario	7.8125	15.625	31.25	62.5	125	250	500	1000	2000	4000	8000	16000
B+S	B	B	B	S	S	S	S	FA	FA	FA	FA	FA
B	B	B	B	B	B	B	B	FA	FA	FA	FA	FA

into three scenarios, each with nine profiles statistically reduced from data measured at Cerro Pachon, the site of the Gemini South and the SOAR observatories in Chile. The first scenario is called "reference" here and consists of the good, bad, and typical ground layers ($\leq 3.6km$) described in the Gemini GLAO study by [ACS06]. The upper layers are from an Extreme AO study for Gemini. The second and third scenarios are taken from [TT06] and are called balloon and balloon+SODAR. In [TT06] the ground layers are given in terms of C_n^2 and to convert them to integrated turbulence we chose triangular weighting functions that maintain continuity with the upper layers, already integrated with triangular functions. The function for the n^{th} layer is unity at z_n and linearly goes to zero at $z_{n\pm1}$, except for the bottom layer, which is unity between $z = 0$ and z_1. Table 5.1 gives the chosen z_n and also gives the model used for each layer in the two scenarios derived from [TT06]. See Fig.5.2 for a plot of the balloon+SODAR models. The Fried parameter and isoplanatic patch size (r_o and θ_o) are plotted in the left panel of Fig.5.2 for all optical turbulence profiles. In this work we choose equal probability for all nine profiles in each scenario.

We are using a theoretical seeing limited PSF implicitly in ITR and ITRS and therefore want an accurate outer scale for the turbulence. An outer scale of $L_o = 30$ meters is often measured (e.g. [SVR04]) and is adopted here for all scenarios.

In §5.4.3 we solve for the WFS integration time that can be considered the maximum allowed for no detectable lag effects. This of course requires that we

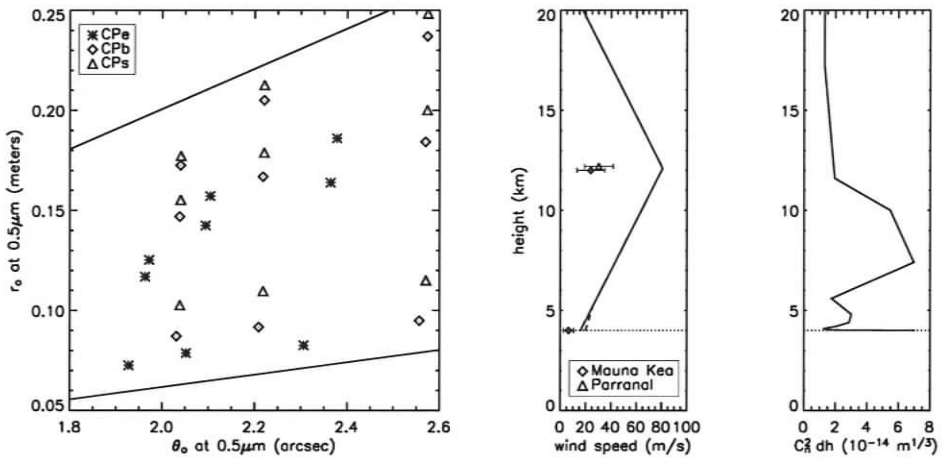

Figure 5.2 Left panel: the r_o and θ_o space occupied by the nine profiles in each scenario. The lines mark $0.314r_o/\theta_o = 6500$ and 2000 meters. Middle: the extreme wind model assumed for the calculation of Δt^+, the upper bound on WFS integration time. Right: A typical turbulence profile from the "reference" scenario shows that the wind in two layers near the tropopause carry just as much turbulence as the layers near the ground.

assume the worst possible wind scenario. At the ground we adopt the standard wind speed threshold for open dome work at most observatories ($16m/s$) and linearly interpolate up to the tropopause.

$$|v_n| = \begin{cases} 16(m/s) + 7\left(\frac{m/s}{km}\right) z_n & \text{if } z_n \leq 12.1km \\ 147(m/s) - 7\left(\frac{m/s}{km}\right) z_n & \text{if } z_n > 12.1km \end{cases} \tag{5.5}$$

where z_n is the height of the layer. The above max wind speed model is plotted in the center panel of Fig.5.2. The mean annual wind speed at the tropopause for two mid-latitude observatory sites [CAC05] is also plotted. The error bars roughly mark the RMS of the variation, indicating that the above wind speed model will very rarely underestimate the wind speed.

The position angle of the wind for all layers was chosen to be 225° counter clockwise from the positive x-axis in the focal plane.

5.3.4 Beacon type

As described in the original GLAO prescription by [Rig02], GLAO removes the contribution of high altitude phase to the DM through averaging the phase from multiple lines of sight around the field of view, introducing angular anisoplanatism. One can assist in removing the high altitude contribution by putting the beacons at an altitude H, which simulates laser guide stars (LGSs) and introduces cone or focal anisoplanatism. Compared to the cylindrical volumes measured using natural guide stars, the turbulent volumes inside cones measure less at high altitude while the ground layer volume remains roughly unchanged. This effect is useful in reducing the number of lines of sight (beacons) required to average out the high altitude turbulence. In the present work we show results at zenith for sodium laser guide stars ($H = 90km$) and for telescope diameters D =3.6 and 8 meters. The cone anisoplanatism this introduces is not enough to eliminate the contrast in angular anisoplanatism between 8 and 4 LGS, as we will see.

LGS wavefront sensors (WFSs) are blind to tip-tilt and focus (TTF). The model assumes perfect TTF correction in the field using a sufficient number of natural guide star WFSs (see [CEV06] for sky coverage analysis).

5.3.5 Conjugation range

We choose the DM be conjugated to the ground (from Chapter 4 $z' = 0$). The turbulent volume corrected by the deformable mirror (DM) can be more optimally conjugated slightly above ground. The term *gray zone* was coined by [Tok04] and it identifies the intermediate altitudes that are partially corrected by GLAO. The high altitude layers are not corrected at all. Recall from Chapter 4 that the height of the bottom of thegray zone is given by $z = \Delta/\theta$. The optimal range will not be more than the scale height of the ground layer turbulence, which, using gray zone arguments is less than 100 meters for the models of [TT06] and less than about 200 meters for the reference scenario. Including the conjugation parameter would also require we include the zenith angle parameter and for simplicity we exclude them by assuming $z' = 0$.

5.4 PSF modeling results for two hypothetical surveys

ITR is directly applicable as a measure of time savings in any program using photometry on unresolved objects on a uniform background that dominates the pixel noise. We choose the first survey science case to be detection and tracking of Near Earth Objects (NEOs) and Kuiper Belt Objects (KBOs) which is usually done at $\sim 0.6\mu m$. We use field mean ITR defined in §5.3.2 to optimize Δ. We speculate a telescope with $D = 3.6m$ has the appropriate trade off between light gathering power and seeing limited field of view, and choose $\theta_{max} = 26$ arcminutes. The results for this case are connected by the solid lines in the following figures.

The second example survey uses ITRS for unresolved line emission sources in a local group galaxy and $\lambda = 1.25\mu m$. The crowded stellar background provides a uniform continuum to satisfy the definition of ITRS. For this we speculate that the light gathering power of a $D = 8m$ telescope with $\theta_{max} = 13$ arcminutes is preferred. We use field mean ITRS defined in §5.3.2 and choose a spaxel to be $\omega = 0.2\,\mathrm{sec}$. This choice of ω is well matched to the median PSF FWHM at $1.25\mu m$ in these atmospheric scenarios. Another potential application of this ITRS metric is for a survey to search for new high redshift quasars emitting Lyman α light from as far as a redshift 10. The results for this case are connected by the dashed lines in the following figures.

Recall from Chapter 4 that the pitch is measured in the pupil plane of the telescope. We define the symbols pitch $= \Delta$ and optimal pitch $= \overline{\Delta}$. In §5.4.1 we will first find the $\overline{\Delta}$ of the VWGLAO system configuration for the two surveys, which we initially model without noise and lag errors. §5.4.2 identifies the field of view θ for VWGLAO. §5.4.3 then verifies that we are correct to assume no noise and no lag in the VWGLAO regime.

5.4.1 The optimal pitch for GLAO $\overline{\Delta}$

Recall from Chapter 4 that the number of pitches across the pupil is $N_p \equiv D/\Delta$, where N_p is an integer. With a well sampled vertical turbulence profile each image quality metric as a function of N_p generally has one extremum. In the case of four LGS the extremum is easy to find as image quality degrades noticeably as N_p increases past the extremum. In the case of eight LGS, the extremum is in a region where the slope is very shallow. This is thanks to the larger number of guide stars doing better at averaging out the high altitude turbulence thereby introducing less anisoplanatism at large N_p.

In this section we find the extremum of $ITR(N_p)$ and $ITRS(N_p)$. It would be interesting to do a trade study, putting a dollar amount to initial investment in N_p and to the savings implied by ITR and ITRS over the lifetime of the instrument. For simplicity we choose the optimal N_p to be simply where ITR or ITRS is 1.05 times its extreme value.

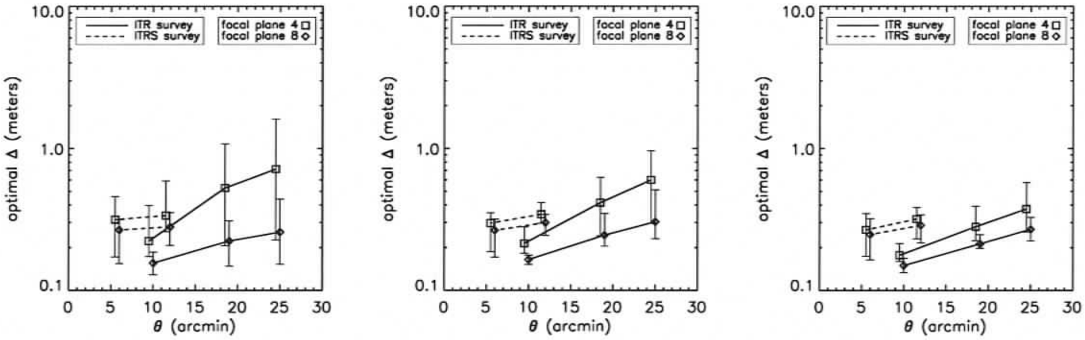

Figure 5.3 The optimal pitch projected in the pupil ($\overline{\Delta}$) as a function of the GLAO field of view (θ). In the panels, from left to right, are the reference model, the balloon only model, and the balloon+SODAR model. On each panel are the four combinations of [4,8] LGSs and [ITR,ITRS] survey science. For each combination there are a few different θ shown. For each case there is a set of nine profiles which give nine $\overline{\Delta}$ values. The symbols mark the 50^{th} percentile $\overline{\Delta}$. The bars mark 20^{th} and 80^{th} percentile.

The results are separated by atmospheric scenario into three panels shown in Fig.5.3 and described in the caption. The search for $\overline{\Delta}$ can be thought of as bringing the bottom of the gray zone as low as possible without degrading image quality. For example, the balloon+SODAR scenario (right panel Fig.5.3) with $\theta = 25$ arcminutes rarely needs the bottom of the *gray zone* to go above 70 meters. The smallest optimal pitch is found for profiles that have ground layer turbulence close the ground conjugated DM. In the region around θ =10 to 12 arcminutes the ITR and ITRS science cases overlap. The optimal pitch for the ITR science ($0.6\mu m$) is smaller than that needed the ITRS science ($1.25\mu m$). This is largely due to the difference in the wavelength of the light, but is also connected to the differences between ITR and ITRS.

Another interesting point is the benefit of a system that corrects only tip-tilt and focus. The ITR science case was chosen to be on a $D = 3.6$ meter telescope. When the $\overline{\Delta} = 1.8$ meters the correction can be approximately described as simply tip-tilt and focus correction. In the reference atmospheric scenario (left panel) this is in fact the optimal pitch 20% of the time when $\theta = 25$ arcminutes.

5.4.2 The corrected field of view for VWGLAO

VWGLAO will improve the efficiency of seeing limited survey science programs that use a contiguous wide field of view. By survey programs we mean that *the efficiency is proportional to the solid angle subtended by the science field times the integration time IT*. In other words, on a telescope with seeing limited field of view θ_{max} that can accommodate GLAO with field of view $\theta < \theta_{max}$, had better improve ITR or ITRS of a single pointing by more than $(\theta_{max}/\theta)^2$.

Fig.5.4 shows the field mean ITR for the imaging survey ($\theta_{max} = 26$ arcmin) using optimal pitch for each profile. The shaded area is where ITR is less than $(\theta_{max}/\theta)^2$ and therefore does not improve the survey efficiency. This survey on a telescope with a 26 arcmin seeing limited field of view in these modeled Cerro Pachon profiles is a definite challenge to GLAO. In the reference scenario (left panel Fig.5.4) GLAO gains are not guaranteed, even at $(\theta/\theta_{max})^2 = 0.95$. With the balloon+SODAR models there is guaranteed gain if the true efficiency is not much less than ITR.

It is likely that GLAO can be activated on-the-fly, but the overhead in setting up the observations will be slightly longer than for seeing limited and that difference in time will slightly reduce the true efficiency. There will also be some obstacles to GLAO observations, such as LGS downtime that will further reduce the true efficiency. On the other hand, there will be no loss in throughput (or increase in emissivity) if GLAO is implemented with an adaptive secondary mirror.

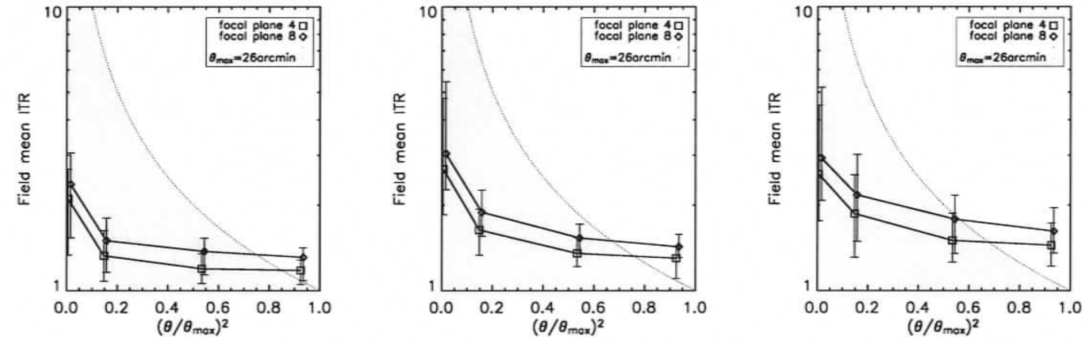

Figure 5.4 The ITR survey science case with ITR as a function of relative field area. This survey is on a telescope with a θ_{max} =26 arcminute seeing limited field of view.

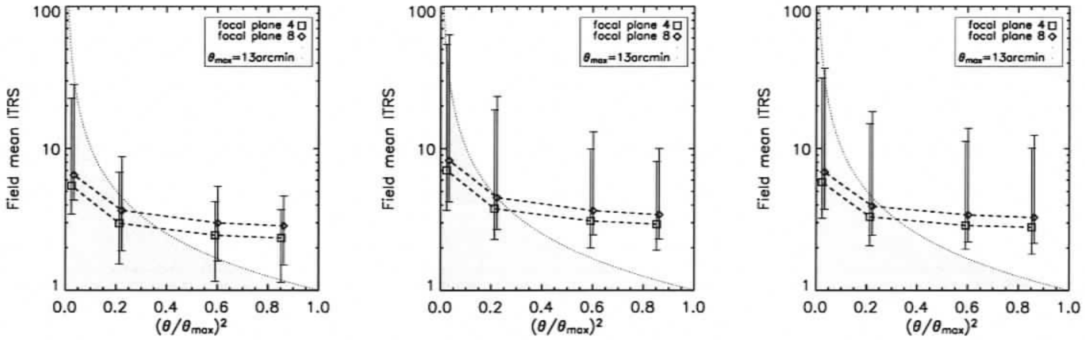

Figure 5.5 The ITRS survey science case with ITRS as a function of relative field area. This survey is on a telescope with a θ_{max} =13 arcminute seeing limited field of view.

Fig.5.5 is ITRS for the spectroscopy survey. Here we see a huge gain for monochromatic point sources that is almost constant for $(\theta/\theta_{max})^2 = 0.2$ to 1.0. This corresponds to $\theta = 6$ to 13 arcmin which roughly corresponds to the bottom of the gray zone at $2\overline{\Delta}/\theta = 180$ to 80 meters (cf. Fig. 6 in [TT06]). Point-like sources are common, which more easily allows ITR to be generally interpreted as a real efficiency prediction. However, point-like monochromatic sources are less common and generalizing ITRS as an efficiency is not as useful.

What is most important to recognize here is that the conversion of ITR and ITRS into true efficiency predictions will not be a function of θ. Therefore, GLAO used to assist survey science should strive for $\theta/\theta_{max} \rightarrow 1.0$, the VWGLAO regime. VWGLAO will provide useful gains so long as the θ_{max} is not so large that $\overline{\Delta}$ becomes too large to provide noticeable correction. We saw this happening for the ITR case ($D = 3.6m$ and $theta_{max} = 26$ arcmin) where the optimal pitch was often many times larger than the total r_o, especially for the reference scenario. This means that that telescope on that site (with the reference atmospheric scenario) should not use GLAO to assist the ITR survey. The ITRS case ($theta_{max} = 13$ arcmin) on the other hand shows very useful VWGLAO potential and should use GLAO.

5.4.3 The integration time requirement Δt^+

To verify that modeling without noise is valid in the VWGLAO regime we check for the effect of lag. We solve for Δt^+, the WFS integration time that gives no more than 1% degradation of the image quality metric anywhere in the field (we set $\tau = \Delta t/2$ in Eqn.(4.7)). We use the maximum wind speed profile described in §5.3.3 which makes Δt^+ is the smallest, most pessimistic upper bound on allowed integration times. If the WFS system can collect enough photons in Δt^+ and subapertures of area $\overline{\Delta}^2$ to get performance that is not deteriorated by noise, then the system will never be limited by noise or lag.

Fig.5.6 shows only those θ that are in the useful VWGLAO regime. We see that Δt^+ is rarely less than 2 milliseconds for the ITRS case. In a wind profile that is

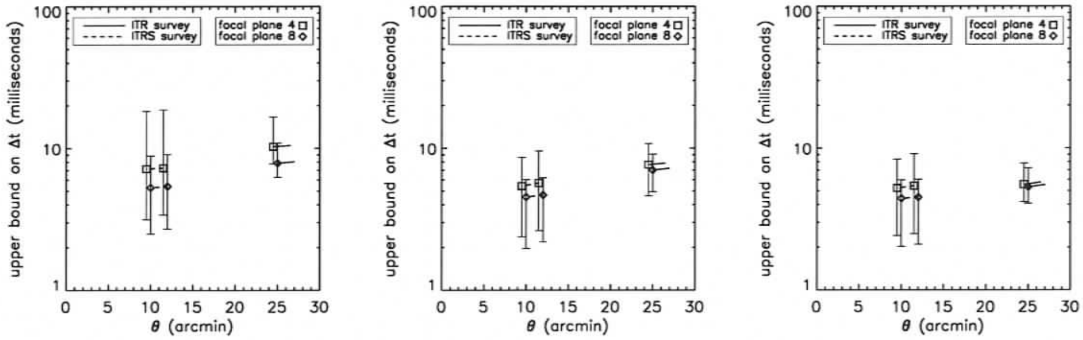

Figure 5.6 Similar to Fig.5.3, the upper bound on WFS integration time (Δt^{+}) as a function of the field of view θ. In the panels, from left to right, are the reference model, the balloon only model, and the balloon plus SODAR model.

half as fast, Δt^{+} would be about 4 milliseconds. At the time this was written, single LGS systems were being used to operate medium to high Strehl systems with 1 to 2 milliseconds WFS integration time and pitch of around 0.5 meters. We are finding VWGLAO pitches that are smaller, 0.2 and 0.25 meters for 8 and 4 LGS. This causes a decreased wavefront signal to noise measurement per WFS proportional to 0.2/0.5=0.4 and 0.25/0.5=0.5 [Rod99]. We break even with the benefit from 4 or 8 WFSs that provide $\sqrt{8} = 2.8$ and $\sqrt{4} = 2$ times more signal to noise. When we also remember that 2 milliseconds corresponds to the worst case scenario and in the vast majority of cases there will be more time to integrate, we do better than break even. Therefore, the VWGLAO cases explored here will have less WFS noise than exisiting LGS systems. We can conclude that there is plenty of room to balance WFS noise and lag where both contribute wavefront error negligible compared to angular anisoplanatism.

One more concern for GLAO WFS noise is residual spot jitter as a result of the anisoplanatism allowed on the residual GLAO wavefront. In other words the WFS spots will not benefit from the correction of local tip-tilt in closed loop like with AO systems in use today. It has been checked that the slight loss in sensitivity is on the order of 20 to 30 *nm* RMS and therefore negligible compared to angular anisoplanatism.

5.5 Conclusions

- At mid-latitudes, nature provides reduced turbulence at intermediate altitudes and as a result of this region the mean image quality of a GLAO corrected field with diameter $= \theta$ degrades slowly with increasing θ. Recall that with increasing θ the optimal pitch increases to keep the bottom of the gray zone at the bottom of this region. This means that there are useful VWGLAO gains to be had so long as the seeing limited field of view of the telescope (θ_{max}) is not so large that the optimal pitch becomes too large, providing no noticeable correction.

- The VWGLAO regime can be realized with negligible wavefront error caused by servo lag and wavefront sensor noise, requiring no more LGS WFS photons than existing systems. For the atmospheric scenarios studied here we find this to be the case even for optimized pitch.

It is interesting to note that while the jet-stream generates turbulence at high altitude for sites at mid-latitudes, the extreme latitudes, namely the arctic and antarctic may offer enormous GLAO gains from their lack of high altitude turbulence, at any corrected field of view. These enormous gains would therefore exclude them from the VWGLAO regime and require more detailed modeling.

Chapter 6

Evaluation of GLAO for WFOS on TMT

This chapter is work in press for the proceedings of the International Society for Optical Engineering conference on Astronomical Telescopes and Instrumentation May 24-31, 2006. The author list in order, is Jeff Stoesz, Jean-Pierre Véran, Scott Roberts, Brent Ellerbroek and Matthew Britton. JPV completed the analysis in §6.5 with modeling assistance from JS. SR lead the trade study and assessed the dollar amounts in §6.4. BE and MB performed checks on JS's model using their own iterative codes *LAOS* and *Arroyo* . BE and MB were also consulted for suitable TMT modeling parameters. JS would also like to acknowledge Matthias Schoeck for providing the T1 and T2 C_n^2 databases with clear explanation.

Abstract:

We arrive at a Ground Layer Adaptive Optics (GLAO) design for the Wide Field Optical Spectrograph (WFOS) on the Thirty Meter Telescope (TMT) that offers true seeing-improved performance and operation for the red and infrared wavelengths. The design requires an adaptive secondary (AM2) and the sodium Laser Guide Star (LGS) launch telescope be able to steer four of the beams to 8.5 arcminutes off-axis. When provided with this the proposed design is potentially the simplest, lowest cost design and can take the form of an upgrade to a seeing limited WFOS. This is seen as a significant advantage over designs that would build an adaptive mirror into each of the four arms of WFOS. We show that the performance penalty for using one mirror instead of four to correct the entire 81 square arcminute WFOS field is minor.

6.1 Introduction

The Thirty Meter Telescope (TMT) project identified a Wide Field Optical Spectrograph (WFOS) as a candidate first generation instrument. To further understand the costs and challenges of such an instrument a ten month feasibility study was undertaken for the project by Association of Canadian Universities for Research in Astronomy (ACURA), and the National Research Council Herzberg Institute of Astrophysics (NRC-HIA). Our design is built upon previous WFOS design studies done in the context of the Canadian Very Large Optical Telescope (VLOT) project at NRC-HIA between November 2003 and November 2004. The overall instrument design and science motivation is described in [PRA06] and references therein.

Curiosity about image improvement over large fields by correcting turbulence near the ground is not new [Rig02] and still mostly unsatisfied due to a lack of data on the vertical distribution of the turbulence, especially in the bottom 1000 meters [Tok04, LH06]. Our current understanding of the vertical distribution of turbulence at most sites does allow us to confidently say that a uniform correction of the > 75 square arcminute field specified by the science cases for WFOS by a single conjugate adaptive optics system will be a modest improvement over a system that achieves the seeing limit. The gains for any of the designs we consider are best described as seeing improved and characterized by integration time savings. In this chapter we evaluate the feasibility of several designs and arrive at a baseline that has a Ground Layer Adaptive Optics system correct the WFOS science field before entering the spectrograph optics. This strengthens the call by other TMT adaptive optics systems for the telescopes's Gregorian secondary to double as a continuous face sheet deformable mirror (called AM2). See [PRA06] for an overview of WFOS and [PFM06] for details on the spectrograph optical design.

In §6.2 we present the model and its input. In §6.3 we use averaged image quality metrics to predict upper limits on the efficiency of the baseline design in various observing conditions. §6.3 also includes predicted PSF uniformity. In §6.4

we explore several possible architectures, affirming our chosen baseline design. §6.5 provides some detail on the main sub-systems for the baseline GLAO design and gives their top level requirements. Finally, §6.6 summarizes the important points from §6.3, §6.4, and §6.5.

6.2 The model

In the following subsections we first describe the atmospheric input to the PSF model, the model itself and other input parameters, then the image quality metrics used throughout this chapter are briefly defined.

6.2.1 The atmospheric database

Accurate predictions for GLAO with the 81 square arcminute field of WFOS and AM2 conjugation require vertical resolution of better than 100 meters in the turbulence profile ($C_n^2(h)$) at the ground, not to mention peculiar non-von Karman effects (e.g. from the telescope enclosure). In the meantime there is extensive, high quality MASS-DIMM data available at two candidate TMT sites (designated T1 and T2) plus high vertical resolution balloon data for Cerro Pachon.

The T1 and T2 profiles are defined with the ground layer at zero meters and the next highest layer at 500 meters. To account for the unknown scale height of the ground layer we also define a modified set of T1 and T2 profiles with the ground layer at 300 meters and are denoted $T1_{300m}$ and $T2_{300m}$. We model the AM2 cases with the DM conjugated to zero meters, which would make predictions based on the unmodified T1 and T2 profiles optimistic and the modified ones very pessimistic. These two sets will bracket the true predictions for an AM2 conjugated at a range of 300 meters.

The Cerro Pachon (CP) balloon data were reduced to a nine profile model with the associated probabilities shown in Table 6.1. This CP model has been extensively used in other GLAO studies. For the readers who are familiar with them, the version

Table 6.1. The probabilities for the nine Cerro Pachon profiles.

	free atmosphere layers		
ground layers	good	typical	bad
good	0.0625	0.125	0.0625
typical	0.125	0.25	0.125
bad	0.0625	0.125	0.0625

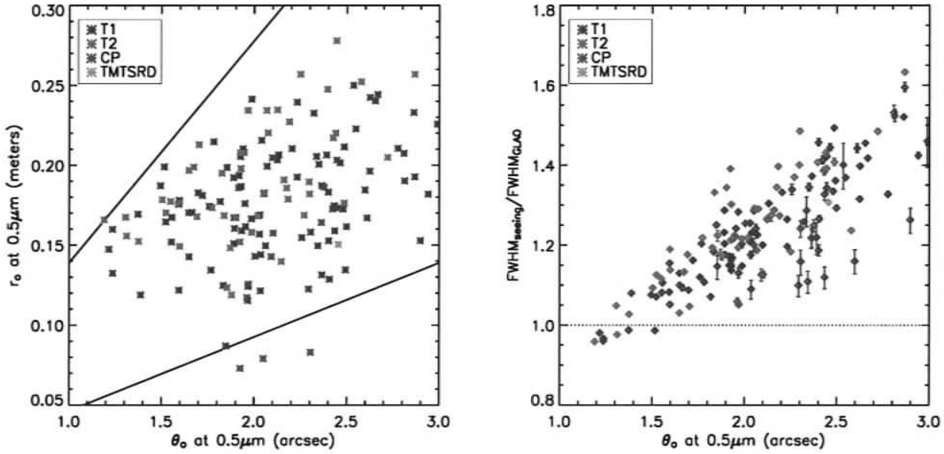

Figure 6.1 The left panel shows the r_o and θ_o (at 0.5μm) for each profile. The two straight lines mark constant $\bar{h}$ =3km, 9km (lower, upper line; $\bar{h} = 0.314 r_o/\theta_o$). The right panel shows the FWHM gain (at 0.6μm) of the baseline GLAO system versus θ_o (at 0.5μm). The diamonds correspond to the mean in the field of view for the AM2-5 baseline design. The vertical bars mark the minimum and maximum values in each field.

of the profiles used here are the extended upper atmosphere version (i.e. four layers above 5 km).

The solitary profile used in the TMT Science Requirements Document is plotted in Fig.6.1 for reference. The Fried parameter (r_o) and isoplanatic patch (θ_o) are moments of the C_n^2 profiles and admittedly do not capture all of the atmospheric character relevant to GLAO. Apropos, the $T1_{300m}$ and $T2_{300m}$ profiles are indistinguishable from the T1 and T2 profiles in the left panel of Fig.6.1 The nine CP profiles (red asterisks) include three of the strongest seeing cases (smallest r_o) which correspond to the profiles with strong turbulence in the ground layers, also known as bad ground layer profiles.

It has been observed that the distribution of outer scale of turbulence at Mauna Kea is log-normal with a mean ~ 30 meters and FWHM ~ 15 meters. It was found that this distribution of outer scale does not noticeably bias the results in §6.4. Hence all three atmospheric scenarios [T1,T2,CP] are simulated with a fixed outer scale $L_o = 30$ meters.

6.2.2 The GLAO PSF model

The formalism used to simulate the Ground Layer AO (GLAO) Point Spread Function (PSF) for the analysis in the following sections is that of *PAOLA* , using a 2D FFT based algorithm by [JVC06]. The PSF model is coded in IDL and defined in the spatial frequency domain as a sum of phase Power Spectra Densities (PSDs). There are two fundamental and uncorrelated error sources in the PSD that are considered in this study.

$$W(f) = W_{aniso}(\text{field location, wind speed}, f) + W_{fit}(f) \tag{6.1}$$

Where f is the spatial frequency of the wavefront projected onto the primary mirror (called the pupil plane hereafter). For simplicity we choose a square actuator geometry with pitch Δ in the pupil plane so that the fitting error term (W_{fit}) for f_x or $f_y > (2\Delta)^{-1}$ is a von Karman spectrum (with L_o specified in §6.2.1) and zero elsewhere. Similarly, the anisoplanatism term is non-zero only where f_x or$f_y \leq (2\Delta)^{-1}$.

Angular anisoplanatism is of course a strong function of the field location of the PSF and is therefore important to LGS asterism trades. As shown in Chapter 5 angular anisoplanatism and fitting error are dominant over lag anisoplanatism and WFS noise for the subaperture pitch of 0.59-1 meter considered in the asterism trades and we are therefore free to model with only angular anisoplanatism and fitting error.

We use lag anisoplanatism to set the requirement on the adaptive secondary mirror (AM2) and ultimately balances with the noise term through wavefront sensor (WFS) integration time, which is in turn dictated by the wind speed assuming frozen flow. This is covered in §6.5.1.

LGS WFSs are blind to tip-tilt, but the model does not include tip-tilt anisoplanatism. We therefore assume perfect tip-tilt correction in each field using NGS WFSs. This implies a requirement on the patrol field of each NGS WFS needed to measure TTF, which is explained in §6.5.3.

The parameters used in the following sections are:

- DM height: at the ground
- sub-aperture pitch (subap spacing Δ): 1 to 0.59 meters (30x30, 50x50)
- DM actuator pitch: matched to sub-apertures
- LGS asterism: various asterisms are used in §6.4 and are described in Table 6.3
- PSF locations: 10 locations for AM2-5 that take advantage of focal plane symmetry for field statistics (see Fig.6.2). The spacing of sampled PSF locations is 1.125 arcminutes which well samples PSF variation for every case except Arm-1 (defined in §6.4) also known as Single-Layer GLAO (SLGLAO).
- Outer scale (L_o): 30 meters
- Zenith distance: zero only
- Image wavelength: 0.6 and 0.8μm in §6.4 and [0.4, 0.6, 1.25] μm in §6.3.1 and §6.3.2

6.2.3 Image quality metrics

Each modeled PSF is subsequently reduced to five image quality metrics to evaluate GLAO with WFOS: full width at half maximum (FWHM), width of 50% ensquared

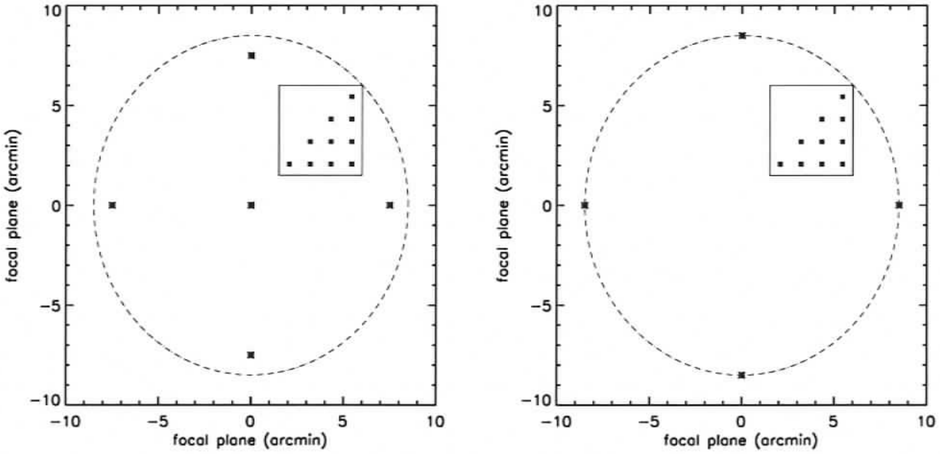

Figure 6.2 The field of view arrangement for the baseline AM2-5 configuration (left panel) and the compatible AM2-4-8.5 configuration (right panel). The asterisks are the LGS locations and the square points are the locations of the simulated PSFs for the field statistics presented in subsequent sections. It was determined that the AM2-5 design is incompatible with the opto-mechanical layout of the atmospheric dispersion compensators (ADCs) and the new baseline uses the LGS arrangement in the right panel.

energy (EE50), relative integration time (RIT) as well as integration time ratios with optimal apertures for imaging (ITR) and fixed apertures for spectroscopy (ITRS). Refer to Chapter 5 for the derivation and discussion of RIT, ITR and ITRS.

6.3 Performance predictions for the baseline design

6.3.1 Upper limits on efficiency

In this subsection we use ITR and ITRS averaged over the field and atmospheric scenario to assess the upper limit on efficiency of GLAO for WFOS. In addition to ITR for imaging, we have chosen ITRS with for small slit applications in crowded fields ($\omega = 0.25\,\mathrm{sec}$) and the more common large slit ($\omega = 0.7\,\mathrm{sec}$). The most important consideration for a global efficiency estimate is cirrus cloud, which can cause shutdown of the LGS system that is propagated from the top of the secondary mirror structure. We consider the LGS and GLAO setup time to be small compared to the science integration times or cirrus cloud down-time.

One reason for this is that our wide field baseline design the improvement in the PSF is not drastic and hence the slit mask designed for GLAO will work with seeing limited images as well. Also, any brief periods of loop instability during loop closure or loop breakage are also not going to significantly impact the large PSF. The effect of breaking the loop is expected to be an instant switch from GLAO performance to seeing limited values. Likewise, when the loop is closed it will be an instant improvement. This leads to an operational concept of GLAO-WFOS that will allow observations to start even before the loop closes, which means the baseline design would introduce zero additional overhead.

Therefore, to correct the ITR and ITRS values for both setup time and the appearance of fratricide caused by cirrus, we take a randomly selected fraction of the ITR and ITRS values to be unity (the seeing limited value). By randomly selecting the observations from each scenario we have assumed cirrus is uncorrelated to the turbulence profile. We take the selected fraction to be 20% based on preliminary results of a TMT study on Mauna Kea sky transparency [Ste06]. We expect that with fairly deep exposures the setup time to be some small fraction of that.

If cirrus downtime accounts for the balance of time being taxed from GLAO then resulting averages of ITR and ITRS can be called efficiency ratios, the efficiency with GLAO over the seeing limited case. Fig.6.3 shows the resulting upper limit on efficiency ratio at the candidate TMT sites (T1, T2) as the solid line. The dash dot line is for the Cerro Pachon scenario. The ITR and ITRS results from the modified $T1_{300m}$, $T2_{300m}$ profiles were used to draw the dashed line segments at$0.6\mu m$ They indicate where the lower limit is for these sites if the science objects are ideal kinds of objects that ITR and ITRS are defined with. As explained in Chapter 5, ITR and ITRS are metrics defined on a source that is unresolved (point like) in the spatial dimensions (i.e. PSF) and on a flat background. The ITRS metric has the added classification of being point like in the spectral dimension. This means an unresolved emission line on a faint continuum from the source plus a bright background that are locally flat in the spectral dimension. While the definition of ITR for imaging is quite common, the definition for ITRS is rarely satisfied in real spectroscopy observations where emission (or absorption) features must be resolved. As such, these predictions are designed give the upper limit on efficiency.

By inspecting Fig.6.3 it seems likely that GLAO can provide an efficiency ratio of 1.1 in at visible wavelengths and as much as 1.4 toward J band, with aproprate choice of aperture. The $0.7''$ aperture is naturally provides less efficiency gain for the red and infrared wavelengths where the images are smaller.

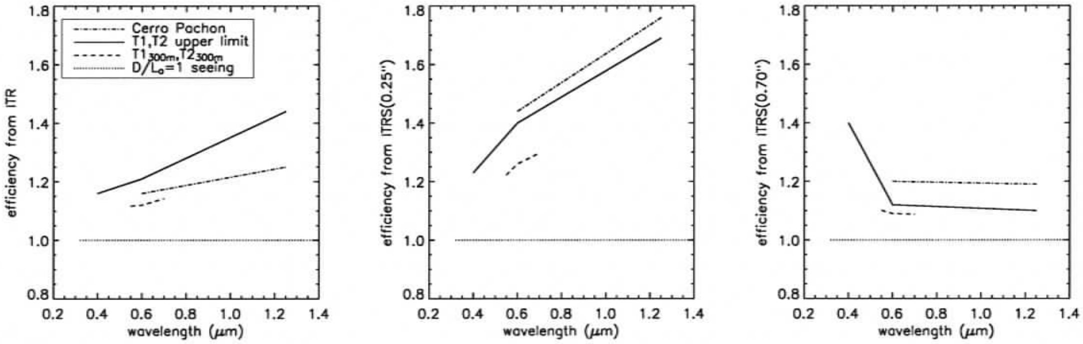

Figure 6.3 The ratio of efficiency with GLAO over the seeing limited case, for imaging (left panel) and spectroscopy using a $0.25''$ aperture (middle) or a $0.7''$ aperture (right). The solid lines are upper limits for the T1 and T2 scenarios. The dashed segment indicates where the lower limit would be for these sites if the science objects were point like objects (see text).

6.3.2 GLAO PSF uniformity

Recall that Tokovinin defines the bottom of the gray zone to be at a hight equal to the pitch divided by the diameter of the GLAO guide star asterism $z = \Delta/\theta$ [Tok04]. Image uniformity results are strongly dependent on details of vertical resolution of the turbulence near the boundary of the gray zone and hence the altitude of conjugation. The T1, $T1_{300m}$, T2, $T2_{300m}$ results should bracket the true uniformity redictions. The results on the CP scenario and ground conjugation may represent more realistic uniformity predictions for the 300 meter conjugation of the TMT AM2.

Table 6.2. The summary of WFOS-GLAO PSF variation in terms of the relative standard deviation of FWHM or EE50 over the field. The results for the T1 and T2 profiles with the ground layer adjusted to 300 meters away are shown in parentheses.

$0.4\mu m$		$0.6\mu m$		$1.25\mu m$	
FWHM	EE50	FWHM	EE50	FWHM	EE50
50^{th} percentile					
$0.1\%_{T2}$	$0.1\%_{T2}$	$0.2\%(1.2\%)_{T2}$	$0.1\%(0.7\%)_{T2}$	$0.4\%_{T2}$	$0.1\%_{T2}$
$0.2\%_{T1}$	$0.1\%_{T1}$	$0.2\%(1.2\%)_{T1}$	$0.1\%(0.7\%)_{T1}$	$0.7\%_{T1}$	$0.2\%_{T1}$
		$0.7\%_{CP}$	$0.4\%_{CP}$	$1.5\%_{CP}$	$0.7\%_{CP}$
95^{th} percentile					
$0.4\%_{T2}$	$0.2\%_{T2}$	$0.5\%(2.2\%)_{T2}$	$0.3\%(1.1\%)_{T2}$	$1.4\%_{T2}$	$0.5\%_{T2}$
$1.0\%_{T1}$	$0.6\%_{T1}$	$1.1\%_{CP}$	$0.5\%_{CP}$	$3.0\%_{CP}$	$1.0\%_{CP}$
		$1.4\%(2.3\%)_{T1}$	$0.7\%(1.1\%)_{T1}$	$4.1\%_{T1}$	$1.4\%_{T1}$

The baseline GLAO system introduces a very small amount of non-uniformity, not more than telescope and instrument aberrations tolerated in the optical design. The WFOS fields are located far enough away from the guide stars in the baseline design(s) there is a relatively smooth and constant gradient inside each field, which causes a rather flat distribution of any image quality metric. This is apparent in the example contour plots of FWHM in Fig. 6.4. It also implies that in each field the difference between the mean and the extreme values will generally be about two times one standard deviation. Table 6.2 contains the field standard deviation relative to the field mean for FWHM and EE50. The values in parentheses under $0.6\mu m$ are for the $T1_{300m}$ and $T2_{300m}$ scenarios. The 95^{th} percentile values in the bottom half of the table represent the worst possible uniformity for each atmospheric scenario. Therefore, at $0.6\mu m$ the worst relative variation is almost never more than a few percent and usually less than 2%. As the GLAO correction becomes poorer toward bluer wavelengths the uniformity becomes better.

The images are also very circular. The difference between the major and minor axis of an ellipse fit to FWHM is never more than 1%.

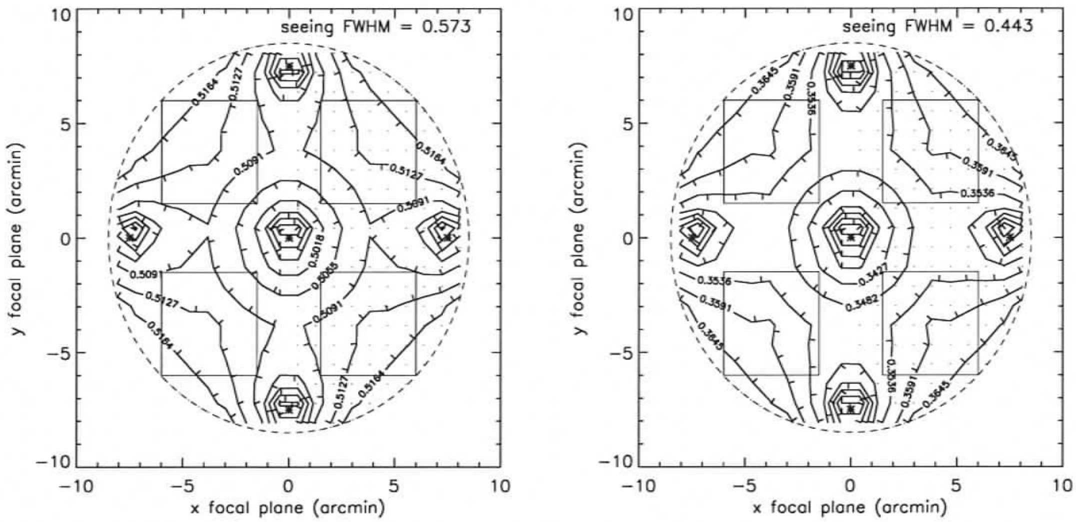

Figure 6.4 Example contour plots of PSF FWHM in the focal plane at $0.5\mu m$ (left panel) and $1.1\mu m$ (right panel). This is the AM2-5 baseline configuration with the typical:typical Cerro Pachon profile. The AM2-4-8.5 with out the central LGS will have more uniform image quality.

Table 6.3. Summary of GLAO architectures considered in the study.

Name	DM location(s)	LGS asterism for each DM
AM2-4	Adaptive Secondary Mirror	4 LGSs, one centered on each science field
AM2-4-8.5	Adaptive Secondary Mirror	4 LGSs outside of the WFOS science fields
AM2-5	Adaptive Secondary Mirror	5 LGSs outside of the WFOS science fields
AM2-8	Adaptive Secondary Mirror	8 LGSs bordering on the WFOS science fields
Arm-1	Modified WFOS Collimator	1 LGS centered on each science field (4 total)
Arm-2	Modified WFOS Collimator	2 LGSs bordering on each science field (8 total)
AM2-...*	Adaptive Secondary Mirror	...LGSs outside of the WFOS science fields
Arm-4*	Modified WFOS Collimator	4 LGSs bordering on each science field (12 total)

*These architectures have more than the expected number of LGSs to be provided by the LGS facility and are included for illustrative purposes.

6.4 Architecture trades

Summarized in Table 6.3 are eight GLAO architectures that cover the range of considered LGS constellations and deformable mirror (DM) implementations. The focal plane detail for AM2-5 and AM2-4 are shown in Fig.6.2.

The first three options in Table 6.3 have the telescope secondary mirror (AM2) as the DM, common to the paths of all four WFOS subfields. The Arm configurations (Arm-1, Arm-2, and Arm-4) use a DM in the WFOS collimator in each of the four barrels. The current WFOS design does not provide an intermediate pupil location for a DM within the collimator. In order to provide this location we expect that four additional reflections would be required (including the DM). With an average surface reflectivity of 0.97, this is a $\sim$ 10% loss of throughput. A rough order of magnitude estimate for implementing this collimator / DM combination is \$2.5 M per arm.

The upper bound on the number of LGSs for WFOS-GLAO will be the number planned for other TMT AO systems. Therefore, based on current planning for NFIRAOS, we expect to have seven to nine LGSs available. A requirement from WFOS-GLAO would be that the LGSs be able to move out to edges of the WFOS field (17 arcminutes diameter).

For the Arm-1 and AM2-4 options an LGS is projected within each WFOS science field. LGSs within the science field could be picked off with mirrors close to the focal plane or by placing dichroic beamsplitter windows in front of the field. The beamsplitter option is a technical challenge because of the size of the substrate required, and the difficulty in applying a multi-layer coating that will provide a notch filter for 589 nm light. Also, with this option there would be a loss of throughput of science light across the full wavelength range.

6.4.1 Simulation results

In this section we will show how the PSF is affected by the AM2 vs. Arm architectures, LGS asterism, and actuator density.

Arm vs. AM2

The AM2-4-8.5 is the chosen baseline design and offers performance very similar to AM2-5. Here we compare AM2-4-8.5 to Arm-4 with the $T1_{300m}$ and $T2_{300m}$

scenarios, which ensures that we will not underestimate the performance of potential of the Arm architectures. The $T1_{300m}$ and $T2_{300m}$ are the worst scenarios for the AM2 case, with the nearest layer to the DM at 300 meters away and the next nearest at 500 meters away, the greatest amount of turbulence is in the GLAO gray zone [Tok04]. The left panel of Fig.6.5 shows the asterism for both AM2-4-8.5 and Arm-4. To achieve the latter requires at least 12 LGS and vignetting of the science field.

The cumulative histogram results for ITR (right panel Fig.6.5) show that changing from the baseline design to the powerful Arm-4 design would change the median ITR at $0.6\mu m$ from 1.18 to 1.3 half the time. Both cases here are simulated with a pitch of 1 meter. The Arm-4 case with 0.59 meter pitch (50x50 on each DM) achieves a slight better 1.32 half the time.

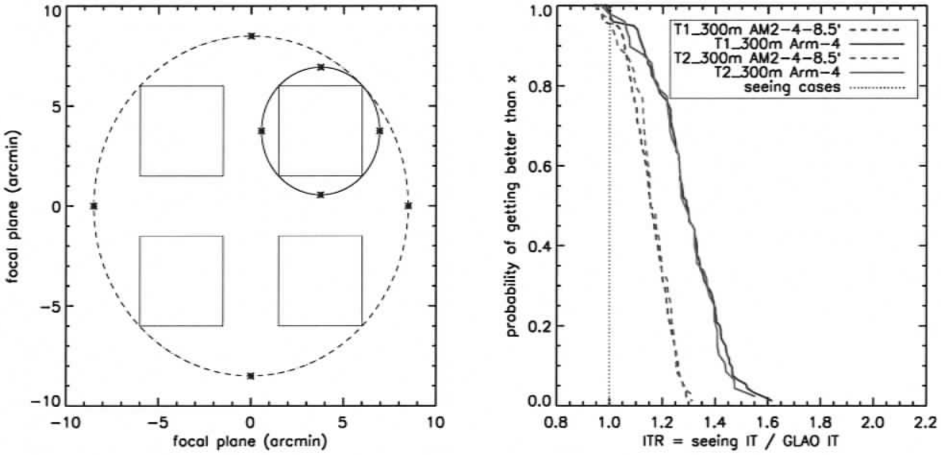

Figure 6.5 Comparison of Arm-4 and AM2-4-8.5. Left panel: is the WFOS focal plane with the guide stars of the Arm-4 case connected by the circle drawn with a solid line of diameter 6.38 arcminutes. The baseline AM2-4-8.5 guide stars are connected by the dashed line, 17 arcminutes in diameter. Right panel: performance show with solid and dashed lines in a of cumulative histogram of ITR.

AM2 variations

We continue the trade study with the Cerro Pachon atmospheric scenario because it offers proper vertical resolution of C_n^2 at 0,20,50, and 100 meters. The left panel of Fig.6.6 shows cumulative histograms of relative integration time (RIT) at 0.8 microns. It shows RIT improving slightly as one goes from a 30x30 to a 50x50 AM2 system (pitch from 1 to 0.59 meters). The biggest improvement occurs where the GLAO DM has the greatest potential, strong turbulence in the lower layers of these CP profiles.

The right panel of Fig.6.6 shows that, with a 50x50 system, any number of guide stars greater than or equal to four gives roughly the same performance. Hence four or five LGS are sufficient to command a 50x50 system and therefore a 30x30. As in the left panel, the order of the list of cases in the legend from left to right matches the order of solid curves. Arm-1 and AM2-4 are not included in these plots as the field mean is similar to the others yet the standard deviation is too large to appear in Fig.6.7.

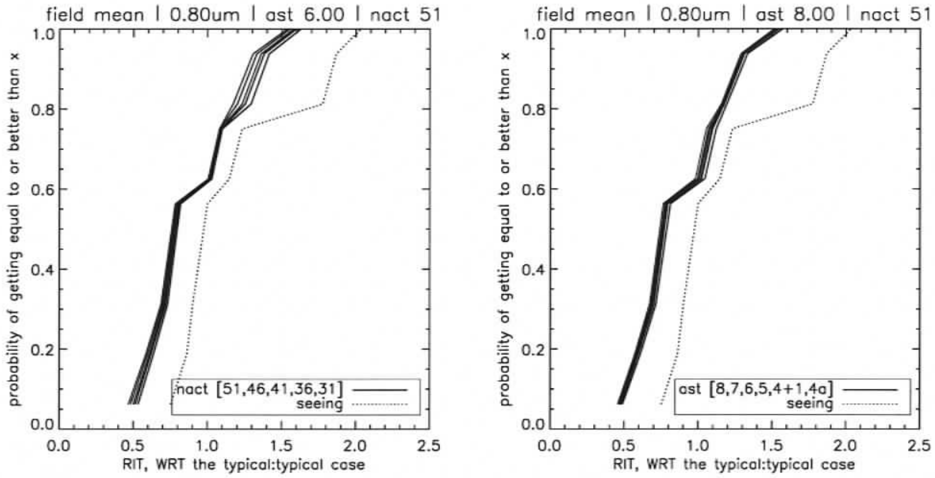

Figure 6.6 The left panel is for a hexagon-like asterism at various actuator densities indicated in the legend by the number of actuators across the diameter of the pupil. The right panel are the results with 50x50 actuators and various ring asterisms indicated in the legend by the number of LGS in the ring, with or without an extra added in center ("+1").

Table 6.4. Summary of architecture cost and 50th percentile performance at zenith and 0.8μm.

Architecture	ITR, field mean/median	ITR, field std.dev.	First light or upgrade	Vignetted fraction of 4.5'x4.5' field	Estimated cost ($USD)
AM2-4-8.5	1.20*/ 1.20*	0.009*	upgrade	None	$2.2 M
AM2-5	1.21 / 1.22	0.012	upgrade	None	$2.5 M
Arm-4	1.45*/ 1.45*	0.007*	not feasible	2.0%	>$12.6M
AM2-4	1.23 / 1.22	0.05	upgrade	6.6%	$2.2 M
AM2-8	1.24 / 1.24	0.016	upgrade	3.0%	$3.4 M
Arm-1	1.23 / 1.10	0.41	first light	6.6%	$10.2 M
Arm-2	1.22 / 1.21	0.09	first light	3.0%	$11.4 M

*These values are interpolated from results at 0.6 and 1.25μm

Table 6.5. Rough cost estimates for various items in ($USD).

item	cost
Adaptive secondary - provided for other instruments	$0 M
NGS WFS - provided for WFOS without GLAO	$0 M
LGS beacons - provided for other instruments	$0 M
LGS WFS - per unit	$0.3 M
Arm Collimator - per arm - DM $1M (~$1.25 k per actuator) - 3 Mirrors $1M	$2.0 M
Other costs	$1 M

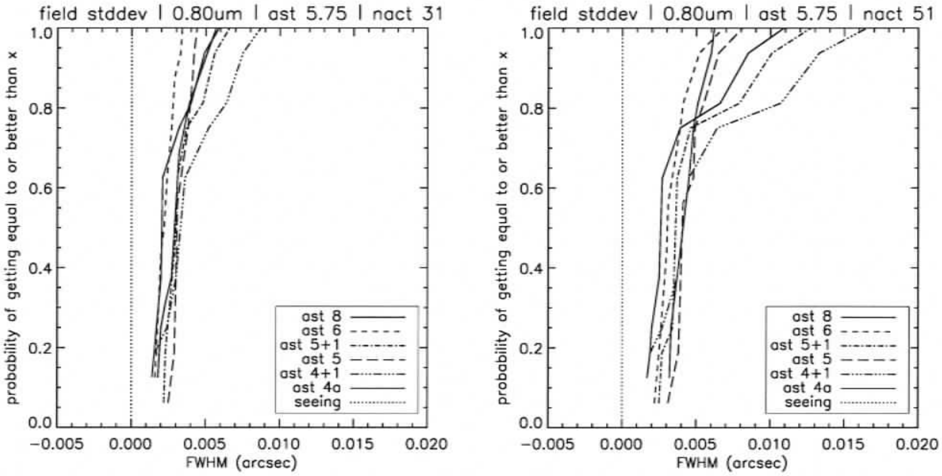

Figure 6.7 Cumulative histograms of field standard deviation rather than mean of FWHM. Here we see that all of the +1 asterisms (dash-dotted curves) produce much more PSF nonuniformity when the low altitude turbulence is strong. The only thing distinguishing the +1 asterism from the non +1 with the same total number of guide stars is the increased nonuniformity.

6.4.2 Architecture, performance, cost and the baseline design

Table 6.4 summarizes the characteristics of each of the systems. Image quality is assessed using ITR. The ITR values quoted in the table are the field mean and median values. The PSF non-uniformity is represented by the field standard deviation of the ITR values. The vignetting value is the percent of the field obscured by the LGS WFS pickoff mirrors. Note that these are a lower bound on the actual vignetting, since they only consider the minimum size of mirror required, and do not consider mechanical elements required to support the mirrors. The cost estimation is detailed in Table 6.5.

Among the Arm designs only Arm-4 is competitive. Arm-1 and Arm-2 also demand four single conjugate DMs that may rival the cost and complexity of AM2 alone. When an LGS is placed in the science field there is higher non-uniformity of the correction, in addition to the problem of gathering the light with vignetting pick-off mirrors or impossible beamsplitters. Having an LGS in or near the field also does not appreciably increase the field mean ITR. For these reasons we eliminate Arm-1 and Arm-2.

AM2-4 is also not preferred as it also suffers from PSF non-uniformity and vignetting.

AM2-8 and Arm-4 demand eight and twelve LGS beacons, the latter also requiring four single conjugate DMs that may rival the cost and complexity of AM2.

AM2-5 was previously chosen as the baseline design, but AM2-4-8.5 is the final preferred baseline as it provides similar performance and accommodates system design considerations (§6.5).

The simulations in Table 6.4 used the CP atmospheric scenario with the DM conjugated to zero meters in every case, which is well conjugated with the turbulence. AM2 is a Gegorian secondary and will in fact be conjugated to +300 meters and for the 1 meter pitch and 17 arcminute field of view simulated here the gradual gray zone transition [Tok04] starts around 200 meters from the DM and thus has an impact on accurate performance predictions, but does not impact the differential performance used for the trade studies.

The Arm configurations require more initial investment and risk in WFOS for an ITR of 1.45 rather than 1.20 with AM2 (at $0.8\mu m$). Hence the possibility of the AM2 upgrade for other TMT adaptive optics systems makes AM2 very attractive as the primary corrector for WFOS-GLAO.

6.5 Baseline system design

In the previous sections we evaluated the performance of GLAO and performed basic system trades. In this section, we examine each of the sub-systems and their requirements.

6.5.1 Deformable mirror

The baseline design will use an adaptive secondary mirror (AM2) for wave-front correction. All the other TMT AO systems would use AM2 only as a woofer, which relaxes their requirements. It is therefore important to make sure that the AM2 woofer will be suitable as the primary corrector for GLAO. Our assumptions on the characteristics of AM2 are based on the preliminary results of a feasibility study for AM2 carried out by *Sagem*.

Actuator density

The expected inter-actuator spacing on AM2 itself is 6 to 8 *cm* across a mirror ~3.5 meters. This works out to be between 43 and 58 actuators across the pupil diameter. The actuators will be arranged in a hexagonal pattern. One should remember however that it may be not possible to apply some high spatial frequency modes to AM2, because too much force would be required. Hence AM2 will be equivalent to an unconstrained DM with a lower actuator density. It is reasonable to assume that the AM2 woofer will perform at least as well as an unconstrained DM with 30x30 rectangular grid and will perform somewhat worse than a 50x50 DM, which were simulated in §6.4.1.

Temporal bandwidth

Based on the AM2 design study by Sagem we expect to achieve a temporal bandwidth for AM2 between 100 and 1000 Hz (-3 dB bandwidth). AM2 will be slower than a normal piezo-based DM (which can be assumed perfect) and thus it is interesting to investigate the effect on delivered image quality. Our analytical modeling of GLAO does not allow us to input any dynamic properties of the DM, which is assumed to be perfect. It does allow us to change the time delay in the AO loop. The worst bandwidth (100Hz) is equivalent to a 3 millisecond time delay in the loop. For this pathological case we also choose a severely strong wind model with 20 meter per second wind below 2000 meters and 5 C_n^2 profiles from the T1 database selected for strong turbulence below 2000 meters and weak turbulence above. We find that with a pitch of 1 meter, 500 Hz frame rate and a 3 millisecond AM2 delay the performance degradation was less than 1% in ITR and therefore conclude that a 100Hz AM2 will have no impact on GLAO performance.

6.5.2 LGS WFS

Polar coordinate CCDs

The baseline configuration for WFOS-GLAO is to use four or five LGS WFSs. A well known problem with LGS wavefront sensing on a 30 meter telescope is that off-axis sub-apertures see the thickness of the sodium layer and produce a radially elongated spot: at the centre of the pupil, the spot is typically circular and has an FWHM of ~1 arcsec. At the edge of the pupil, the size of the spot is still ~1 arcsec in the tangential direction, but is ~4 arcsec in the radial direction. An elongated spot produces a noisier measurement and to mitigate this effect, we plan to use CCDs with a radial geometry (Fig.6.8) and special clocking [AAN06]. They are being developed and are the baseline for the Narrow Field Infra-Red Adaptive Optics System (NFIRAOS) for TMT. In each sub-aperture the CCD has a rectangular pixelated area (e.g. 12x6) which has a radial orientation that puts the long side of the rectangle parallel to the direction of the spot elongation. All of the pixels in the radial direction will be used to account for the thickness and structure of the sodium layer using techniques such as match filtering [GE06]

Non-common path aberrations

TMT is currently an aplanatic Gregorian telescope and therefore produces anastigmatic off-axis images. For the same reason, the image of an off-axis source not at infinity, such as an LGS, will also be degraded by coma, which is a function of the range distance. In the baseline configuration with four LGSs at 7.5 arcmin off-axis. A Zemax analysis finds that the image of these LGSs will be affected by astigmatism and coma given in Table 6.6. Other aberrations are insignificant. Z=85 km

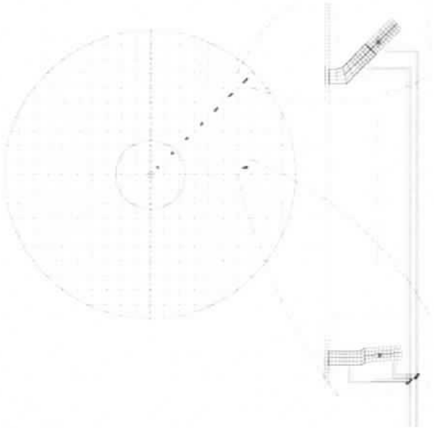

Figure 6.8 A radial format CCD. Diagram provided by Sean Adkins.

Table 6.6. Amount of static astigmatism and coma aberrations that will degrade the image of an LGS at 7.5 arcmin off-axis, for different range distances, in micron RMS of wave-front error. This number is converted in arcsec of WFS spot displacement, for a spot at the edge of the telescope pupil.

	Astigmatism	Coma
Z=85 km	-2.40μm RMS	-1.78μm RMS
	-0.16 arcsec	-0.48 arcsec
Z=150 km	-2.39μm RMS	-1.04μm RMS
	-0.16 arcsec	-0.28 arcsec
Z=85 km - Z=150 km	-0.01μm RMS	-0.74μm RMS
	0.00 arcsec	-0.2 arcsec

corresponds to the lowest expected position of the sodium layer at zenith. Z=150 km corresponds to the expected height of the sodium layer at $\sim$ 55 degree zenith angle.

These aberrations will not significantly affect WFS spot images. However, each spot will be offset and the WFS will measure these aberrations. These aberrations are in the non-common path and should not be corrected by the DM. They can be removed by two different methods: 1) Correcting the aberrations optically before the WFS lenslet array or 2) Using the spot position corresponding to these aberrations as reference position and drive the spots to these positions (offset slopes).

Table 6.7. FWHM, EE50 and ITR of the seeing PSF, and the GLAO corrected PSF with an increasing amount of static coma added.

	seeing values	GLAO values with residual RMS coma of $0\mu m$	$0.25\mu m$	$0.5\mu m$	$0.75\mu m$	$1.0\mu m$	$1.25\mu m$	$1.5\mu m$
FWHM(sec)	0.18	0.15	0.15	0.16	0.17	0.18	0.19	0.21
EE50 (sec)	0.29	0.21	0.22	0.23	0.25	0.27	0.29	0.30
ITR	1.00	1.42	1.39	1.30	1.17	1.03	0.90	0.78

The optical correction method is best from the standpoint of the AO control system, because it is transparent. Astigmatism does not depend on the LGS range distance and is therefore fairly easy to correct optically. Coma varies with range distance and therefore requires a moving corrector, which is much more involved.

The offset slopes correction method simplifies the opto-mechanical design, but suffers from two potential drawbacks: firstly, it uses a significant amount of dynamic range on the WFS: secondly, unavoidable calibration errors will make it so that only a fraction of the aberrations can be removed using this method. Experience with calibration of AO systems suggests that only a factor 3 to a factor 5 attenuation in RMS may be achieved with offset slopes. Table 6.6 also shows the offset slopes required to correct for each aberration, at the edge of the pupil, which is the worst case. These numbers are simply calculated by taking the derivatives of the corresponding Zernike polynomials. From the dynamic range standpoint, the WFS could fully correct these aberrations electronically using offset slopes. So we must now discuss the implications on the science image of only correcting these aberrations by a factor of 3 to 5, because of calibration errors.

We focus our discussion on coma, because astigmatism is not a function of the range distance and can be easily corrected by a static optical corrector. Therefore we study the impact on the science image of leaving an increasing amount of uncorrected coma. The results are given for the best seeing case in Table 6.7. We therefore find that if the static coma corrector reduced the $1.78\mu m$ RMS coma when pointed at zenith (Z=85km Table 6.6) to 0.5μm then ITR would not be reduced by more than 9% if no electronic compensation (offset slopes) is performed. In the case when Z=150km then this static corrector would overcorrect by $\sim 0.5\mu m$, which is roughly equal and opposite uncorrected coma. With electronic compensation and in median or bad atmospheric conditions, the ITR reduction would be much less. We conclude that a static correction of coma in combination with electronic correction is acceptable. Not including a static optical corrector for coma, leaving the full 1.78μm rms of coma going through would require electronic compensation at levels that we do not believe are reasonable. Our recommendation is therefore to include a static coma corrector in the LGS WFSs.

Expected residual spot jitter

In GLAO, the LGS WFS sees a residual wave-front where the ground turbulence layer is corrected, but the rest of the turbulence is not. As a result, we can expect the WFS spots to be jittering nearly as much as when the loop is open. For the calculation we considered the tip-tilt of the uplink beam to be corrected. We also set the bottom layer of the TMT Science Requirements Document (SRD) to be perfectly corrected in the downlink. Using this turbulence profile with $r_o = 15cm$ (at 0.5μm) and $L_o \rightarrow \infty$, the root mean square spot jitter is calculated to be no more than 22.2 or 25 milliarcseconds for a pitch of 1 or 0.5 meters. This residual jitter in the LGS spots will not seriously impact WFOS-GLAO performance.

WFS linearity issues

Centroiding error as a function of local tilt for an LGS WFS using radial format CCDs with 16x4 or 12x6 pixels per subaperture is studied in [GE06]. The linearity of the LGS WFS using a matched filter algorithm for optimal centroiding suggests that if a large offset is required (e.g. to correct for the static aberrations discussed in §6.5.2) then six pixels in the tangential direction is preferable (i.e. 12x6). In this case a (1,1) pixel offset appears to be possible. This corresponds to a 0.5 arcsecond offset which, based on the results in Table 6.6 would enable electronic correction of all coma.

6.5.3 NGS WFS

GLAO will use the On Instrument WFS (OIWFS) in each barrel for NGS WFS. Using only one NGS to sense tip-tilt for each 4.5minx4.5min sub-field should be sufficient for the GLAO PSF. Three of the WFOS barrels each have 2x2 Shack-Hartmann WFS and one barrel will likely have a higher order WFS to serve as the truth WFS. The two main purposes of the truth WFS 1) to monitor the true true atmospheric focus and thereby monitor the range to the sodium layer, which then controls the LGS WFS zoom optics and 2) monitor quasi-static aberrations at the science focal plane and correct for them by providing updated reference slopes to the LGS WFSs.

Our baseline is to use a 128x128 detector that can operate at 500 full frames per second. With 0.1sec pixels this gives a 6.4 arcsecond field of view in each 64x64 pixel sub-aperture. It is desirable that at least one OIWFS has a larger field of view to make sure that the NGSs can be found even with telescope pointing errors and pick-off probe positioning errors. This avoids the overhead of pre-imaging the field. After the NGSs have been found, the telescope can be repointed and or the pick-off probes can be adjusted, until the NGSs are all centred in each WFS (see the operational model in §6.5.5).

Our baseline uses a 4 square arcminute patrol field that is inside the science field for each 2x2 OIWFS, introducing a small amount of vignetting for pick-off. As illustrated in [CEV06] this field of view will be more than sufficient to give 100% sky coverage for sensing tip-tilt for WFOS-GLAO on TMT.A slightly larger patrol area would be desired for the truth WFS with 6x6 sub-apertures that also runs at 500 frames per second to monitor the sodium layer range.

6.5.4 Calibration sources

WFOS does not have any entrance focal plane, so we are not considering outfitting the instrument with any source simulator that could be seen in the WFOS focal plane. There is the possibility of a deployable source in each of the LGS WFS arms. They would be just after the pick-off mirror / zoom corrector and just before the coma / astigmatism corrector. Such calibration sources could be used to:

- Measure the aberrations generated by the coma / astigmatism corrector and check that they are what they are supposed to be.
- Check pupil centring on the WFS lenslet array.
- Measure static aberrations that need to be considered as non-common path aberrations.

In order to access the WFOS focal plane, sources will have to be deployed at the TMT Prime focus. It would be useful to have just one LGS source that could feed an LGS WFS. Such a source would allow registration of the AM2 and WFSs, as well as test the sodium range compensation optics. Such an LGS source would not necessarily need to simulate the cone effect. However, it would need to simulate the finite range of the sodium layer, with the ability to vary this range. One LGS source would make it possible to close the AO loop on one LGS.

An additional NGS calibration source at the TMT Prime Focus would also be very desirable to monitor the image quality when the AO loop is closed on the LGS calibration source. It would need to be accessible from the truth WFS at least, and by all the other OIWFSs if possible.

6.5.5 GLAO specific operations

The baseline system design would include the following.

Daytime perparation

- Measure LGS WFS CCD noise level

- Deploy calibration source in each LGS WFS arm
- Check that the pupil is well centred on the lenslet arrays
- Check that the LGS WFS reads the correct coma correction

Observations start

- For the reasons explained in §6.3.1 there will be negligible observational overhead with the chosen baseline system. To aid this we would start the WFOS observations only with tip-tilt and focus correction using OIWFSs and the secondary mirror (OIWFS-M2 loop).

Enabling GLAO correction

- Open the laser shutters
- Adjust LGS positions (using LGSF steering mirrors) until the LGSs are properly centred on each LGS WFS.
- Check flux on LGS WFSs.
- Detune laser and record background image. This image will measure sky background, including Raleigh back-scattering and will be subtracted from the WFS measurements.
- Retune laser.
- Enable uplink T/T correction loop to stabilize LGS spots.
- Close high order GLAO loop using low loop gains to minimize transients that would perturb on-going science integration.
- Slowly ramp up the loop gains until the correction is optimal, while checking for system stability.
- The GLAO loop can remain closed during dithers or nods, as in nod-and-shuffle operation.

6.6 Conclusions

Our preference is to rely on the adaptive secondary mirror (AM2) being considered as the woofer for other TMT AO instruments. The gains predicted for all of the designs able to uniformly correct the full 81 square arcminutes are all characterized by modest integration time savings and as such are best operated as a transparent assist for seeing limited observations. If we consider the AM2 to be provided with one of the other TMT AO systems, the performance benefit of four single conjugate mirrors in each barrel (Arm) over the one AM2 designs is not considered enough. The AM2 woofer is compatible with WFOS-GLAO, is more elegant, correcting the wavefront before WFOS without crowding the spectrograph.

The Natural Guide Star WFSs for GLAO would be the same OIWFSs needed for the seeing-limited mode. For LGS WFS at over 7.5 arcminutes off axis we need static coma corrector optics on each LGS WFS. The remainder of the aberrations can be corrected using offsets to LGS spots.

The preliminary predictions of efficiency for the baseline wide field GLAO design are promising. Looking at Fig.6.3 it seems likely that this design will provide an efficiency ratio of 1.1 in at visible wavelengths and as much as 1.4 toward J band. We find that a GLAO system would not introduce any additional overhead, including guide star acquisition, and is compatible with all the WFOS observing modes, including Nod-And-Shuffle. The WFOS-GLAO PSF will have a morphology similar to the seeing limited PSF, which means that GLAO can potentially be turned on or off during an exposure with no drastic consequence on the data quality, only a gain in efficiency when GLAO is turned on. This makes AM2 GLAO a very appealing AO mode for WFOS.

Chapter 7

Conclusions

Wide field adaptive optics (WFAO) is currently represented by Altair, the first altitude conjugated AO system. In Part One we identified and planned *sparse field* observations to assess the wide field performance (listed in Appendix A.1). All of the basic aspects of Altair's performance were also characterized for use by the community to plan observations. We identified and quantified degradation of the images due to vibration and secondary mirror print-through aberrations. The *PSF database* is versatile and ready to for analysis of Altair's wide field performance using PSF models such as *PAOLA* or other analytic models for a solo WFS and solo DM on the sky as was done by [SMG05] and the anisoplanatism studies by [vSB06, Bri06]). We also investigated and reported on the extrapolation scheme used when Altair operates in altitude conjugated mode. The scheme called *method 2*b which re-weights the edge actuators is better than the implemented scheme called *method 2*a.

In Part Two we explore the next generation of WFAO using a model derived for GLAO. The model is implemented in *GLiFFT* for the purpose of feasibility and trade studies. It is an efficient code for rapidly computing the PSF resulting from the fundamental GLAO error sources (lag,cone, and angular anisoplanatism). The *GLiFFT* code will be made publicly available and is planned for use with the results of the Gemini GLAO site testing campaign mentioned in §1.5. The speed is an advantage especially for converting the large $C_n^2(h)$ data sets directly into PSFs. The resulting PSF statistics will also serve the development of $C_n^2(h)$ models.

The *GLiFFT* model was used with greatest significance to establish the very wide GLAO (VWGLAO) regime. The regime is defined to be where GLAO provides theoretical gains over seeing limited surveys. We also showed that the lag anisoplanatism and therefore noise are negligible effects compared to the angular anisoplanatism in two example VWGLAO cases.

In Part Two we also used the model primarily for trade studies of the GLAO system proposed for the Wide Field Optical Spectrograph (WFOS) on the Thirty Meter Telescope (TMT). It was decided that correcting the whole WFOS field (81 square arcminutes as defined in the science requirements document) using the laser guide star (LGS) and adaptive secondary (AM2) facilities purchased for other extended AO systems has a significant benefit. Additional adaptive optics inside of WFOS would be costly. This very wide design has the benefit of uniform correction for a transparent assist of seeing improved observations on an adaptive TMT (cf. right panel Fig.1.5). There are three things identified as important improvements to the work presented in Chapter 6.

- Accurate simulation of DM conjugation is important to the WFOS-GLAO study, and as pointed out in Chapter 6 the gray zone for that design is from 0 to 100 meters then 500 meters and above which may have peculiar effects. The *GLiFFT* model the is lacking a trusted method for modeling altitude conjugation (see z' in Chapter 4) and this should be developed.

- Predictions of performance presented here where for generalized science, using ITR and ITRS metrics. With more time these predictions would have been made for specific programs with simulated astrophysical observations. The metrics are very effectively used as diagnostic tools for the GLAO PSF, especially ITR.

- Uncorrected telescope aberrations may be important to the blue and UV wavelength predictions in the WFOS-GLAO study and should be studied.

An area that the analytic modeling of just the fundamental error sources has contributed greatly, is in fostering intuitive understanding and development of simpler analytic forms for the fundamental error sources. Several analytic approximations have been discovered through the development of the analytic models, including a GLAO structure function for the n^{th} layer.

$$D_n(\xi) = \frac{D_{seeing}(\xi)}{1 + \left(\frac{4r_o}{\varsigma_n}\right)^{5/3} D_{seeing}(\xi)} \tag{7.1}$$

The seeing structure function (D_{seeing}) for von Karman turbulence is given in [HS90] and [Sas94] Eqn.(12.46). The ς_n is the characteristic length shorter than which the system cannot correct, which essentially defines the r of the relatively sharp knee in the GLAO structure function.

$$\varsigma_n = \Delta \quad \text{or} \quad z_n\theta \quad \text{whichever is bigger} \tag{7.2}$$

Where the actuator pitch is Δ and layer height times asterism diameter is $h\theta$. Eqn.(7.1) is an improvement on one by [Tok04] as it includes pitch and a outer scale, important for the uncorrected high altitude layers, especially on a TMT. The structure function definition can quickly give the PSF with an accurate FWHM and serves as a sampling pre-conditioner for more realistic models.

Given the useful and uniform correction in a circular asterism we also developed a model using the azimuthally symmetric PSD Eqn.(4.20) and Henkel transforms implemented in *Glitter* . Benchmarks with *GLiFFT* currently show that the anticipated computer memory savings of *Glitter* are useful. However the CPU time is comparable to *GLiFFT* , which benefits greatly with the efficiency of the FFT algorithm. Implementation of Henkel transform techniques of [BPS98] or [Ham00] would reduce the number of multiply and adds, potentially improving the speed of *Glitter* by 100 fold. We identify the following future work for GLAO models to be the most interesting:

- The modeling work presented here can help the search for a closed from PSF model, suited to data reduction for GLAO or near-seeing limited data from ELTs. As the Moffat PSF model does for seeing limited images where Kolmogorov statistics apply. We foresee a need for more realistic atmospheric models, including accurate $C_n^2(h)$ as well as $L_o(h)$ and perhaps other non-Kolmogorov effects.

- Implementation of different actuator geometries in *GLiFFT* to more accurately assess the second most important fundamental GLAO error source, fitting error.
- NGS noise models and beacon weighting schemes for revisiting the usefulness of the pyramid WFS.

As a final note, we would like to remind the reader that GLAO is the natural AO mode of an adaptive telescope that will be used where LGS and AM2 facilities exist. The extremely large telescopes of the future have science goals using a contiguous wide field ($\gtrsim$ 30 square arcminutes per pointing) and will likely operate in the VWGLAO regime, which has no additional overhead for seeing improved operation.

Appendix A

Evaluation of the on-sky performance of Altair

A.1 Selected sparse fields

Table A.1 lists sparse fields selected using the criteria in table 2.2, to span RA, and have uniform infrared magnatudes and at least one bright visible star for guiding with full correction. All fields have 3, 4, or 5 stars that can be simultaniously imaged in the infrared. In most cases only the brightest and second brightest visible star have a V magnitude listed on this table. Any of the other stars are useful as faint guide stars. The USNO catalogue *J* and *F* magnitudes were transformed to B and V using the formulation by [Inf94]. The H magnitudes are as published in the 2MASS all-sky catalogue [CSv03]. The best quality sparse fields for Gemini North (20°N) are around 17h to 22h RA, where the bulk of the Milky Way is.

The work in this section has made use of the *VizieR* catalogue access tool, CDS, Strasbourg, France.

Table A.1. The selected sparse fields.

Field name	RA (J2000)	Dec (J2000)	separation from base (arcsec)	(B-V)	V	H
baq-56	00 28 51.2	+28 32 07.2	0.0	-	-	11.8
baq-56	00 28 52.0	+28 32 07.2	10.4	1.1	11.0	10.5
baq-56	00 28 51.4	+28 32 09.6	5.9	-	-	11.4
baw-34	01 23 53.2	+41 35 29.8	0.0	1.2	11.4	11.6
baw-34	01 23 53.8	+41 35 35.3	9.0	-	-	12.1
baw-34	01 23 52.8	+41 35 38.1	9.6	-	-	12.3
baw-34	01:23:53.2	+41:35:36.0	6.2	-	12.2	10.9
bay-2	02 47 57.1	+44 24 14.1	0.0	-	-	12.2
bay-2	02 47 58.0	+44 24 19.3	11.6	1.0	11.7	11.5
bay-2	02 47 56.5	+44 24 21.7	9.8	-	-	12.2
bay-26	03 36 09.5	+45 16 25.5	0.0	-	-	10.4
bay-26	03 36 08.8	+45 16 27.7	7.1	1.5	10.6	10.0
bay-26	03 36 08.4	+45 16 32.4	13.0	-	-	9.9
bas-47	05 52 11.8	+32 34 23.4	0.0	-	-	11.6
bas-47	05 52 12.6	+32 34 28.5	10.7	-	10[d]	10.9
bas-47	05 52 11.8	+32 34 33.9	10.5	-	-	12.0
bas-47	05:52:13.3	+32:34:16.8	19.6	-	11[d]	10.9
bat-63	05 29 11.7	+34 51 40.0	0.0	-	-	11.6
bat-63	05 29 10.7	+34 51 42.1	12.5	-	-	11.9
bat-63	05 29 12.2	+34 51 49.4	11.8	0.0[d]	10.6	10.6
bak-17	06 30 34.4	+17 10 05.0	0.0	-	-	11.8

Table A.1 (cont'd)

Field name	RA (J2000)	Dec (J2000)	separation from base (arcsec)	(B-V)	V	H
bak-17	06 30 33.9	+17 10 13.6	11.3	1.8	9.8	10.0
bak-17	06 30 34.9	+17 10 14.5	11.8	1.3	10.8	11.1
bat-34	06 46 14.5	+34 17 40.5	0.0	-	-	11.0
bat-34	06 46 13.5	+34 17 43.7	12.8	0.4	9.6	9.7
bat-34	06 46 14.3	+34 17 47.2	7.0	-	-	10.7
baf-71	07 48 37.6	+08 37 43.4	0.0	1.5	9.9	9.4
baf-71	07 48 36.8	+08 37 47.5	12.3	-	-	11.5
baf-71	07 48 37.8	+08 37 54.8	11.9	-	-	11.9
abr-643	07 58 48.7	-20 17 53.7	0.0	-	-	11.3
abr-643	07 58 49.4	-20 17 52.4	9.4	2.0	9.7	9.8
abr-643	07 58 48.1	-20 17 50.7	9.1	-	-	10.5
abr-643	07 58 48.7	-20 17 42.3	11.5	-	-	12.5
abr-643	07 58 49.7	-20 17 57.2	13.1	0.8	11.5	10.3
baf-268	11 09 25.0	+09 18 57.9	0.0	-	-	10.9
baf-268	11 09 25.1	+09 19 05.1	7.3	-	-	11.8
baf-268	11 09 24.6	+09 19 09.5	13.0	1.5	11.3	10.5
baq-179	15 09 22.8	+29 30 49.0	0.0	-	-	11.3
baq-179	15 09 22.8	+29 30 55.2	6.2	1.1	10.6	11.0
baq-179	15 09 23.1	+29 31 00.5	12.0	-	-	11.1
baq-146	19 30 43.5	+29 12 35.7	0.0	-	-	11.5
baq-146	19 30 44.3	+29 12 35.9	10.4	1.5	10.9	10.2

Table A.1 (cont'd)

Field name	RA (J2000)	Dec (J2000)	separation from base (arcsec)	(B-V)	V	H
baq-146	19 30 42.9	+29 12 39.9	9.6	-	-	11.4
baq-146	19 30 43.9	+29 12 40.8	7.3	-	-	11.4
bar-41	19 43 08.0	+30 27 40.3	0.0	-	-	11.0
bar-41	19 43 08.7	+30 27 41.7	10.0	-	-	11.3
bar-41	19 43 07.3	+30 27 44.7	10.0	-	-	12.4
bar-41	19 43 08.0	+30 27 52.5	12.2	-	11[d]	10.0
baw-5	20 08 30.4	+40 11 26.8	0.0	1.1	10.7	9.3
baw-5	20 08 31.3	+40 11 32.1	11.4	-	-	11.2
baw-5	20 08 30.5	+40 11 36.8	10.1	-	-	11.9
bax-30	21 45 58.4	+43 37 56.2	0.0	-	-	11.0
bax-30	21 45 59.1	+43 37 59.1	8.2	0.6	10.3	9.9
bax-30	21 45 58.6	+43 38 04.9	10.8	-	-	11.0
baq-94	22 08 57.7	+28 48 13.1	0.0	-	-	10.3
baq-94	22 08 58.6	+28 48 18.8	12.6	-	-	10.8
baq-94	22 08 57.9	+28 48 20.0	7.2	1.0	10.0	9.9
bba-28	23 10 27.7	+49 30 04.6	0.0	1.2	10.8	10.7
bba-28	23 10 26.4	+49 30 05.5	12.5	0.3	12.7	10.6
bba-28	23 10 27.6	+49 30 12.6	8.1	-	-	10.9

[d] This magnitude is estimated by eye from plate scans because of source confusion in the catalogue.

Appendix B

Control of the unilluminated actuators in Altair

B.1 Finding degenerate analysis pupil configurations

It was mentioned in a previous section that the number of discrete analysis pupil configurations can be reduced to a minimal set because many of the configurations can be made degenerate by simple transformations. Altair's existing system design [V01] takes advantage of the translation to make degeneracies. Altair expects covariance matrices (method 2) calculated on the 19x19 (18x18 pitches) virtual DM and the actual DM is a circle that is about 14 pitches in diameter, and hence a configuration centred on actuator 180 and another centred on actuator 181 can use the same matrices and all of the real (servoed) actuators in both are accounted for by the oversized virtual DM. Calculating for a particular configuration on the larger virtual DM leads to, say N calculations and would be N' calculations on just the real actuators. While $N' < N$ the calculations on the virtual DM will cover M other configurations made degenerate by translation, where as $N' \times M$ calculations would be needed to provide the same coverage the other way. In fact $N < N' \times M$ for our 19x19 virtual DM and circular 14 pitch diameter DM.

With translation, a finite set of locations of analysis pupil centres in a one square pitch area around the actuator at the centre of the virtual DM will provide all of the

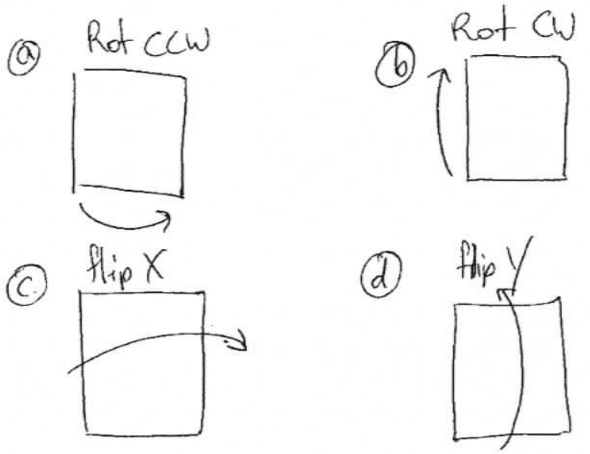

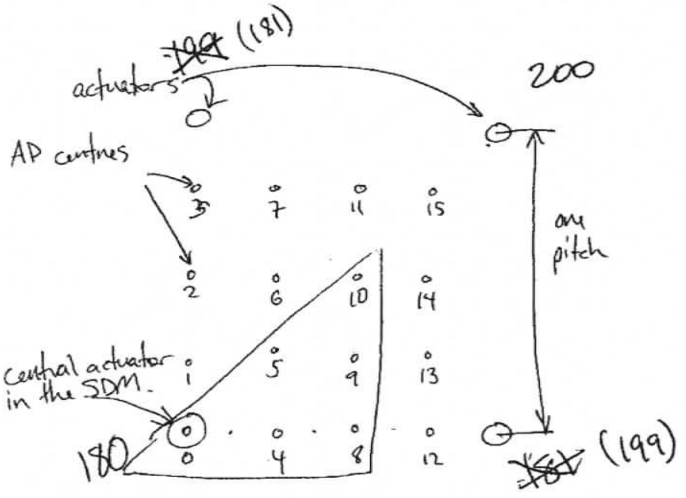

Figure B.1 The locations of the analysis pupil centres for the MC simulations.

needed covariance matrix pairs needed by Altair. Previous planning called for Altair to have 16 discrete locations in this one square pitch area ([V01]). Unfortunately this area was chosen to be offset a little in x and y from the central actuator (see Fig. B.1). The reason it is unfortunate will be explained after we describe how more degeneracy exploited.

By executing a coordinate transformation on the actuators of the virtual DM we can map actuators from one analysis pupil location (configuration) to the matching set of another analysis pupil location. The transformations are a flip and a rotation by 90^o. For example, the Fig.B.2 below shows the set of actuators for a NGS analysis pupil centred at location 1 (left panel) and one at location 4 (right panel).

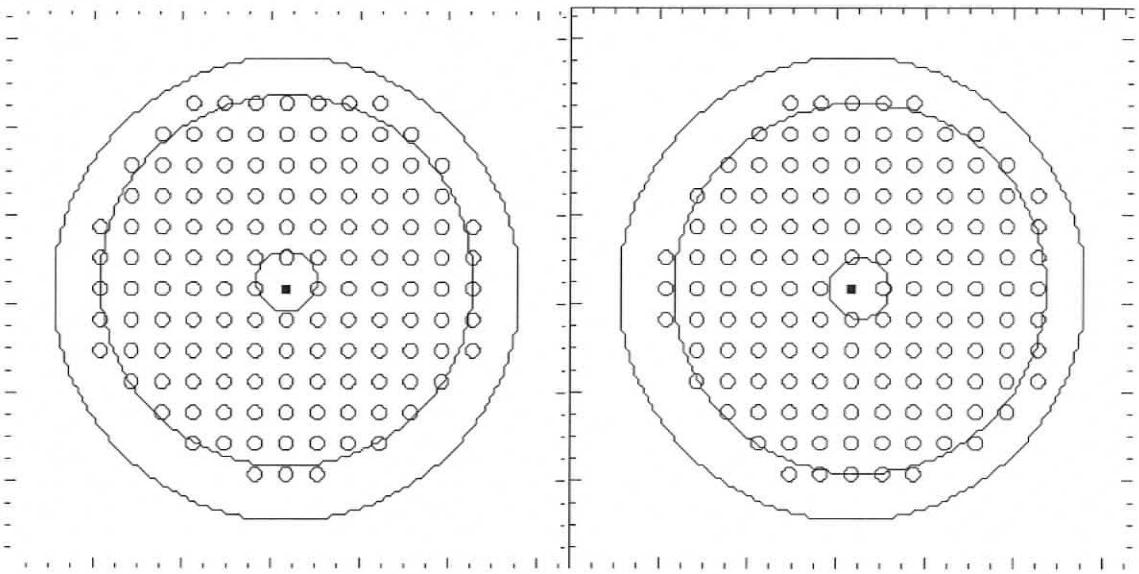

Figure B.2 Left panel: he analysis pupil centred at location 1 showing $\mathbf{m}_{gs}$. Right panel: The analysis pupil centred at location 4 showing $\mathbf{m}_{gs}$.

Actuator 64 in configuration 1 maps to actuator 148 in configuration 4 with a rotation about the central actuator.Therefore configuration 1 and 4 are degenerate with this transformation.

The centre of symmetry for a rotation or a flip transformation must be centred in the virtual DM so that all 360 actuators map to another actuator after the transformation. This constraint is what makes the 16 pre-defined locations for Altair unfortunate. Only three pairs can be made degenerate by a rotation: 4 and 1, 8 and 2, 12 and 3. If the patch of 16 locations was moved such that the centre of the virtual DM (and therefore the centre of symmetry) to location 10 then we could get configurations 1,2,3,6,7,11,12,13,14,15 from a variety of transformations of configurations 4,8,5,9. This means that each of the covariance matrices for configurations centred at 1,2,3,6,7,11,12,13,14,15 would not need to be calculated by Monte Carlo iterations, but instead can be derived by shuffling the rows and columns of one of the 4,8,5,9 set and reducing computation time by a factor of ~ 2.67.However, with the chosen locations, we can only shuffle to get three of the 16.

Bibliography

[AAN06] S. M. Adkins, O. Azucena, and J. E. Nelson. "The design and optimization of detectors for adaptive optics wavefront sensing." In *Proceedings of the SPIE, Volume 6272 (2006).*, July 2006.

[ACS06] D. R. Andersen, D. Crampton, K. Szeto, S. Morris, M. Lloyd-Hart, R. Myers, J. A. Stoesz, T. Butterley, M. Milton, J.-P. Véran, and R. Wilson. "Modeling a GLAO system for the Gemini Observatory." *PASP*, 2006. *submitted.*

[Bab53] H. W. Babcock. "The Possibility of Compensating Astronomical Seeing." *PASP*, **65**:229–+, October 1953.

[Bec88] J. M. Beckers. "Increasing the Size of the Isoplanatic Patch with Multiconjugate Adaptive Optics." In M.-H. Ulrich, editor, *Very Large Telescopes and their Instrumentation, ESO Conference and Workshop Proceedings, Proceedings of a ESO Conference on Very Large Telescopes and their Instrumentation, held in Garching, March 21-24, 1988, Garching: European Southern Observatory (ESO), 1988, edited by Marie-Helene Ulrich., p.693*, pp. 693–+, 1988.

[BMK04] G. Brusa, D. L. Miller, M. A. Kenworthy, D. L. Fisher, and A. Riccardi. "MMT-AO: two years of operation with the first adaptive secondary." In D. Bonaccini Calia, B. L. Ellerbroek, and R. Ragazzoni, editors, *Advancements in Adaptive Optics. Edited by Domenico B. Calia, Brent L. Ellerbroek, and Roberto Ragazzoni. Proceedings of the SPIE, Volume 5490, pp. 23-33 (2004).*, pp. 23–33, October 2004.

[BPS98] R. Barakat, E. Parshall, and B. H. Sandler. "Zero-order Hankel transformation algorithms based on Filon quadrature philosophy for diffraction optics and beam propagation." *Optical Society of America Journal A*, **15**:652–659, March 1998.

[Bri06] M. C. Britton. "The Anisoplanatic Point-Spread Function in Adaptive Optics." *PASP*, **118**:885–900, June 2006.

[BW99] M. Born and E. Wolf. *Principles of optics. Electromagnetic theory of propagation, interference and diffraction of light.* Cambridge University Press, 1999, 7th expanded ed., 1999.

[CAC05] E. Carrasco, R. Avila, and A. Carramiñana. "High-Altitude Wind Velocity at Sierra Negra and San Pedro Mártir." *PASP*, **117**:104–110, January 2005.

[CEV06] R. M. Clare, B. L. Ellerbroek, J.-P. Véran, G. Herriot, and D. Andersen. "Sky coverage and tip/tilt error analysis for TMT." In *Proceedings of the SPIE, Volume 6272 (2006).*, July 2006.

[Col92] G. P. Collins. "Making stars to see stars - DOD adaptive optics work is declassified." *Physics Today*, **45**:17–21, February 1992.

[CSv03] R. M. Cutri, M. F. Skrutskie, S. van Dyk, C. A. Beichman, J. M. Carpenter, T. Chester, L. Cambresy, T. Evans, J. Fowler, J. Gizis, E. Howard, J. Huchra, T. Jarrett, E. L. Kopan, J. D. Kirkpatrick, R. M. Light, K. A. Marsh, H. McCallon, S. Schneider, R. Stiening, M. Sykes, M. Weinberg, W. A. Wheaton, S. Wheelock, and N. Zacarias. "2MASS All-Sky Catalog of Point Sources (Cutri+ 2003)." *VizieR Online Data Catalog*, **2246**:0–+, June 2003.

[EBD05] B. Ellerbroek, M. Britton, R. Dekany, D. Gavel, G. Herriot, B. Macintosh, and J. Stoesz. "Adaptive optics for the Thirty Meter Telescope." In R. K. Tyson and M. Lloyd-Hart, editors, *Astronomical Adaptive Optics Systems and Applications II. Edited by Tyson, Robert K.; Lloyd-Hart, Michael. Proceedings of the SPIE, Volume 5903, pp. 20-31 (2005).*, pp. 20–31, August 2005.

[ET98] B. L. Ellerbroek and D. W. Tyler. "Adaptive Optics Sky Coverage Calculations for the Gemini-North Telescope." *PASP*, **110**:165–185, February 1998.

[Fri65] D. L. Fried. "Statistics of a Geometric Representation of Wavefront Distortion." *Optical Society of America Journal A*, **55**:1427–1435, 1965.

[Fri82] D. L. Fried. "Anisoplanatism in adaptive optics." *Optical Society of America Journal*, **72**:52–+, January 1982.

[GE06] L. Gilles and B. Ellerbroek. "Laser guide star Shack-Hartman wavefront sensor modeling: matched-filtering wavefront-sensor nonlinearity and impact of sodium layer variability for the Thirty Meter Telescope." In *Proceedings of the SPIE, Volume 6272 (2006).*, July 2006.

[Gen95] E. Gendron. "Optimisation de la commande modale en optique adaptive: application á l'astronomie." Ph.D. dissertation (Université de Paris VII-Denis Diderot, Paris), 1995.

[Goo68] J. W. Goodman. *Introduction to Fourier Optics.* McGraw-Hill, New York, 1968.

[Ha99] G. Herriot and et al. "Altair Critical Design Documents." NRC - Herzberg Institute of Astrophysics, Victoria, 1999.

[Ham00] A. J. S. Hamilton. "Uncorrelated modes of the non-linear power spectrum." *MNRAS*, **312**:257–284, February 2000.

[Har98] J. W. Hardy, editor. *Adaptive optics for astronomical telescopes*, 1998.

[HEA06] N. Hubin, B. L. Ellerbroek, R. Arsenault, R. M. Clare, R. Dekany, L. Gilles, M. Kasper, G. Herriot, M. Le Louarn, E. Marchetti, S. Oberti, J. Stoesz, J. P. Veran, and C. Vérinaud. "Adaptive optics for Extremely Large Telescopes." In P. Whitelock, M. Dennefeld, and B. Leibundgut, editors, *IAU Symposium*, pp. 60–85, 2006.

[HJI03] K. W. Hodapp, J. B. Jensen, E. M. Irwin, H. Yamada, R. Chung, K. Fletcher, L. Robertson, J. L. Hora, D. A. Simons, W. Mays, R. Nolan, M. Bec, M. Merrill, and A. M. Fowler. "The Gemini Near-Infrared Imager (NIRI)." *PASP*, **115**:1388–1406, December 2003.

[HS90] B. J. Herman and L. A. Strugala. "Method for inclusion of low-frequency contributions in numerical representation of atmospheric turbulence." In *Propagation of high-energy laser beams through the earth's atmosphere; Proceedings of the Meeting, Los Angeles, CA, Jan. 15-17, 1990 (A91-24851 09-36). Bellingham, WA, Society of Photo-Optical Instrumentation Engineers, 1990, p. 183-192.*, pp. 183–192, May 1990.

[Inf94] L. Infante. "Counts and colours of faint stars in 5 fields near the North Galactic Pole." *A&AS*, **107**:413–418, October 1994.

[JVC06] L. Jolissaint, J.-P. Véran, and R. Conan. "Analytical modeling of adaptive optics: foundations of the phase spatial power spectrum approach." *Optical Society of America Journal A*, **23**:382–394, February 2006.

[JVM04] L. Jolissaint, J.-P. Veran, and J. Marino. "OPERA, an automatic PSF reconstruction software for Shack-Hartmann AO systems: application to Altair." In D. Bonaccini Calia, B. L. Ellerbroek, and R. Ragazzoni, editors, *Advancements in Adaptive Optics. Edited by Domenico B. Calia, Brent L. Ellerbroek, and Roberto Ragazzoni. Proceedings of the SPIE, Volume 5490, pp. 151-163 (2004).*, pp. 151–163, October 2004.

[JVS04] L. Jolissaint, J. Véran, and J. A. Stoesz. "Wide field adaptive optics upper limit performances." In *Emerging Optoelectronic Applications. Edited by Jabbour, Ghassan E.; Rantala, Juha T. Proceedings of the SPIE, Volume 5382, pp. 468-477 (2004).*, pp. 468–477, July 2004.

[Kol41] A. N. Kolmogorov. "in Dissipation of energy in a locally isotropic turbulence." *Doklady Akad. Nauk SSSR*, **32**:141, 1941. (English translation in: American Mathematical Society Translations 1958, Series 2, Vol 8, p. 87, Providence R.I).

[LH06] M. Le Louarn and N. Hubin. "Improving the seeing with wide-field adaptive optics in the near-infrared." *MNRAS*, **365**:1324–1332, February 2006.

[MLC03] D. G. Monet, S. E. Levine, B. Canzian, H. D. Ables, A. R. Bird, C. C. Dahn, H. H. Guetter, H. C. Harris, A. A. Henden, S. K. Leggett, H. F. Levison, C. B. Luginbuhl, J. Martini, A. K. B. Monet, J. A. Munn, J. R. Pier, A. R. Rhodes, B. Riepe, S. Sell, R. C. Stone, F. J. Vrba, R. L. Walker, G. Westerhout, R. J. Brucato, I. N. Reid, W. Schoening, M. Hartley, M. A. Read, and S. B. Tritton. "The USNO-B Catalog." *AJ*, **125**:984–993, February 2003.

[New52] I. S. Newton. *Opticks; or a Treatise of the Reflections, Refractions Inflections, and Colors of Light.* Opticks by Sir. Isaac Newton New York, NY: Dover Publications, INC., 1952, 1952.

[Nol76] R. J. Noll. "Zernike polynomials and atmospheric turbulence." *Optical Society of America Journal A*, **66**:207–211, March 1976.

[Obu49] A. M. Obukhov. "Structure of the temperature field in turbulent flows." *Isv. Geogr. Geophys. Ser*, **13**:58–69, 1949.

[PFM06] J. S. Pazder, M. Fletcher, and C. Morbey. "The optical design of the wide field optical spectrograph for the Thirty Meter Telescope." In *Advances in Stellar Interferometry. Edited by Monnier, John D.; Schöller, Markus; Danchi, William C.. Proceedings of the SPIE, Volume 6269 (2006).*, July 2006.

[PRA06] J. Pazder, S. Roberts, R. Abraham, A. Anthony, M. Fletcher, T. Hardy, D. Loop, and S. Sun. "WFOS: A Wide Field Optical Spectrograph for the Thirty Meter Telescope." In *Proceedings of the SPIE, Volume 6269 (2006).*, July 2006.

[Rag96] R. Ragazzoni. "Pupil plane wavefront sensing with an oscillating prism." *Journal of Modern Optics*, **43**:289–293, 1996.

[RE95] R. Racine and B. L. Ellerbroek. "Profiles of nighttime turbulence above Mauna Kea and isoplanatism extension in adaptive optics." In *Proc. SPIE Vol. 2534, p. 248-257, Adaptive Optical Systems and Applications, Robert K. Tyson; Robert Q. Fugate; Eds.*, pp. 248–257, August 1995.

[RG92] F. Rigaut and E. Gendron. "Laser guide star in adaptive optics - The tilt determination problem." *A&A*, **261**:677–684, August 1992.

[Rig02] F. Rigaut. "Ground Conjugate Wide Field Adaptive Optics for the ELTs." In *Beyond conventional adaptive optics, held May 7-10, 2001, Venice, Italy. Edited by E. Vernet, R. Ragazzoni, S. Esposito, and N. Hubin. Garching, Germany: European Southern Observatory, 2002 ESO Conference and Workshop Proceedings*, volume 58, 2002.

[Rod99] F. Roddier. *Adaptive Optics in Astronomy.* Cambridge University Press, 1999.

[RSA98] F. Rigaut, D. Salmon, R. Arsenault, J. Thomas, O. Lai, D. Rouan, J. P. Véran, P. Gigan, D. Crampton, J. M. Fletcher, J. Stilburn, C. Boyer, and P. Jagourel. "Performance of the Canada-France-Hawaii Telescope Adaptive Optics Bonnette." *PASP*, **110**:152–164, February 1998.

[RVL98] F. J. Rigaut, J. Veran, and O. Lai. "Analytical model for Shack-Hartmann-based adaptive optics systems." In *Proc. SPIE Vol. 3353, p. 1038-1048, Adaptive Optical System Technologies, Domenico Bonaccini; Robert K. Tyson; Eds.*, pp. 1038–1048, September 1998.

[Sas94] R. J. Sasiela. *Electromagnetic wave propagation in turbulence. Evaluation and application of Mellin transforms.* Springer Series on Wave Phenomena, Berlin: Springer, —c1994, 1994.

[Sed98] G. Sedmak. "Performance Analysis of and Compensation for Aspect-Ratio Effects of Fast-Fourier-Transform-Based Simulations of Large Atmospheric Wave Fronts." *Appl. Opt.*, **37**:4605–4613, July 1998.

[SJV04] J. A. Stoesz, L. Jolissaint, J. Veran, and J. LeDue. "An analytic model for natural guide star wide-field adaptive optics." In *Proceedings of the SPIE, Volume 5490, pp. 713-720 (2004).*, pp. 713–720, October 2004.

[SLC03] M. Schöck, D. Le Mignant, G. A. Chanan, and P. L. Wizinowich. "Atmospheric turbulence analysis with the Keck adaptive optics systems." In *Adaptive Optical System Technologies II. Edited by Wizinowich, Peter L.; Bonaccini, Domenico. Proceedings of the SPIE, Volume 4839, pp. 813-824 (2003).*, pp. 813–824, February 2003.

[SMG05] C. D. Sheehy, N. McCrady, and J. R. Graham. "Laser Guide Star Observations of Super Star Clusters in NGC 1569 and AO PSF Estimation in Crowded Fields." *American Astronomical Society Meeting Abstracts*, **207**, December 2005.

[Ste06] E. Steinbring. "Mauna Kea sky transparency from CFHT SkyProbe data." Private communication, 2006.

[Str70] J. W. Strohbehn. "Remote Sensing of Clear-Air Turbulence." *Journal of the Optical Society of America (1917-1983)*, pp. 948–+, July 1970.

[SVR04] J. A. Stoesz, J. Veran, F. J. Rigaut, G. Herriot, L. Jolissaint, D. Frenette, J. Dunn, and M. Smith. "Evaluation of the on-sky performance of Altair." In *Proceedings of the SPIE, Volume 5490, pp. 67-78 (2004).*, pp. 67–78, October 2004.

[SVR06] J. Stoesz, J.-P. Véran, S. Roberts, B. Ellerbroek, and M. Britton. "Evaluation of ground layer adaptive optics for the wide field optical spectrograph on the TMT." In *Proceedings of the SPIE, Volume 6272, pp. (2006).*, July 2006.

[TBV03] A. Tokovinin, S. Baumont, and J. Vasquez. "Statistics of turbulence profile at Cerro Tololo." *MNRAS*, **340**:52–58, March 2003.

[TLJ04] T. Travouillon, J. S. Lawrence, and L. Jolissaint. "Ground-layer adaptive optics performance in Antarctica." In D. Bonaccini Calia, B. L. Ellerbroek, and R. Ragazzoni, editors, *Advancements in Adaptive Optics. Edited by Domenico B. Calia, Brent L. Ellerbroek, and Roberto Ragazzoni. Proceedings of the SPIE, Volume 5490, pp. 934-942 (2004).*, pp. 934–942, October 2004.

[TLS00] A. Tokovinin, M. Le Louarn, and M. Sarazin. "Isoplanatism in a multi-conjugate adaptive optics system." *Optical Society of America Journal A*, **17**:1819–1827, October 2000.

[Tok04] A. Tokovinin. "Seeing Improvement with Ground-Layer Adaptive Optics." *PASP*, **116**:941–951, October 2004.

[TT06] A. Tokovinin and T. Travouillon. "Model of optical turbulence profile at Cerro Pachón." *MNRAS*, **365**:1235–1242, February 2006.

[TVZ05] A. Tokovinin, J. Vernin, A. Ziad, and M. Chun. "Optical Turbulence Profiles at Mauna Kea Measured by MASS and SCIDAR." *PASP*, **117**:395–400, April 2005.

[V01] J.-P. Véran. "Reconstructor Parameters Generator." aoRPG.doc / version 1.3, 2001.

[V04] C. Vérinaud. "On the nature of the measurements provided by a pyramid wave-front sensor." *Optics Communications*, **233**:27–38, March 2004.

[Ver00] J. Véran. "Control of the unilluminated deformable mirror actuators in an altitude-conjugated adaptive optics system." *Optical Society of America Journal*, **17**:1325–1332, July 2000.

[VRM97] J.-P. Véran, F. Rigaut, H. Maître, and D. Rouan. "Estimation of the adaptive optics long-exposure point-spread function using control loop data." *Optical Society of America Journal A*, **14**:3057–3069, November 1997.

[vSB06] M. A. van Dam, R. J. Sasiela, A. H. Bouchez, D. Le Mignant, R. D. Campbell, J. C. Y. Chin, S. K. Hartman, E. M. Johansson, R. E. Lafon, P. J. Stomski, Jr., D. M. Summers, and P. L. Wizinowich. "Angular anisoplanatism in laser guide star adaptive optics." In *Proceedings of the SPIE, Volume 6272 (2006).*, July 2006.

[VY06] C. R. Vogel and Q. Yang. "Multigrid algorithm for least-squares wavefront reconstruction." *Appl. Opt.*, **45**:705–715, February 2006.

[Win91] D. M. Winker. "Effect of a finite outer scale on the Zernike decomposition of atmospheric optical turbulence." *Optical Society of America Journal A*, **8**:1568–1573, October 1991.

This page is intentionally left blank.

“As the sun sank lower and touched the edge of the cloud-belt on the horizon, Hazel came out from under the branches and looked carefully round the lower slope. Then he stared upwards over the ant-hills, to the open down rising above. Fiver and Acorn followed him out and fell nibbling at a patch of sainfoin. It was new to them, but they did not need to be told that it was good and it raised their spirits.”

Richard Adams, *Watership down*